MODELLING AND ANALYSIS OF A NEW INTEGRATED RADIOFREQUENCY ABLATION AND DIVISION DEVICE

LEONG CHING YING, FLORENCE

NATIONAL UNIVERSITY OF SINGAPORE

2009

MODELLING AND ANALYSIS OF A NEW INTEGRATED RADIOFREQUENCY ABLATION AND DIVISION DEVICE

LEONG CHING YING, FLORENCE
(***B.Eng (Hons.), Multimedia University, Malaysia)***

A THESIS SUBMITTED

FOR THE DEGREE OF MASTER OF ENGINEERING

DEPARTMENT OF MECHANICAL ENGINEERING

NATIONAL UNIVERSITY OF SINGAPORE

2009

I. Acknowledgement

The writing of this thesis has been one of the most significant challenges I have faced throughout my candidature. It is my greatest pleasure to express my gratitude for the many people who made this thesis possible. To them, I owe my deepest gratitude.

First and foremost, I am deeply indebted to my supervisor Professor Poo Aun Neow. Without him, I would not have thought of pursuing the Master of Engineering in NUS. He is always there to lend me a hand in many aspects. The continuous support, encouragements and guidance he has shown throughout this endeavor are invaluable. He has given me the motivation to face challenges I encountered with great courage and perseverance.

This is a great opportunity to express my respect to my co-supervisor, Assistant Professor Chui Chee Kong as well, for he has provided encouragement, sound advice, good teaching, and great ideas throughout my research and thesis-writing period. With his enthusiasm, inspiration, and great efforts to explain things clearly, simply and patiently, he helped to make this research meaningful for me. I would have been really lost without him.

I have furthermore to express my utmost gratitude to Dr Stephen Chang from the Department of Surgery, NUH, for the opportunity to work on this research funded by his research grant. He has also contributed much inspiration and shared much wise advice, especially in the medical side of this research. Most importantly, I have learnt ample knowledge in the area of biology and gained invaluable experience as well as exposures working with Dr Chang.

I am pleased to thank the people whom I have worked closely with – Mr. Yang Tao, Mr. Yang Liangjing, Mr. Huang Wei Hsuen, Mr. Khoo Seng Chye, Ms. Yu Ruiqi and everyone in Control Lab. They have been always around to provide me with necessary assistance and support in many aspects of the research. It has been great and fun working with them.

I am also very grateful to those who have been by my side all this while. The friends I met when I first came – Dr. Xi Xuecheng, Ms. Yang Lin, Mr. Van Dau Huan and Ms. Bahareh Ghotbi, and others – Ms. Wang Qing, Mr. Kommisetti V R S Manyam, Ms. Low Siok Ling and Dr. Ong Lee Ling, always remain great friends, not forgetting my wonderful friends back in Malaysia, especially Mr. Mohd Taufik Hamzah, and Ms. Susan Lim. They helped me get through the difficult times, with all the support, camaraderie, entertainment and care.

Lastly, and most importantly, I would like to dedicate this thesis to my parents, Joachim Leong Soon Shiu and Lim Kiat Sing. Without their continual moral and emotional support, encouragements, understanding, sacrifices, care and love, I would not have reached this far.

II. Table of Contents

III. Summary

Liver cancer is one of the world's deadliest diseases. The intervention methods in hepatic surgery have always been complicated and time-consuming especially due to the vascularity of the liver. Two most common hepatic treatment techniques are radiofrequency (RF) ablation and hepatectomy. Each has its individual complications and risks.

Tumour reoccurrence is a major worry of liver ablation while liver resection has always been complex due to the concern of blood loss. The implementation of RF ablation in assisting resection could be a promising intervention method. However, the two processes are often performed separately, with ablation performed first on the desired liver zone and manual resection with surgical scalpel by surgeons thereafter. Tissue cuts that exceed the necrosis zone is likely to happen, leading to blood loss. Re-ablation of the area is then required immediately to avoid losing more blood, resulting in time loss.

The objective of this research is to integrate both the RF ablation and resection processes into a single procedure, minimizing the above inconveniences and risks. With a new medical device prototype design, the integration concept is made possible. However, to further develop and enhance the device, more in-depth studies and experimental analyses are required in understanding the liver tissue and its interaction with the devices in contact. This led to the study of the liver tissue mechanical properties as well as the dynamic model of the tissue/cutting tool interaction.

The liver tissue, like other soft biological tissues, is viscoelastic in nature, exhibiting both elastic and viscous attributes, which generally produces a non-linear response. However, since this research focuses on the response of localized liver tissues at minimal deformation prior to cutting, the response can be assumed to be linear.

Therefore, the liver tissue is modelled using the Kelvin model, also known as the standard viscoelastic model and verified using biomechanics experiment on fresh porcine liver. The work is then extended to the examination and modelling of coagulated porcine livers based on measured biomechanics properties. The Maxwell-Kelvin combination is found to reflect the mechanical properties of the coagulated tissue closely. These mechanical models are ascertained by the curve fitting process onto respective relaxation response generated by the compression experiments. The models for the non-coagulated and coagulated liver tissues are proposed accordingly.

The modelling of liver tissue and scalpel interaction along with the applied force and deformation is also derived. The mechanical models and properties acquired from the tissue modelling process are implemented to determine the interaction models between the tissues and scalpel. Penetration experiments were performed onto the tissues to investigate the cutting force and time. These findings are essential in studying the relationship between the liver tissues and the cutting tool.

The mechanical models of the liver tissue and its interaction with the cutting tool can be applied to surgical simulation and planning. Thus, the introduction of the new integrated RF ablation and division device into the real clinical world could be realised.

IV. List of Figures

V. List of Tables

Chapter 1: Introduction

1.1. Background

The liver is one of the most vital organs in the human body, performing essential functions such as blood purification, toxic degeneration, food storage and distribution as well as digestion. Diseases infecting and malfunctioning liver result in much pain and inconvenience. Even though vaccines are available to control liver diseases in at-risk patients, the only potentially curative therapy for cancerous growths in the liver is the excision of tumours. Since decades ago, many surgical methods and technologies have been studied to determine the best treatment for liver cancer. However, important consideration such as the risk of intraoperative bleeding during liver surgery added complexity into these researches. This is because liver is a very vascular organ, containing as much as 10% of all body blood at any one time. It is an organ with a unique microanatomy in relation to hepatic arterial, portal venous and hepatic blood with interconnecting lobular sinusoidal anatomy [1]. There are cases in which patients do not have sufficient hepatic reserve for certain treatments, i.e. resection whereby the cancer infected portion of the liver is removed, as well as complicated locations of tumours within the liver, i.e. considerably near major blood vessels, pose issues that are yet to be solved by clinicians.

Liver cancers along with cancers of the lung, stomach, and rectum/colon cause the highest death toll factors worldwide. Liver cancer is known as the third most common cancer disease in the world as estimated by the International Agency for Research on Cancer, causing 598,000 deaths as of year 2002 [2]. The World Health Organization reported that, in year 2002, there were approximately 618,000 deaths for

every million new cases of patients with liver cancer [3]. Five-year survival rates of only 3% to 5% rates were achieved from the incidences in United States and Japan, and in developing countries such as China [2], despite the advances in medical technologies and treatment. According to a report by Xinhua News Agency on the 28th July 2008, almost half of the world's new liver cancer patients are from China, accounting for about 350,000 annually, resulting in 320,000 deaths that year [4]. The National Cancer Centre Singapore (NCCS) cancer statistics showed that in the same year, liver cancer is ranked fourth as the most common cancer among Singaporean men as well as the second deadliest cancer in Singapore [5]. As of year 2009, liver cancer remains a major killer, across the world causing the fourth highest number of deaths with an estimated at 610,000 [6]. Along with the possible increase in the world population as predicted in the document reported by the United Nations [7], the percentage of liver cancer incidences may have declined; nevertheless, it is still a serious disease for which treatment methods and cures are urgently needed and rigorously researched on.

Hepatic resection has conventionally been the only curative option for patients with liver tumours. It was an alternative to liver transplantation though a study showed promising results on the latter treatment. There are however, tradeoffs in either method. Hepatic resection is risky if performed on those with limited hepatic reserve whilst transplantation may results in rejection of the transplanted liver. Both treatment methods are prone to severe blood loss. With the advances in medical technologies, the ablation technique is now a significant method of treatment to liver intervention [8]. There are several new thermal ablative therapies introduced for liver treatment, such as microwave ablation (MW), radiofrequency (RF) ablation, focused ultrasound ablation, hot saline injection, and laser coagulation therapy. Generally, these therapies can treat

patients that are not able to undergo hepatic surgery. However, the suitability of treatment will be dependent on their conditions and severity. All thermal ablation techniques apply heat energy through a medium to destroy targeted tissue but the process, abilities and affects differ from one another. The closest related ablation therapies are the MW and RF ablation methods.

MW hepatic ablation is a tumour coagulation method which delivers microwave power through a microwave applicator, i.e. an antenna, generating electromagnetic wave to heat and destroy the tumours. MW has the capability over RF ablation in heating tissue to a temperature as high as 125 degrees Celsius [9], and is viewed as a guarantee for cell death. Higher levels of heat generation enables faster and more effective ablation of tumours near blood vessels as it is least affected by the heat sink effect induced by blood flowing through vessels that disperses the MW generated heat. However, high temperature ablation may cause excessive burning and larger necrosis, which may cause undesirable char to normal tissue around the localized region.

RF ablation is another new invasive procedure, almost similar to the MW ablation, differing by only its maturity level in clinical environment, affects and implementation. It involves the use of high-frequency alternating currents in the radiofrequency range of approximately 500 kHz flowing through the needles attached to the probes. This produces frictional heat and ionic agitation in the liver tissues. Coagulation necrosis is then created within the localized region of the ionic agitation flow. RF ablation is now the world's most widely used modality in the treatment of liver cancer [10]. Though this method does not generate as much heat as MW ablation

to destroy tissue, the RF ablation technique creates necrosis within reasonable range of temperatures sufficient for general cell death.

Further application of this technology in liver resection helps to reduce bleeding. The process of combining RF ablation and liver resection in treatment of liver cancer has been introduced, increasing the success rate of liver surgery [11, 12]. Resection is performed after the parenchyma is coagulated by monopolar or bipolar radiofrequency ablation [12]. The process involves ablating a desired line of resection in the liver prior to manually cutting the unwanted portion away using a surgical scalpel by surgeons. As ablation of normal liver tissue is considerably faster than that of abnormal tissue, this technique is less time consuming than ablating the cancerous tissues alone. Ablation of tumours ranging from 2 to 3 centimetres and greater requires at least 6 and 12 overlapping ablations respectively for complete cell destruction [13]. This combined method also results in minimal blood loss during hepatic transaction, and is one of the most significant advantages of alternating the RF ablation-resection process [14].

Upon coagulation of the tissue, radiofrequency ablation denaturalizes the tumour using heat created by ionic agitation, thus leading to cell death at sufficient heating. Beyond a temperature of approximately 40 degrees Celsius, thermal damage to the liver tissue will start to occur [15]. A fully ablated tissue is significantly harder than a normal tissue due to water loss from the tissue and denaturalization [1, 16]. Water evaporation occurs significantly as the tissue temperature reaches 70 degrees Celsius [17]. Besides desiccation, ablation results in obvious tissue shrinkage of the liver, as well as of its vascular and binary branches due to collagen bonding. Throughout the vaporization process, the material properties of the ablated liver tissue vary. From the stress-strain curve obtained, the stress at 20% strain is about 1,000 Pa

and 2,000 Pa for liver tissues ablated at 37 degrees Celsius and at 60 degrees Celsius respectively. At an ablation temperature of 80 degree C, the stress is about 20,000 Pa. This stiffness and the sensed compressive force information upon division of the ablated tissue can determine the appropriateness of the coagulated regions to be divided.

The study of soft tissue deformability due to stress and strain factors is related to tissue biomechanics. Mechanical properties of soft tissues, i.e. brain, liver, and kidney, has been popular in biomechanics research as these tissues do not bear mechanical load which is different from typical engineering materials. Even though many non-linear mathematical models have been developed to represent soft tissues, including liver which is the focus of this research, it is unclear which models are appropriate for real-time elastic deformation simulation. Simplified models are often used for surgical simulation purposes. Computer Aided Surgery implementing the finite element method has been increasingly popular among researchers in simulating the deformation of human organs for surgical simulation. Several methods to model tissue mechanically have been reported. Non-physical constructions model, e.g. the linked volume representation is introduced [18, 19] as well as physical construction based modelling which was pioneered by Terzopoulos [19]. One of the most widely used physical methods is the spring–mass model composed to closely model the mechanics of soft tissue. In some conditions, soft tissues are modelled as elastic materials. However, most current research involves viscoelastic models as soft tissues exhibit viscous nature as well. The popular mechanical models used to describe soft tissues are the Maxwell model, Kelvin model (Standard Linear model), and Voigt model [20] which have been commonly used and integrated to model different parts of body tissues.

1.2. Motivation and Objective

The agony of the patients with liver diseases and the complications of hepatic treatments greatly motivated this study. Bleeding during hepatic surgeries is a major concern due to the vascular nature of the liver. There are methods to aid the stopping of blood flow during resection, for example, the Pringle manoeuvre [21]. However, these procedures are often complicated and time consuming. Ablation of liver tumours, which is commonly applied, leads to localized cell death, but may not be the most optimal solution for there are possibilities of cancerous cells reoccurrence.

An innovative design of a bio-mechatronics device integrating RF ablation with the resection process is one of the objectives to be achieved towards clinical advancement. The new integrated device executes the process of ablation and liver division alternately within specific coagulated zones. In conventional and manual liver dissection, the risk of over-cutting outside the necrosis zone may occur, causing blood loss. The integration benefits in eliminating the risk of bleeding due to over-cutting as well as time loss due to re-ablation of coagulated areas. With a fully ablated necrosis by the RF needles, a complete stoppage of blood flow is achieved leading to an almost bloodless resection, and thus significantly reduces the need for blood transfusion.

A theoretical study and analysis is essential to show the feasibility and significance of this research. The liver tissues, both non-coagulated and coagulated, are modelled mechanically approximating actual tissue, following an analysis that shows the interaction of the tissues corresponding to the contact of the probe, i.e. surgical scalpel. Experimental responses obtained are used to simulate real clinical observation with respect to cutting force and speed. The interaction relationship can be implemented for surgical planning and simulation purposes.

1.3. Research Scope

This study involves the development of a new concept, which is an integration of RF ablation and the division device for successful and convenient hepatic surgery. A prototype design is constructed according to the clinical specifications. It is a preliminary design concept for the purposes of experimental observations, improvements and advancements prior to real clinical applications. The observations and findings from the design and experiments led to comprehensive studies on the modelling of liver tissue and its interaction with devices in contact. The models are obtained and analyzed through experiments and dynamic modelling. The propositions and findings are beneficial not only in providing improvements to the current prototype device design, but also for future studies related to the scope of interest. As the RF ablation process is at a mature stage and is known for consistent coagulation, the significant part of this study focuses on effective cutting of the liver tissue - fast cutting for minimal tissue deformation and with minimal force.

1.4. Organization of the Thesis

Chapter One introduces the background of the topic of research as well as the motivation behind the project and objectives to be achieved. A collection of research works accomplished in the related area of research is reviewed in Chapter Two, providing an insight in liver intervention concepts, issues, developments and advancements. The construction and observations of the integrated RF ablation and division device is discussed in Chapter Three, along with the recommendations for improvements. These are supported by the studies presented in the following chapters, Chapter Four and Chapter Five. To understand the mechanical properties of the liver tissue for the cutting process, its material attributes have been examined in both the coagulated and non-coagulated tissue conditions. Experimental analyses and dynamic models of both conditions are constructed in Chapter Four. A study of the interaction between the liver tissue and cutting device is then provided in Chapter Five. Finally, discussion on the overall study, contributions of this work and recommendations are concluded in Chapter Six.

Chapter 2: Literature Review

2.1. Liver Ablation and Resection

Treatments of liver cancer had been a major research issue decades ago. With advances made in the integrated fields of medicine, engineering and computer science, many improved interventions have been made possible although risks and various side effects are still present. The treatment techniques chosen for patients are dependent on such factors as the characteristics and locality of the diseases or tumours. Many studies have been performed to improve the treatment, survival rates and surgical processes. Some relevant studies are discussed in this chapter.

2.1.1. Liver Resection and Transplantation

Hepatic resection has been one of the major curative treatments to liver cancer before the maturity of other possible treatment methods, with the mortality rate reported to be up to 20% to a routine surgery carried out in high volume liver units with an operative risk less than 5% [22]. In this treatment, cancerous and disease-infected portions of liver are eviscerated to prevent the spread of cancerous cells to other regions of the liver or body. Depending on the severity of the infection, the amount of liver to be removed is determined, with the requirement that a minimum of 40% of the liver volume must remain as a safe reserve [22].

The surgical process is time and effort consuming as resection is often performed manually with surgical scalpels by surgeons. Blood loss or haemorrhage during the operation is a significant issue due to vascularity of the liver, although haemostasis is performed through several methods during the intervention. In the

event of excessive blood loss, blood transfusion is needed and high risks exist. To prevent these, one of the popular haemostasis procedures is the clamping of the hepatic vessels (Pringle manoeuvre or inflow occlusion) to avoid excessive blood loss [21]. As the Pringle manoeuvre does not control the backflow bleeding of the veins, Zhou et al. [23] suggested the selective hepatic vascular exclusion (SHVE) that is also an improvement to total hepatic vascular exclusion (THVE). In vascular occlusion, several methods are applicable; e.g. suture ligation, tying veins with tourniquets and Satinsky clamping. From the experiment and comparison of these procedures performed by Zhou et al. [23], the Pringle manoeuvre results in higher mortality rates, longer hospitalisation, and higher occurances of post-operative bleeding and liver failure in patients. Cromheecke et al. [24] controlled blood flow during resection with the use of compression sutures. Throughout their experiments, this method resulted in no deaths. Hilal et al. [22] applied fibrin glue onto cut surfaces to occlude blood flow during hepatic resection. In cases where hepatic artery resection is required, arterialisation of the portal vein after hepatic artery resection is performed [25].

Apart from the manual methods, there are other means of hepatic resection involving external devices or tools. In the Finger Fracture method, the liver parenchyma is fractured between the finger and thumb of the surgeon especially when surgical tools are not available [26]. The Cavitron Ultrasonic Surgical Aspirator (CUSA) has also been widely applied for hepatic resection whereby ultrasonic energy is transmitted into the liver parenchyma to break, de-bulk and emulsify the tumours which are then sucked away from the organ. However, a subsequent study revealed that CUSA increases the incidence and severity of venous air embolism within the organ [27]. Y. Hata et al. [28] designed a water-jet device that cuts liver tissues with the flow of pressurised fine water concentration. This resection technique is shown to

be more reliable and effective as compared to CUSA. The average operation time was about 5 hours (CUSA, 6 hours) with a morbidity rate of 12.5% (CUSA, 40%) [28].

If the cancerous cells are beyond control and has spread throughout wide regions of the organ, especially in patients with limited hepatic reserve, hepatic transplantation is then the preferred treatment option. This intervention option depends also on the characteristics of cases, i.e. size of tumours, involvement of major vessels and number of nodules. It is unsuitable in treating large tumours (>3cm) with three or more nodules and should be restricted to that less than 3cm with one or two nodules [29]. The survival rate however, is not very promising, with 3-year survival rate of 31% as compared to the 3-year survival rate of 50% after resection [29]. Organ rejection by the immunity system and haemostasis remain serious concerns.

2.1.2. Liver Thermal Ablation

Though hepatic resection has been the preferred treatment for liver cancer, there are complicating factors affecting resection that lead surgeons to implementing other interventions, e.g. the issue of haemorrhage and unsuitable locations of tumours. Liver ablation treatment for liver cancer has been used and improved upon significantly during the past decades with advances made in thermal technologies, treatment techniques, and surgical devices. The thermal ablation treatment for liver tumours has been an alternative to conventional treatments, such as chemotherapy, and chemoembolization. Ablation techniques are also receiving increasing attention for treatment of other malignancies like lung, and kidney cancer.

There are a variety of thermal ablation techniques available for treating liver cancer. These are generally grouped into three major categories - chemical based

(ethanol or alcohol injection), extreme cold-based (cryoablation), and extreme heat-based (radiofrequency ablation, microwave ablation and laser ablation) ablations. These treatments can be performed in laparoscopic, percutaneous, and open surgery.

Among the various methods of thermal ablation, radio-frequency (RF) ablation is the most widely applied technique worldwide for the treatment of liver cancer for unresectable liver tumours [30, 31]. Sutherland et al. [32] stated that RF ablation may be more effective compared to other treatment methods. Some studies showed that RF ablation results in lower reoccurrence rate as compared to percutaneous ethanol injection (PEI) [33, 34]. PEI is a chemical ablation technique that diffuses ethanol into lesions to coagulate the localised tissue. Percutaneous hot saline injection therapy (PSIT) is assumed to be a better alternative to PEI as toxicity will not be a concern [35] with the amount of injection required for the treatment.

Cryoablation is slightly similar to the above two methods, except that instead of injecting ethanol into the tissue, the cryoablation method injects liquid nitrogen through a device probe. According to Onik et al. [36], Charnley et al. [37] and Zhou et al. [38], cryoablation is a promising, safe and simple treatment and can be a good choice for the treatment of liver cancer. However, some complications do cause concern. Besides the common issues like haemorrhage and hepatic failure, Sarantou et al. [39] pointed out that cryoablation could cause dangerous effects such as hypothermia, parenchyma fracture, billiary fistul, pleural effusions and acute renal failure.

There exist other electro-generated ablation methods. Apart from RF ablation, microwave (MW) and laser ablation techniques are also used for the treatment of liver cancer. Laser ablation utilises a Nd:YAG laser with the intense laser beams delivered

to the lesion through multiple bare-tip 300-nm fibers inserted spinal needles [40]. Laser ablation now competes in popularity with RF ablation as both are almost equally efficient, and with fewer major complications. In MW ablation, a microwave generator emits an electromagnetic wave through an antenna, agitating water molecules in the surrounding tissue to create coagulation necrosis. MW ablation is found to be superior to other ablation techniques in producing higher ablation temperatures, larger ablation region, and faster ablation [41, 42]. This method is the best option to treat tumours located near vessels as the heat sink effect can be reduced [42], thus decreasing the possibility of reoccurrence. However, thermal damage to surrounding tissues is greater in this treatment technique due to its nature.

2.1.3. Radiofrequency (RF) Ablation

In RF ablation, the lesions are coagulated via alternating currents flowing through the probes of the RF ablation device at radio frequencies of approximately 400 kHz, thereby causing ionic agitation resulting in necrosis of the tissues. To date, many devices have been developed for RF ablation. The two major types are the bipolar and the monopolar RF ablation devices. Diversive grounding pads are required for monopolar RF devices and these are normally placed on the thighs or back of the patients. Rita Medicals, Radiotherapeutics and Boston Scientific developed an RF device with a multi-tined electrode to achieve higher levels of coagulation necrosis, while Radionics incorporated an active cooling system into its RF probes by perfusing chilled water through the needles into the liver tissue [8]. The objective is to allow the creation of a larger coagulation zone by controlling the ablation with the chilled water to prevent the charring of localised portions of liver tissue. Several RF ablation devices that are clinically used are shown in Figure 2.1.

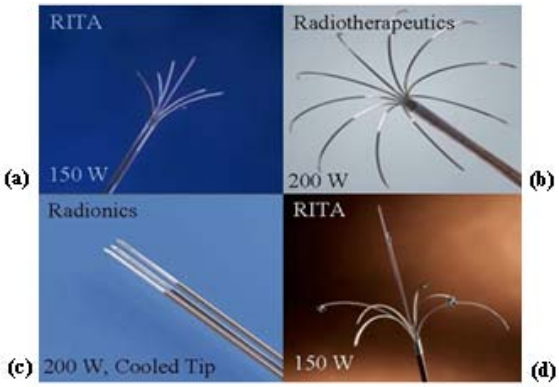

Figure 2.1: Samples of RF ablation devices, (a) & (d) Multitined electrodes by Rita Medicals, (b) Multitined electrodes by Radiotherapeutics, and (c) Cooled tip electrodes by Radionics. [43]

Yao [44] and his team developed a bipolar inline RF ablation device (as shown in Figure 2.2) and applied this successfully in rabbit experiments. This device creates a neat line of necrosis zone and is suitable for use with the resection process. However, it cannot be applied for laparoscopic and percutaneous surgery. Another development, the Habib 4x Laparoscopy RF ablation device which is licensed to Rita Medicals, is now being used for liver transections.

Figure 2.2: Samples of RF ablation devices, (a) Bipolar InLine RF Ablation Device [44], (b) Habib 4x RF Ablation Devices (for laparoscopic and open surgery). [45]

2.1.4. Radiofrequency (RF) Ablation Assisted Liver Resection

RF ablation, although not as powerful in terms of generating coagulation necrosis as MW ablation, is still one of the best options for liver tumour intervention and is the most widely used. This thesis focuses on RF ablation with resection for it can optimally induce thermal damage in the liver tissue and cell death at temperatures above approximately 40 and 60 degrees Celsius respectively [46]. This is sufficient to

prevent haemorrhage during the resection process. By incorporating RF ablation into RF-assisted liver resection, the coagulation of normal liver parenchyma is much more rapid than coagulation of tumour tissue [14, 47].

RF ablation has been used widely to assist in hepatic resection. Though some are still implemented in open surgery, the incorporation of RF ablation for resection enables laparoscopic surgery to be executed. According to the experiments performed using the Habib 4x RF ablation device [45, 48, 49], mortality and morbidity rates are reduced significantly compared to other ablation methods. Blood loss and the need for blood transfusion are minimal. Delis et al. [14] applied the Radionics Cool-Tip RF ablation device prior to manually cutting the coagulated portion of the liver parenchyma with a surgical scalpel in open surgery, as shown in Figure 2.3. Bachellier et al. [47] and Hompes et al. [50] performed similar procedures but in laparoscopic surgery. Clancy and Swanson [51] have used the InLine RF coagulation (ILRFC) by Resect Medical in assisting their resection process that is later performed separately with blunt dissection and cautery as well as with a harmonic scalpel. These transections resulted in minimal blood loss, and low mortality and morbidity rates.

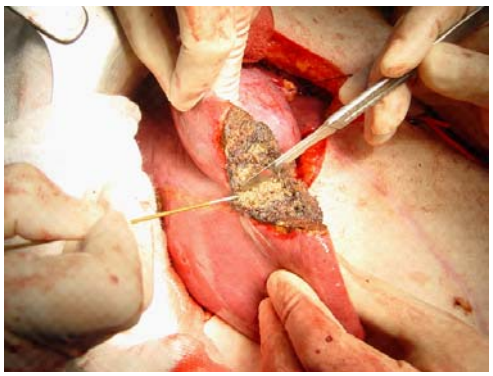

Figure 2.3: Cool-Tip RF assisted resection in open surgery. [14].

A new development of an RF assisted device for resection shown in Figure 2.4, revealed by Navarro et al. [52], combines a non-insulated cool-tip RF rod attached with a sharp cutting knife of 2 mm width for a bloodless and fast resection process.

This device first coagulates the surface of the liver tissue and then dissects the coagulated surface as the device is moved backwards. The method provides simultaneous interventions of coagulating and sectioning process, enabling a faster and more convenient procedure. However, due to the limitation in sizes of coagulation necrosis and the cutting blade, it can only cut 2 mm deep into the coagulated regions.

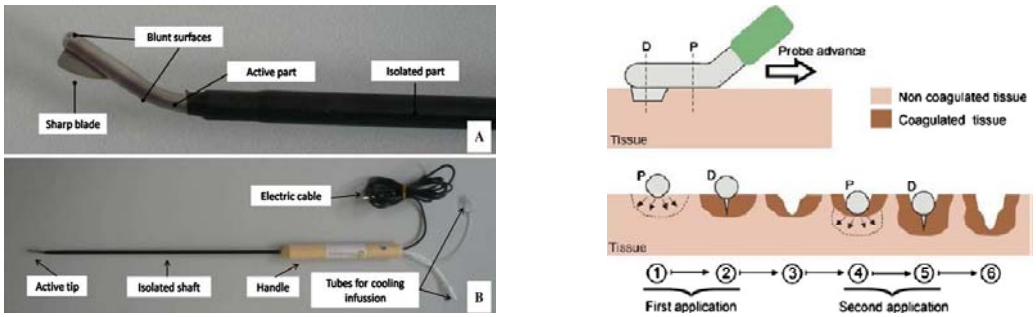

Figure 2.4: (left) The integrated RF device manufactured by Minimeca-Medelec, and (right) Lateral view of probe and the application process. [52]

There were some debates as to whether the RF assisted liver resection procedure causes severe damage to the liver. Mitsuo et al. [53] used a Radionics cool-tip system in assisting resection and showed that there was a significant reduction in intraoperative blood loss. However, there was also a higher risk of liver damage as the excessive induced necrosis is hazardous to patients who have limited hepatic reserve. There is also a risk of biliary leak at the main bile duct due to the conduction of RF energy. Thus, it seems that RF ablation in assisting resection, if not properly applied, may cause severe damage in liver cells [53], which is also supported by Berber and Siperstien [54]. Miroslav and Bulajic [55] commented that the technique used by Mitsuo et al. [53] is not suitable for resection as RF "CoolTip"^{TM} performs maximal pre-coagulation, which consumed more time and applied higher amounts of RF energy than required. This results in larger areas of necrosis overlapping remnant liver tissue. It is concluded that a proper choice of the RF application must be made in assisting resection in order to achieve a safe and efficient procedure.

2.2. Modelling of Tissue

2.2.1. Finite Element (FE) Modelling

Basafa et al. [56] , in his study on realistic and efficient simulation of liver surgery, used the FE method to simulate the deformation of liver tissue. It is an extension of the mass-spring modelling approach for a more realistic force formation behaviour while maintaining the capability of real-time response. According to Basafa et al [56], linear springs used in most previous simulations fail to show the nonlinear response. In the interactive simulation, the liver model is touched by a virtual instrument as illustrated in Figure 2.5. Basafa et al. also a verified that the model allows the parameters to be tuned based on experimental data unavailable in previous approaches and this advantage can lead to the development of an effective VR laparoscopic surgery trainer.

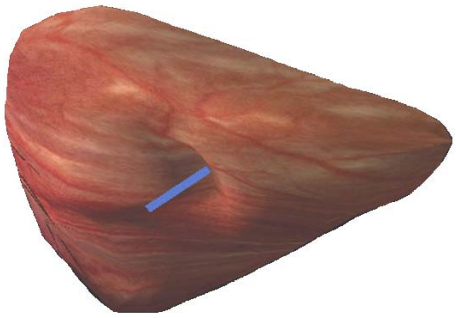

Figure 2.5: Interactive simulation of a liver model under deformation [56]

Another approach using the FE method is known as the hierarchical multi-resolution finite element model, proposed by Nesme et al. [57] to obtain computational efficiency on continuous biomechanical models that adapt numerical solution schemes, i.e. matrix inversion and nonlinear computation of the strains, to the adequate level of details. The proposed model merges a multi-resolution description with a Hierarchical FE integration which is proven to generate a more realistic result.

The process defines a 3D octree mesh based on the mutation concept of a cubic bounding the body of the object. A maximal level of division is defined when a "maximal density" octree mesh is reached. Illustration of the process is shown in Figure 2.6 and Figure 2.7, which show the 3D octree meshes for a liver.

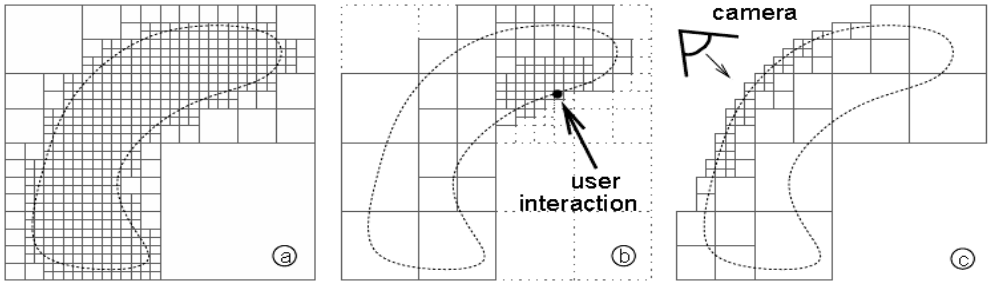

Figure 2.6: (a) leaves of the octree mesh = finest level of details, (b) mechanical leaves = finest mechanical level, and (c) geometric leaves = finest geometric level. [57]

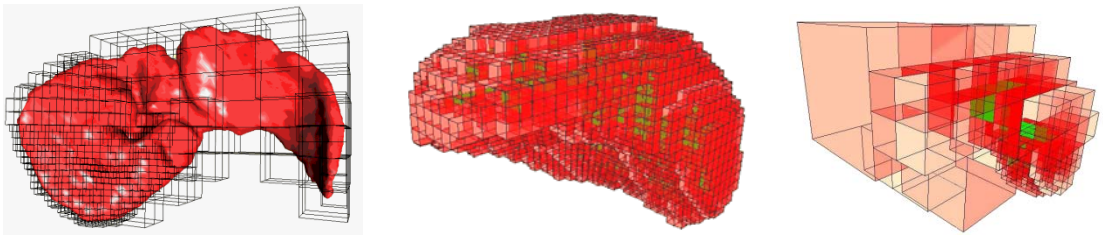

Figure 2.7: An octree-mesh for a liver: densities of mechanical leave for the finest level of details and for a multiresolution mesh. [57]

In comparison to traditional finite element approaches, this method simplifies the task of volume meshing in order to facilitate the use of patient specific models, and increases the propagation of the deformations [57].

Cotin et al. [58] proposed a combination of three liver models based on linear elasticity; a quasi-static pre-computed real-time elastic model, a topology changing tensor-mass model and a hybrid of both these models. The hybrid model of the liver combines the advantages of both the earlier models, allowing efficient cutting and deformation in real time. The liver is modelled as tensor-mass for the portion that directly interacts with the surgical tools, and as quasi-static elastic elements beyond the boundary. The tensor-mass and hybrid elastic models are shown in Figure 2.8.

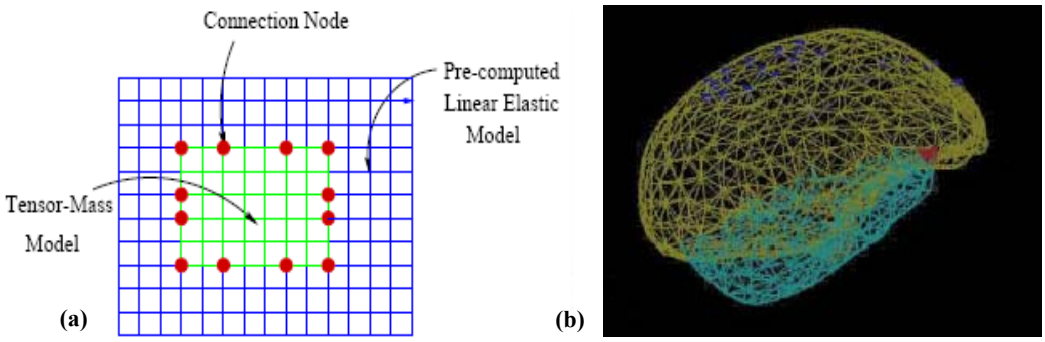

Figure 2.8: (a) Visualization of nodes connecting tensor-mass model and pre-computed liner elastic model, (b) wireframe FEM version of the hybrid elastic model with upper mesh as quasi-static pre-computed model and lower mesh as tensor-mass model [58]

2.2.2. Segmentation and Statistical Shape Modelling

Some research has done on modelling livers with statistical shape modelling. Statistical modelling allows segmentation of the liver, essential for hepatic surgery pre-operative planning. It allows computation of the resection volume. Building a 3D shape model from a training set of segmented instances of an object; i.e. from Magnetic Resonance (MR), Ultrasound (US) and CT (Computer Tomography) images, is the determination of the correspondence between different surfaces, and this process is one of the major challenges.

Lamecker et al. [59, 60] have used this modelling method to model the compactness and completeness of livers. Statistical modelling is performed by the Lamecker et al. based on several procedures [59] as illustrated in Figure 2.9. Firstly, extraction and representation of liver shapes acquired from CT imaging is performed.

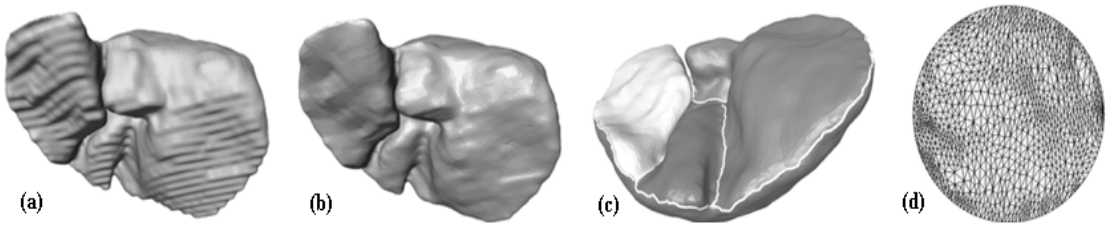

Figure 2.9: Triangulated surface of the liver: (a) before and (b) after interpolation, Surface decomposition into (c) liver decomposed into four patches along lines of high curvature, and (d) one parameterized patch. [59]

The second step involves decomposing the surface into patches and mapping a patch on one surface onto the corresponding patch on another surface to minimize local distortion, such as local scaling and shearing.

Following that registration of surfaces and principle component analysis is performed to gain statistical information by aligning the 3D images acquired. The authors compared the compactness and completeness of the livers by two alignment strategies, i.e. the mere translation (TRA) and the mean least squares (MLS) methods. It is found that the TRA model is more compact than the MLS model, while the absolute variance is larger for the TRA model.

Another related research is done by Massoptier and Sergio on segmenting three dimensional liver surfaces automatically from images obtained via CT or MR by using the graph-cut technique [61] and the Gradient Vector Flow (GVF) snake [62]. The results of the two techniques are compared for best contribution in Figure 2.10.

Active contour in GVF is used to obtain an accurate surface that approximates the real liver closely. Its application in the segmentation of CT images resulted in good time processing and quality. However, this technique is prone to assume a mistaken boundary for related particles located inside but close to the liver surface, considering them to be outside the region of interest [61]. This error is undesired and it is addressed by the graph cut technique for more accurate automatic image segmentation. This method works with the mean and standard deviation of liver samples in determining the error margin and hence, the accurate boundary of the liver region based on the voxels, edges and vertices of the liver from the CT images. The three dimensional segmentations are evaluated and it is found that the error in implementing the graph-cut technique is lower than that applying the GVF technique.

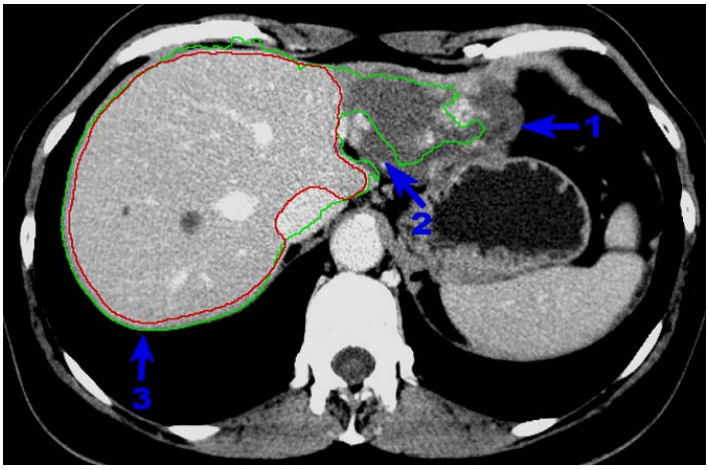

Figure 2.10: Visual comparison between the graph-cut method (green line) and the active contour segmentation (red line). The graph cut method extends the boundary of the active contour method towards the real contour. However, the lesion pointed by arrow 1 was neglected. [61]

Delingette and Ayache [63] performed 1mm interval slices to obtain anatomical CT images to extract an accurate shape of the liver. Each image contrast is enhanced for clear edge detection of smooth liver boundary. Two dimensional slice extractions are transformed into tridimensional binary images by using the model-based reconstruction algorithm involving deformable contours and surface meshes [64]. Using a marching-cube algorithm [65], the images are then processed to form the external surface of the liver using subvoxel triangulation as seen in Figure 2.11.

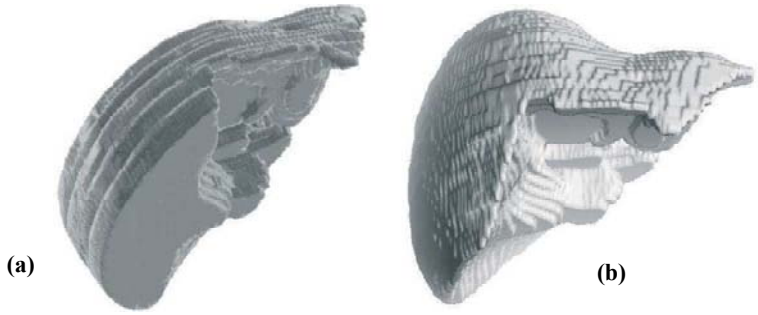

Figure 2.11: (a) 3D model of liver resulted from stacking of segmentations, (b) surface construction based on marching-cube algorithm. [63]

As the triangles generated by the subvoxel triangulation is high in computational and processing cost, the simplex meshes method developed by Delingette et al. is implemented for segmentation and simplification as well as smooth triangulated surfaces based on vertices connectivity, as depicted in Figure 2.12.

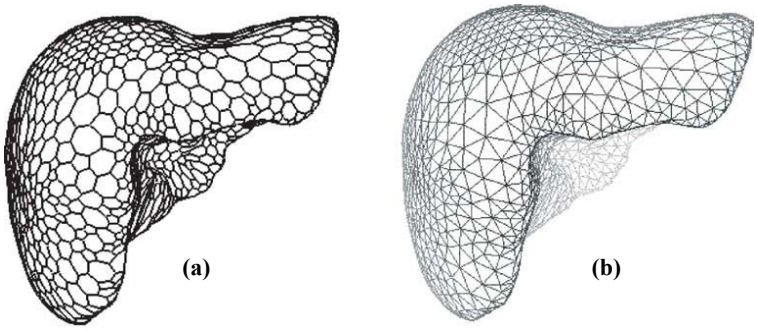

Figure 2.12: Simplified 3D liver model; (a) Simplex mesh model, (b) triangulated dual surface. [63]

2.2.3. Mechanical Modelling

Many researchers discuss tissue modelling in the framework of the linear viscoelasticity relating stress and strain on the basis of Maxwell, Voigt, and Kelvin models. Buchthal and Kaiser [66] first formulated the continuous relaxation spectrum corresponding to a combination of an infinite number of Voigt and Maxwell elements in modelling of the muscle fibre. In the studies relating tendons and joint ligaments, Viidik [67] proposed a nonlinear application of the Kelvin model based on a sequence of springs of different natural length, with the number of participating springs increased with increasing strain. Terzopoulos and Fleiseher [68] suggested a four-unit viscoelastic model, a series assembly of the Maxwell and Voigt viscoelastic models (as shown in Figure 2.13) so that internal forces depend not just on the magnitude of deformation, but also on the rate of deformation. It is a study which aids in the modelling of soft tissue, which is also viscoelastic in nature.

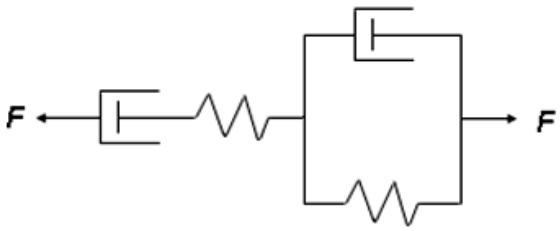

Figure 2.13: The four-element model of a Maxwell unit in series with a Voigt unit respectively, In which *F* denotes the external force. [68]

Schwartz et al. [69] introduced an extension of the linear elastic tensor–mass method for fast computation of non-linear viscoelastic mechanical forces and deformations for the simulation of biological soft tissues with the aim of developing a simulation tool for the planning of cryogenic surgical treatment of liver cancer. The Voigt model was initially considered to approximate the properties of liver tissues. However it was later discovered, from experiments, that a linear model is not suitable for modelling this application under various needle penetration loads [69].

Ko et al. [70] investigated the relaxation of residual stresses due to viscoelastic deformation in a film/substrate system using the Kelvin model. Experiments were performed and results were compared with those obtained from the Maxwell model. The experiment performed showed that for a given time, the stress relaxation rate using the Kelvin model is faster for a smaller thickness ratio of the film, and this trend is the same as that obtained from the Maxwell model. However, for the same parameters the Maxwell model requires a longer time to reach the steady state than the Kelvin model. As for full relaxation, the Maxwell model can have full stress relaxation but the Kelvin model cannot. The relaxation rate is greater for the Kelvin model than for the Maxwell model while the stress relaxation time is shorter for the Kelvin model than for the Maxwell model. This shows the opposite trend for an elastic film deposited on a viscoelastic substrate and it is based on suitability of the implementation that appropriate results can be acquired.

In studying the mechanical model of the human vocal fold, Flanagan and Landgraf [71] represented each vocal fold as a mass-spring-damper system. The system is excited by a force F, given by the product of the air pressure in the glottis with the area of the intraglottal surface. The force acts on the medial surface of the vocal folds.

Although the one-mass model produces acceptable voiced-sound synthesis and simulates the glottal flow properties, it is inadequate to produce other physiological details related to the vocal folds behaviour. Thus, multiple-mass representations of the folds is proposed by Ishizaka and Flanagan [72]. In the two-mass model, vocal folds are represented by two coupled mass-damper-spring oscillators.

In another study, Hauth et al. [73] states that the Voigt, Maxwell and Hooke models have a simple exponential relaxation and creep law, which is usually not sufficient to reproduce the relaxation and creep behaviour accurately. The Prony (or Constant Q) model [73] which seems to be almost similar to the Kelvin model, except that it has a series of Maxwell elements, is suggested. The schematic of the model is shown in Figure. 2.14.

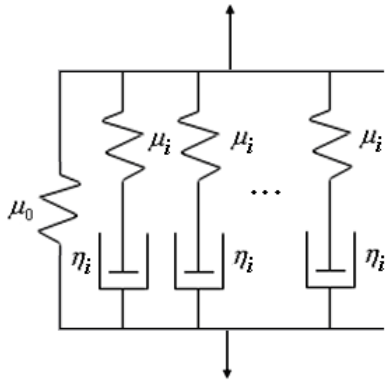

Figure 2.14: Prony model (μ_i and μ_0 are spring constants while η_i is damper coefficient). [73]

The relaxation function is then expressed in exponential term with a unit-step function, *I(t)* as shown in Equation (2.1) [73], where μ_0, μ and η are ... and *t* is time.

$$k(t) = \left(\mu_0 + \mu e^{-\frac{t}{\eta}}\right) I(t). \tag{2.1}$$

Hauth et al. then compares the results between experiments applying Hooke and Prony concepts based on a frequency test via a finite element discretization as depicted in Figure 2.15. It is found that longer oscillations occurred in the case based

on Hooke's model. The model utilizing Prony material model, known as the constant Q material model, is more capable of modelling organic materials accurately [73].

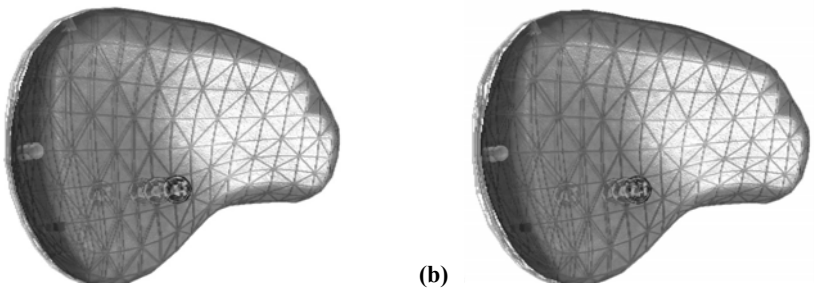

Figure 2.15: Liver with 327/2616 Tetrahedra, snapshots of creep (a) with a constant Q material, and (b) with Hooke material. [73]

Sinkus [74], on the other hand, described a more advanced spring-damper model as pictured in Figure 2.16, which resembles a fractal arrangement with an infinite series of Maxwell units as the author and his team reviewed work done on Magnetic Resonance Elastography (MRE). This mechanical model was applied to study the link between rheological model and complex shear modulus complex-valued.

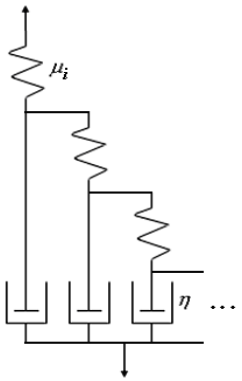

Figure 2.16: Spring-damper model with a fractal arrangement of Maxwell units. [74]

The shear modulus as a function of frequency [74] is given by:

$$G*(\omega) = G_d(\omega) + iG_1(\omega). \tag{2.2}$$

where *i* represents the spring number and, G_d and G_l relate to the rheological model to be interpreted in terms of spring constants, μ and damper coefficient, η. In other words,

$$G_d = \mu \quad and \quad G_1 = \omega\eta. \tag{2.3}$$

According to the causality principle, there exists a relationship between the dynamic and the loss modulus. However, it is suppressed in the Voigt model. The values for the constant parameters G_d and G_l in terms of frequency cannot be observed or measured from the tissue in this context. The Maxwell model provides a frequency dependent complex modulus with the corresponding G_d and G_l and exhibits a high frequency limit, capable to generate a power-law behaviour [74]:

$$G_d = \frac{\mu}{1 + \left({}^{\mu}/_{\omega\eta}\right)^2} \qquad and \qquad G_1 = \frac{\omega\eta}{1 + \left({}^{\omega\eta}/_{\mu}\right)^2}. \tag{2.4}$$

This approach has been implemented in research on breast cancer, prostate cancer and liver fibrosis [74, 75].

2.3. Modelling of Tissue/Device Interaction

Modelling of tissue/tool interaction is the study on the response of tissues when in contact with objects and devices. The dynamic properties of the tissues towards its environment can be studied and simulated using the models derived. This is a significant process contributing towards reliable and efficient surgical planning, simulation and haptic interfacing, i.e. force and position feedback during operation processes. Much of the past research work has focus more on tissue modelling. Tissue/device interaction studies are usually performed using FE modelling for both online and offline computations of dynamic attributes. Some analysis also used the dynamic modelling method. Most of the studies are extensions and implementations of the mechanical modelling of tissues. Several tool/device interaction studies are reviewed and briefly described in this section.

2.3.1. Finite Element (FE) Modelling

Needle/tissue interaction has been widely researched for the purpose of physically-based virtual planning, environment training and surgical simulation. In a needle/tissue interaction study, DiMaio et al. [76] developed a system to measure and model interaction forces occurring along the needle shaft while simulating insertions into soft tissues. Soft tissue is modelled as a linear elastostatic model that predicts tissue deformations in 2D, characterised by Young's modulus and Poisson Ratio.

The tissue is modelled as a discretised mesh of nodes using FE modelling. The measured insertion force is related to the tissue deformation, enabling the estimation of the forces along the needle. During needle insertion simulations, the force distribution along the needle at the model mesh nodes lying in the path of the needle is shown in Figure 2.17.

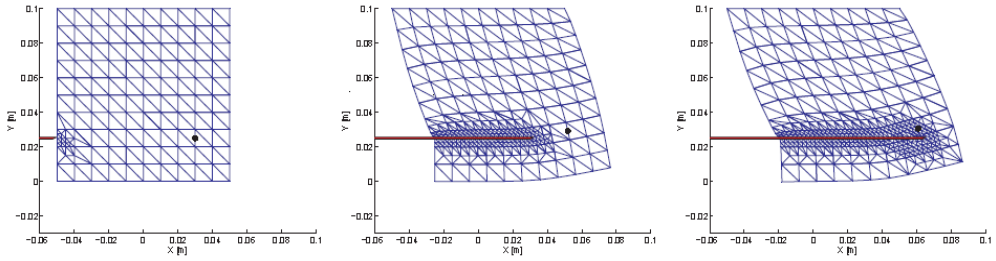

Figure 2.17: Simulated needle intercept of a small target embedded within elastic tissue. [76]

Boundary conditions and needle constraints are computed based on the simulation results, as illustrated in Figure 2.18. The local coordinate change, node interception and system expansion are also studied for system updates. As the needle travels deeper into the tissue, new nodes are generated to contact with the surrounding tissue [76]. The force and deformation distance for the new nodes which are unknown can be calculated by the system with reference to the neighbouring nodes.

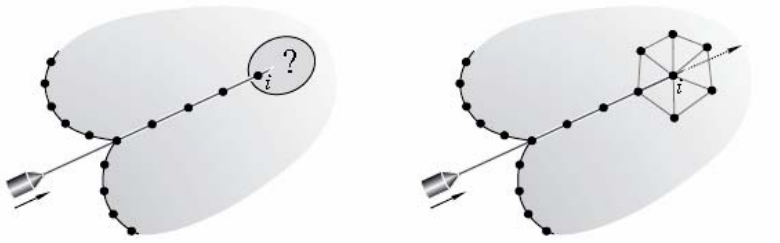

Figure 2.18: New intercept nodes are identified by searching within a small neighbourhood centred at the most distal needle node. [76]

Figure 2.19 shows snapshots taken during the virtual needle insertion simulation. The response of the interaction is visualized based on experimental deformation and force at penetration and extraction condition. This study provides a new insight on how node generation and update can be done as well as the idea on haptic feel of force, torque and deformation at the same time.

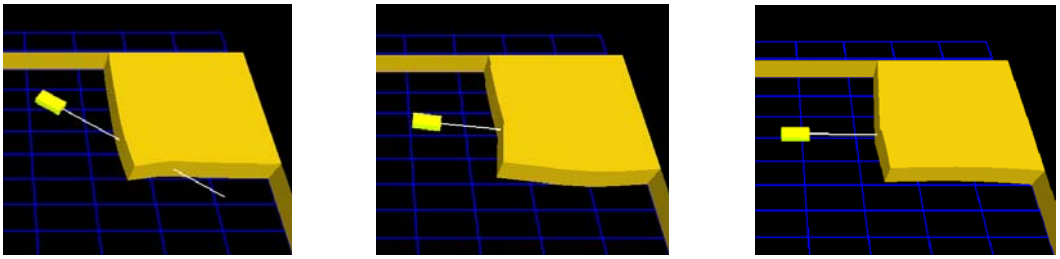

Figure 2.19: Interactive virtual needle insertion simulation in a planar environment. [76]

Besides the tissue/needle interface, much research has been performed on the models of tissue/device or tool interaction. Hansen et al. [77] modelled spatula/brain tissue interaction by using FE modelling on neurosurgery simulation, whereby spatulas are used to retract parts of the brain to access to the surgical target regions. The motivation for his study was to develop safety measures that are essential in neurosurgery. Pressures of the retractor on the brain tissues may result in ischemia due to deformation of the tissue for a finite duration, besides direct injuries like tissue tear.

Hansen et al. [77] employed FE modelling to model the brain and spatula for the computation of haptic force feedback to be fed into a surgical simulator. Hence, the pressure of the spatula onto the brain tissues can be directly felt without risking the safety of patients while learning the appropriate force for application. Brain spatula was modelled physically by triangles, as seen in Figure 2.20(a) and (b) and adding thickness to the former as shown in Figure 2.20(c). Figure 2.21 shows the brain models that were generated directly from Magnetic Resonance Imaging (MRI) scans and then segmented using the tetrahedral mesh in the FE method. Hooke's law was applied to model the interaction mechanically.

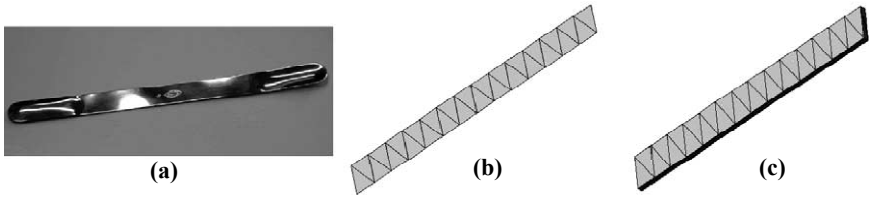

Figure 2.20: (a) Photo of a spatula. (b) Physical model. (c) Graphical model. [77]

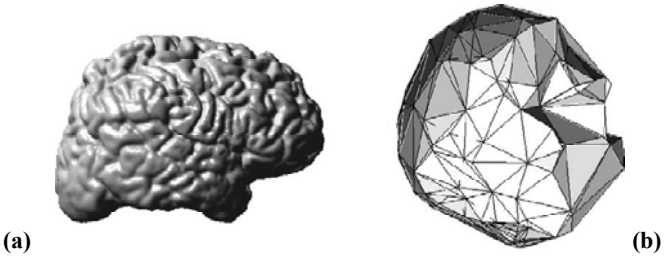

Figure 2.21: (a) Physical brain, (b) virtual representation with tetrahedral mesh. [77]

Haptic feedback and deformations, as well as collision detection and response, were computed. Analysis into the haptic feedback of forces was performed and simulations were generated. Through haptic response analysis, the response of the tissue produced by large and small spatulas was shown to affect the movements of nodes in their FE model mesh. Finally, the results obtained were applied into the simulator. The results were found to be promising with the force and visual feedback realistic. Nevertheless, improvements were suggested in considering more advanced modelling, i.e. non-linear elasticity and more advanced collision response [77].

In another study involving tissue and tool interaction, T. Chanthasopeephan et al. [78, 79] modelled the liver cutting process with a new custom-made cutting equipment. The liver cutting force was measured through the interaction with respect to the displacement of the cutting tool. A precise experimental setup capable of performing accurate data acquisition of forces and displacement of cutting tool as well as measuring cutting forces and lengths, as shown in Figure 2.22 was developed. The findings were used to investigate the properties of the liver, which then aided in the determination of the effective Young's Modulus for developing an FE model to simulate and reflect cutting forces computationally for haptic purposes.

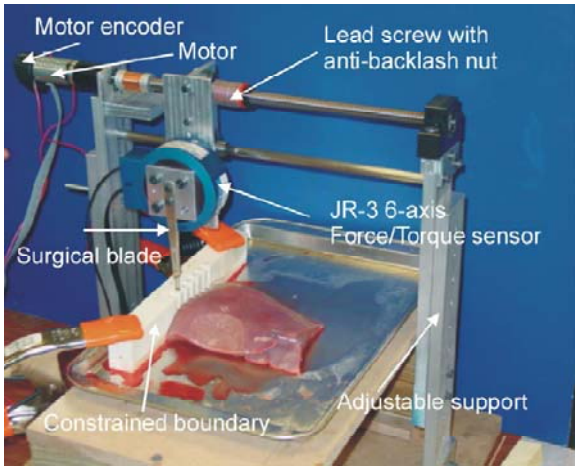

Figure 2.22: Experimental set up for force and displacement measurement. [78-80]

The experiment was performed on a fresh porcine liver harvested from the slaughter house. With cutting speeds of 0.1, 1.27, and 2.54 cm/s and a travel distance of 12cm across the fresh liver samples, the cutting force and the displacement of the surgical blade were recorded and plotted. The experimental data were then filtered to enable clearer identification of the deformation and the cut response. The graphs plotted for the unfiltered and filtered 0.1cm/sec data are as depicted in Figure 2.23. The plots show periodic responses of alternate tissue deformation and fracture of localized tissue area.

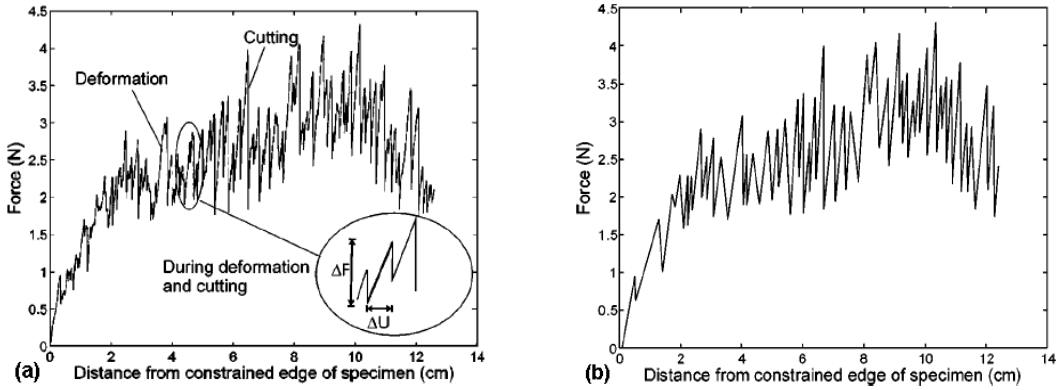

Figure 2.23: Experimental results of cutting speed of 0.1cm/sec, a) filtered data b) unfiltered data. [78, 79].

It is found that the Young's modulus for each cut is relative to the cutting speed. The iteration computation, E_{i+1}, is applied with a convergence criterion as shown in Equation (2.5) [78]. E_i is the local effective Young's modulus while $\Delta F^{EXPERIMENT}$ and ΔF^{FEM} are experimentally measured force and FE modelling computed force respectively.

$$E_{i+1} = E_i \left(\frac{\Delta F^{EXPERIMENT}}{\Delta F^{FEM}} \right) \quad whereby \quad \frac{\| \Delta F^{EXPERIMENT} - \Delta F^{FEM} \|}{\Delta F^{EXPERIMENT}} \ll 0.02 \ . \qquad (2.5)$$

The data is used to construct the two dimensional FE mesh shown in Figure 2.24 for visualization of the cutting process efficiently.

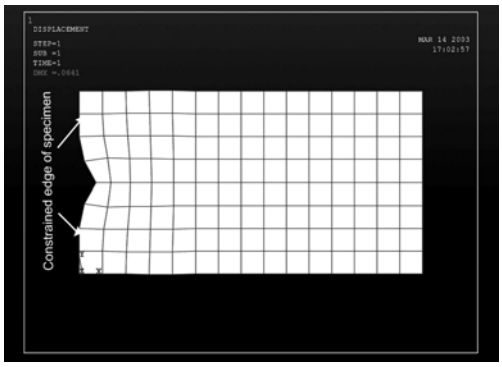

Figure 2.24: Finite element mesh constructed for deformation observation during liver cutting. [78]

T. Chanthasopeephan et al. [80] then furthered the previous research in studying the deformation of liver tissue prior to cutting. This analysis takes into account the force and deformation of the tissue with respect to the localized region. The computations of iteration process for FEM analysis and respective convergence criterion are given by Equation (2.6) [80]:

$$E_{i+1} = E_i \left(\frac{\Delta F^{EXPERIMENT}}{\Delta F^{FEM}} \right) \quad whereby \quad \frac{\| \Delta F^{EXPERIMENT} - \Delta F^{FEM} \|}{\Delta F^{EXPERIMENT}} \ll 0.01 \,. \tag{2.6}$$

Simulation on two dimensional and three dimensional FEM, as depicted in Figure 2.25 is performed to visualize the deformation profile.

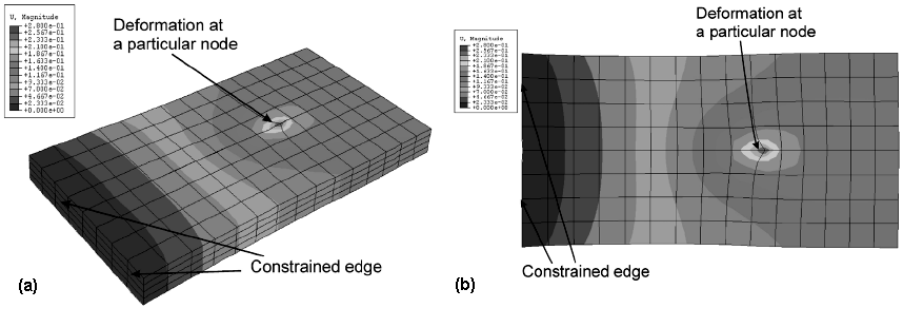

Figure 2.25: Deformation profile from (a) 3-D quadratic-element model and (b) 2-D quadratic-element plane-stress model. [80]

The work done by T. Chanthasopeephan et al. [78-80] is considerably related to the analysis in my research. Even though the authors have performed the experiments on a fresh porcine liver, the ideas and findings gained from their study greatly aid in the analysis on the cutting and deformation of coagulated porcine liver for the alternate RF ablation and division process.

2.3.2. Dynamic Modelling

While most studies employed FEM in tissue/device interaction, T. Azar et al. [81] estimated the fracture toughness of soft tissue from needle insertion by relying on the energy balance concept. Insertion tests were performed on the liver tissue using various types of needles and observations made of the resulting tissue surface crack patterns. Sample of such patterns are shown in Figure 2.26. The crack width is then used in the energy balance equation shown in Equation (2.7) to simulate the fracture toughness based on differing crack patterns [81]:

$$F\mathrm{du} + \mathrm{dU_i} = J_{IC}\mathrm{dA} + \mathrm{d}\Delta + \mathrm{d}\Gamma + P\mathrm{du}\,. \tag{2.7}$$

where F and Fdu are the force of and the work done in the needle insertion respectively; J_{IC} and J_{IC} dA the critical fracture toughness and the irreversible work of fracture respectively; dA, dΔ and dΓ the incremental crack area, the deviation in the stored internal recoverable strain energy potential and the work absorbed in plastic flow respectively; and Pdu the work done by the force P along the needle [81].

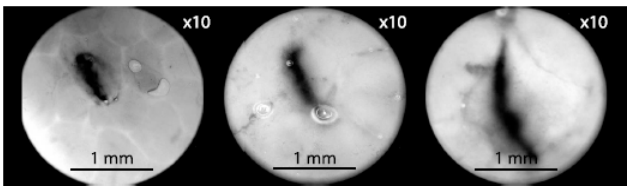

Figure 2.26: Crack size observation in the penetration test using a standard bevel needle of various diameters. From left to right, diameters of 0.71 mm, 1.27 mm, and 2.10 mm. [81]

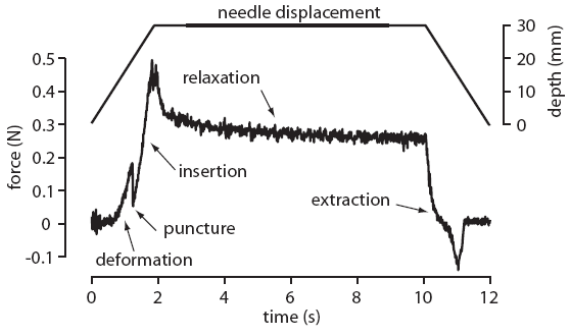

Figure 2.27: Stages of needle insertion [81, 82]

Equation (2.7) was applied in each stage of the needle insertion defined by B. Maurin et al. [82] and as shown in Figure 2.27 to calculate the force involved to

determine the fracture toughness with various crack lengths. The crack length was estimated from the penetration test performed by T. Azar with a bevel shaped needle. Through the experiment and analyses, it was found that 10% of the error in fracture toughness is estimated to be due to 10% of the error in crack size. The result seems considerably accurate given the assumptions and methods implemented. However, the viscosity of the tissue should be taken into account for a more realistic consideration.

In another dynamic interaction modelling, Rentschler et al. [83] applied the concepts of mechanical models in modelling the interaction between liver tissue and an *in vivo* wheeled robotic mobility device as shown in Figure 2.28.

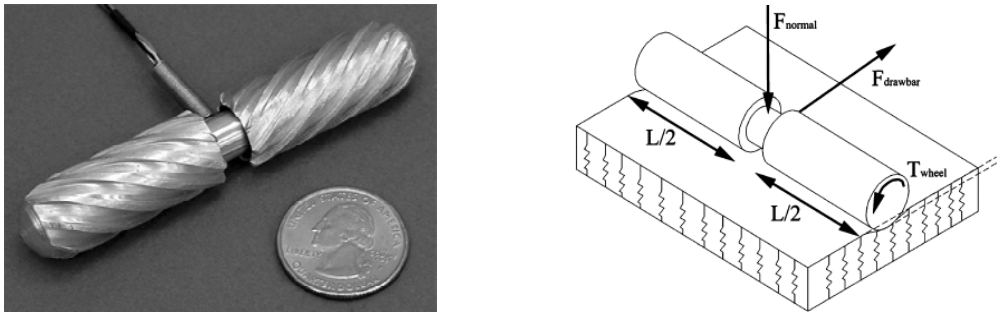

(a) (b)

Figure 2.28: (a) *in vivo* wheeled robot, (b) 3D robot model. [83]

Experiments were performed to compare the results of the interaction between the wheeled robot and the elastic and viscoelastic model of the liver tissue, as depicted in Figure 2.29.

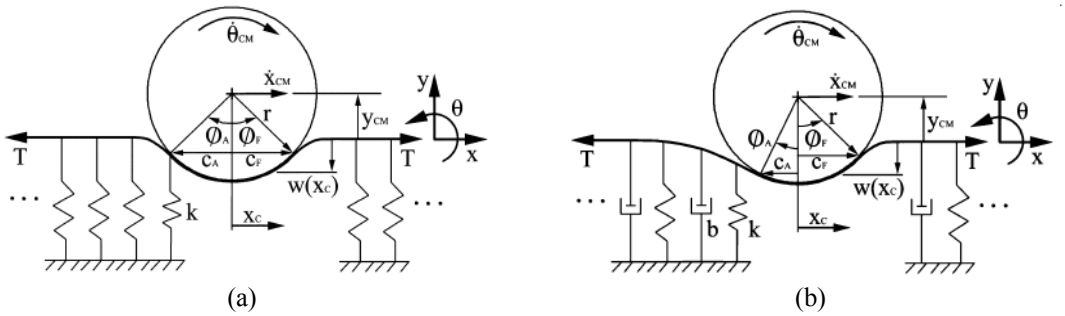

(a) (b)

Figure 2.29: (a) Elastic tissue model (k is the tissue stiffness) and (b) Voigt viscoelastic tissue model (k is the tissue stiffness and b is the viscous damping of the tissue). T is the membrane tension, r is the radius of the wheel profile, $\dot{\theta}_{CM}$ is the wheel rotation velocity, $\dot{x}_{CM}$is the wheel translational velocity, y_{CM} is the vertical wheel position, c_F and $\varphi_F$are contact length and angle in front of wheel, c_A and $\varphi_A$are contact length and angle behind wheel, x_c and w(x_c) are the x-directional contact length and its deflection respectively [83]

The elastic model was initially considered but the predicted drawbar forces were found to be much larger than the observed forces. It was assumed that through this model, the tension in the membrane could be neglected for assumption of small strains but the membrane tension was found to contribute significantly to the restoring force of the organ for larger deflections. The elastic model employed did not exhibit the energy loss due to the viscous nature of the soft tissue. Estimates of the stiffness, *k,* and the damping coefficient, *b,* of the tissue were obtained experimentally after determining the expected drawback forces for the wheels for both models. From the drawback force experiments, it was found that the viscoelastic model predicts the wheel performance more accurately than the elastic model [83].

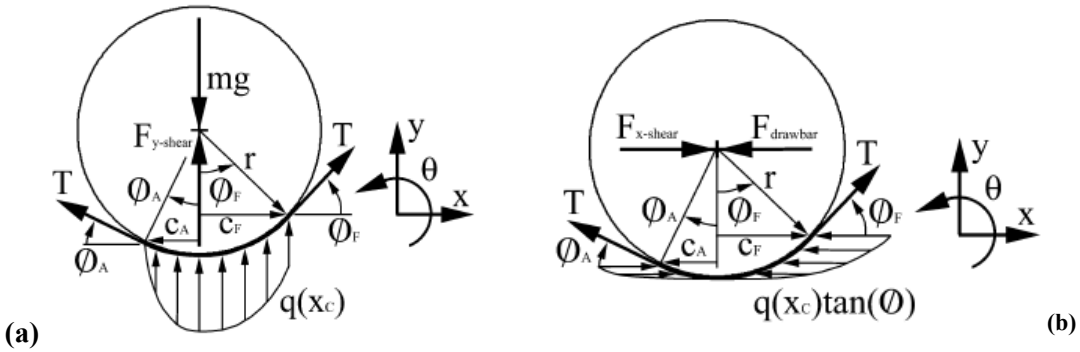

Figure 2.30: (a) Vertical forces and (b) Horizontal forces. $F_{y\text{-}shear}$ is the vertical components of the shearing of a peritoneal fluid layer between the wheel and tissue, $F_{x\text{-}shear}$ is the horizontal force generated by the wheel and organ interaction, q is the viscoelastic tissue pressure, and T is the membrane tension [83]

Rentschler et al. [83] modelled the interaction between the liver tissue and the wheeled robot by deriving the equations of motion for both vertical and horizontal forces, as illustrated in Figure 2.30. Equations (2.8) and (2.9) [21] represent the equations for vertical and horizontal motions respectively, in which $F_{x-pressure}$ and $F_{y-pressure}$ are the forces due to tissue pressure in the x and y directions respectively, membrane forces are the forces exerted on the liver tissue membrane by the wheel, drawbar force that relates to the drawbar, and shear forces that due to tissue deformation with respect to regional displacement.

$$m\ddot{x}_{CM} = -F_{drawbar} + F_{x-shear} + F_{x-pressure} + F_{x-membrane} \quad (2.8)$$

$$m\ddot{y}_{CM} = -mg + F_{y-shear} + F_{y-pressure} + F_{y-membrane} \quad (2.9)$$

Smooth wheels of various diameters were experimented with and it was found that as the diameter increases, the motion resistance caused by viscoelastic deformation reduces. This is due to the reduction in the normal pressure and sinkage [83]. A variety of wheel designs, including those with smooth, helical, brush, female and male profiles were also analysed. Even though the brush wheel performed better in manoeuvring over liver terrains, the helical wheel benefits by maintaining localised stress on the liver surface.

All the previous studies reviewed in this chapter greatly inspire and motivate the research discussed in this thesis. It is ardently hoped that the findings in this research can contribute to engineering in medicine research and to better health care.

Chapter 3: Development of Integrated Liver RF Ablation and Division Device

3.1. Device Design and Prototype

In fulfilment of the objective in this research project and thesis, a new prototype of the bipolar RF ablation device integrating a cutting mechanism was developed. The aim is to improve the hepatic surgical process by reducing surgical time and blood loss.

3.1.1. Design Concept

This new innovation assists in bloodless hepatic resection by first coagulating the liver tissue to create necrosis and then cut with a retractable surgical scalpel that is attached in the device. As seen in Figure 3.1, the new RF ablation and division device is used along with a RF generator, Rita 1500X for well-controlled ablation. The device is inserted into the liver by a surgeon, followed by the ablation process. The cutting of coagulated liver is executed thereafter, by protruding the surgical scalpel with the RF electrode in place for position securing purpose. This alternated ablation and division is performed in a desired line of resection, resulting in a convenient and less time-consuming process.

Figure 3.1: Integrated RF ablation and cutting device prototype with the RITA 1500X RF generator

3.1.2. Assumptions and Hypothesis

Several assumptions have to be made to cater for several considerations. As briefed in the background of this thesis, liver parenchyma is damaged at an instance of 60 degree Celsius during ablation of approximately 6 minutes, forming uniform coagulated necrosis. Thus, at any temperature above this margin, irreversible cell death and complete stop of blood flow is assumed. With the aid of the RF generator, ablation is performed at approximately 80 degrees Celsius and above for complete coagulation depending on the properties of liver tissue at various portions. The reasonable fixed depth of cut by the extended scalpel blade corresponding to the depth of coagulated necrosis eliminates the possibility of over-cutting into non-coagulated areas which will result in bleeding. Thus, upon coagulation, an almost bloodless and safer resection procedure with this new integrated device is promising.

It is also hypothesised that the new integrated device is beneficial in significantly reducing time loss in several aspects. The convention method is to ablate liver according to desirable resection line and manually divide in between the line of necrosis separately after the ablation. The manual process may not be accurate. Re-ablation may be needed if over-cutting happens; if so, there will already be blood loss. Re-ablation process takes up additional duration which will make the surgery process more time-consumption. Thus, with the consistent ablation and cut by the new integrated device, time loss can be eliminated.

3.1.3. Prototype Design

The inspiration of the new device evoked from the Habib 4X RF Laparoscopic device. The four RF electrodes allow bipolar transmission of current with more

precise and uniform burning besides possessing char resistance characteristic. In the new prototype design, the four RF electrodes are implemented with new incorporated mechanism for cutting. A scalpel blade is attached to this cutting mechanism which is controlled by pneumatic cylinder. A single acting pneumatic cylinder is applied in this device for it is small and light. A temperature sensor is also incorporated to monitor the ablation rate upon meeting safe appropriate cutting condition.

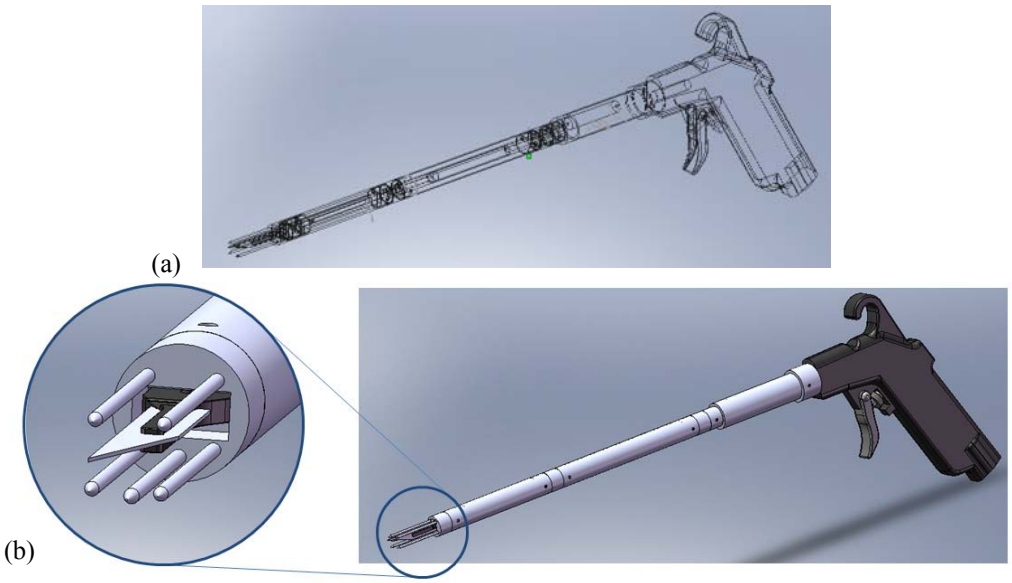

Figure 3.2: 3D prototype design, (a) wireframe view, and (b) with incorporated scalpel blade, BB511

The prototype was designed using SolidWorks 2007. Figure 3.2 shows the three dimensional assembly drawing of the integrated device. The materials used for the fabrication of this device are Delrin (Polyoxymethylene) and stainless steel type 304. Both these materials are certified by the Food and Drug Administration (FDA) for surgical use. Delrin is an engineered insulated thermoplastic that is highly resistant to water and temperature whereas type 304 stainless steel is an austenitic chromium-nickel alloy that is corrosion resistance.

The prototype consists of portions which are detachable to cater for sterilization, maintenance and extension purposes as illustrated in Figure 3.3. Replacement of parts, i.e. scalpel blade, temperature sensor and pneumatic actuator, is

made convenient with the modular characteristic. In addition, further technological and application advancement is also possible with the modularity of this prototype.

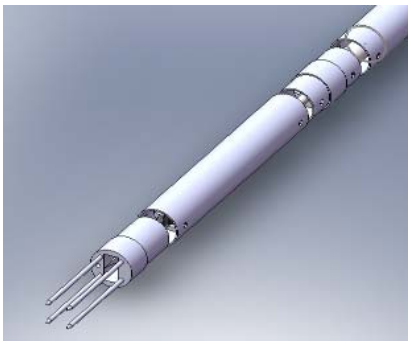

Figure 3.3: Detachability of each cylindrical part for convenience of manipulation

3.1.4. Device Specification

Figure 3.4 shows the complete RF ablation and cutting device prototype. Inside, there are four RF bipolar electrodes similar to that of Habib 4X device. The RF energy is generated by the RITA 1500X RF generator which can generate up to 250 watts. A sharp penetrable thermocouple TSS F24223 Type T which probe length of 11 inches and diameter of 1.6mm is incorporated for temperature sensing. The extension of the scalpel blade (BB511) attached to the Aesculap scalpel blade holder of size 3 is actuated by a 7mm diameter, single acting spring return air cylinder SMC CDJ2B6-60SR-B, which has a maximum pressure of 0.6MPa. This pneumatic cylinder is implemented along with a SMC SY3120-5LZD-C4 5/2 way solenoid valve connected to a 24V power supply and an initiator at the handle of the device.

Figure 3.4: Complete prototype of the new integrated RF ablation and cutting device.

The general specifications of the prototype is summarised in Table 3.1 below.

Table 3.1: Specifications of the prototype device design

Length	0.43m
Weight	0.3kg
RF Recharge time	1 second
Maximum pressure	0.6MPa
Shaft length (Insertion)	0.24m
Diameter	14mm
4 Electrodes	Length = 35mm, Char Resistant

3.2. Experiments

Experiments were performed to observe the validity and applicability of the new device prototype on an ex-vivo porcine liver. Whole fresh porcine livers were harvested from the abattoir and transported to the experiment lab in a tightly closed thermal container. The experiment setup including the new device prototype, Rita 1500X RF generator, pneumatic compressor pump, and power supplies are prepared as shown in Figure 3.5. The setup is controlled by a computer via the Labview software for temperature monitoring.

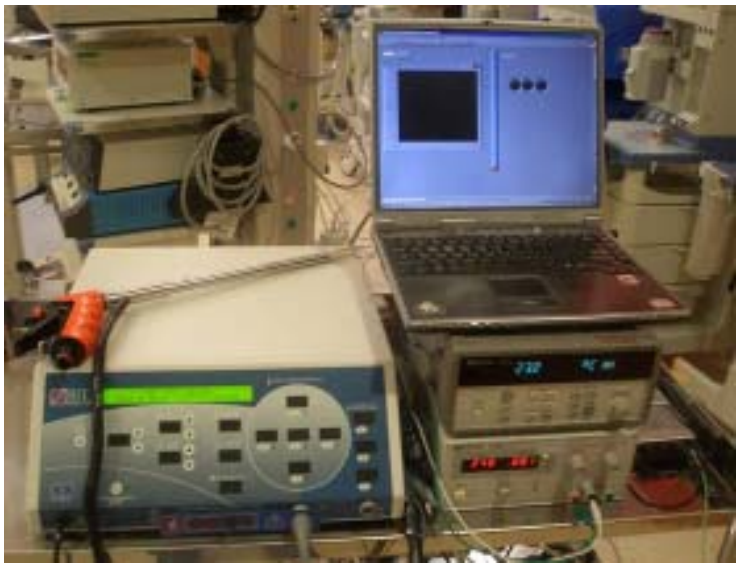

Figure 3.5: The experiment setup

3.2.1. Experiment on Unperfused and Perfused Porcine Liver

The first part of the experiment was executed on an unperfused liver lobe to observe the ablation and cutting process. The ablation was executed prior to cutting with the pneumatically extended scalpel. Figure 3.6 depicts the experiment observation, which proved the applicability of the new device prototype.

(a) 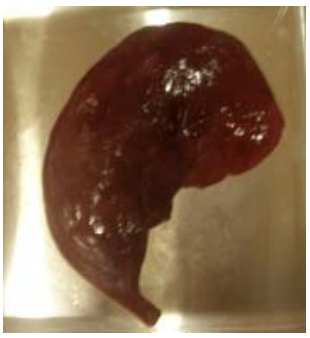 (b) 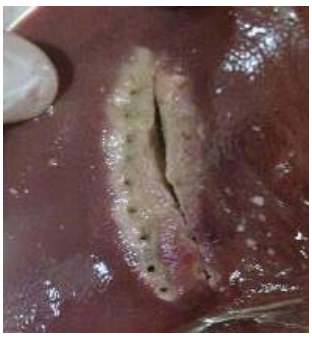 (c) 

Figure 3.6: Experiment observation: (a) unperfused lobe of a fresh porcine liver, (b) the ablated and cut liver region, and (c) break segment of the coagulated liver tissue

Next, the same experiment was performed on an entire porcine liver that is perfused using a perfusion system consisting of a pump and tank, with flowing water that simulated blood flow. The procedures are depicted in Figure 3.7.

(a) 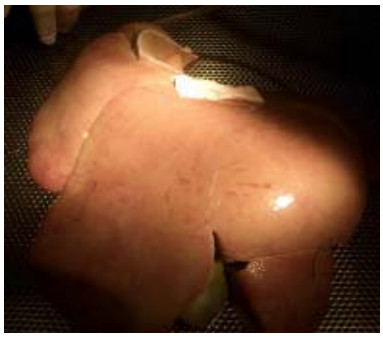 (b) 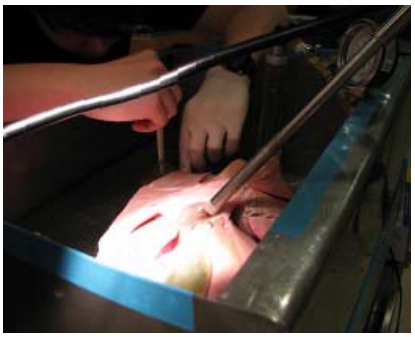

Figure 3.7: (a) An entire perfused porcine liver in the perfusion tank, and (b) application of the new RF ablation and cutting prototype

Likewise, the experiment proved successful application of the prototype. However, it takes 13 seconds to fully ablate a perfused liver tissue, which is 4 seconds longer than that on an unperfused liver. This is due to the flow of water within the perfused liver as there heat sink effect does occur. Figure 3.8 shows the experimental observation on the perfused liver.

(a) 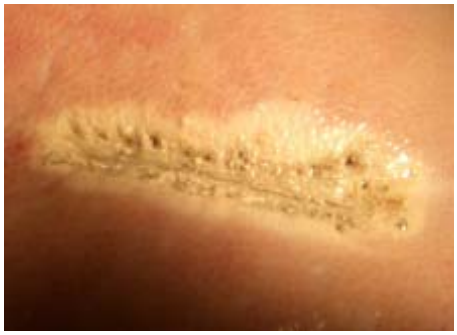 (b) 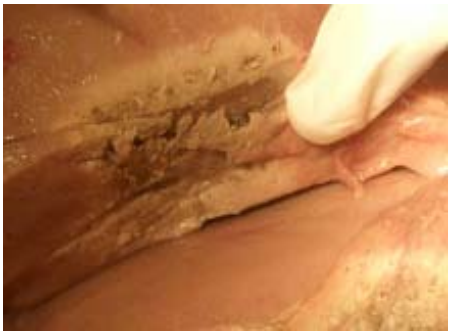

Figure 3.8: (a) The ablation and cut region on a perfused liver, and (b) dissection onto the ablated tissue

3.2.2. Execution Time Observation

The execution times between two RF-assisted resection procedures were compared. Similar to the experiments performed in the previous sub-section, the perfused porcine liver was first ablated with a Habib 4X RF Laparoscopic device and separated by manually cutting the tissue with a surgical scalpel. In the second part, the perfused liver was ablated with the new integrated RF ablation and cutting device prototype, and then an immediate cut by the pneumatic powered scalpel extension. The time execution for both the entire processes was recorded.

Visually, the effects and results on both coagulated liver tissue are alike. The duration taken to ablate both liver portions is similar as well. However, the operation time for a single procedure of ablation and cut implementing the new device prototype is at least 7 seconds faster than the other. The reason for the time deviation is because, in the separate RF ablation and manual cut, the surgeon will have to manually align and adjust the depth of the cutting on the coagulated liver tissue; a task which is dependent on the skill of the surgeon. The optimal time execution for the new device based on the experiment was about 74 seconds.

3.3. Discussions

The prototype design significantly reduces blood loss as well as the operating time for non-segmental resections during hepatic transection. With the RF ablation method, there is no concern on the methods of haemostasis. The removal of entire infected parenchyma with minimal blood loss results less operative complications. This also reduces overall hospital stay and eventually the overall costs of the intervention process.

The experiments demonstrated that the new integrated prototype device can achieve the required safety standard with a high level of reliability. The strong penetration force produced by the pneumatic cylinder assists in a guaranteed and complete division of the coagulated liver. Currently, feedback on the response of the liver tissue to the cutting process has yet been monitored. Thus, the effect of forces onto the liver tissue is not known. There exists a concern on whether the strong force produced by the pneumatic actuator will result in any impact or damage onto the liver or neighbouring organs. Hence, it is essential to identify the sufficient force required for cutting.

The issue above leads to the study of the liver tissue and cutting device interaction in this research. The response of liver tissue upon cutting enables the observations of appropriate forces required to create the break or penetration point onto the liver surface. The analysis allows a mechanical and computation model of the interaction to be developed. Prior to that, a mechanical model of the liver tissue must first be determined to aid the modelling of the interaction. These analyses and findings will benefit in surgical planning on random regions of the liver tissue.

Chapter 4: Modelling of Liver Tissue

4.1. Liver Tissue Mechanical/Material Properties

4.1.1. Constitutive Models and Equations

With reference to the objectives of this study as well as the solid assumptions discussed later in this section, the property of linearity is the main focus of this chapter. The simplest model of static reversible elastic deformation corresponds to the linear elastic model. Linearity of elasticity is assumed at two different levels. The geometrical linearity is the level with quadratic terms eliminated from the strain tensor assuming that there are only small deformations. The other level is the physical linearity in which the relation between the stress tensor and the strain tensor is assumed linear [69]. Only when displacement onto the material is minimal can the theory of linear elasticity be valid [20, 84].

Elasticity is known to be insufficient in representing soft biological tissue as the tissue body consists of not only the solid biological porous matrix, but also by large, water by wet weight. With the presence of fluid properties in soft tissue, incompressibility and viscosity has to be taken into account. Elasticity only considers the elastic nature of the tissue but does account for the energy loss in the tissue due to viscous nature. Hence, viscoelasticity is a more appropriate mechanical attribute that exhibit both viscous and elastic characteristics when undergoing deformation. Liver, like most soft tissues, combines elastic and viscous behaviours. It possesses the features of hysteresis, relaxation and creep that are called features of viscoelasticity.

Viscoelasticity can be introduced into the tensor–mass model, provided that viscous modelling is restricted to a simple linear relation. The three most widely

implemented mechanical models in tissue modelling are the Maxwell, Voigt and Kelvin models [20, 69, 70], with schematic diagrams as shown in Figure 4.1.

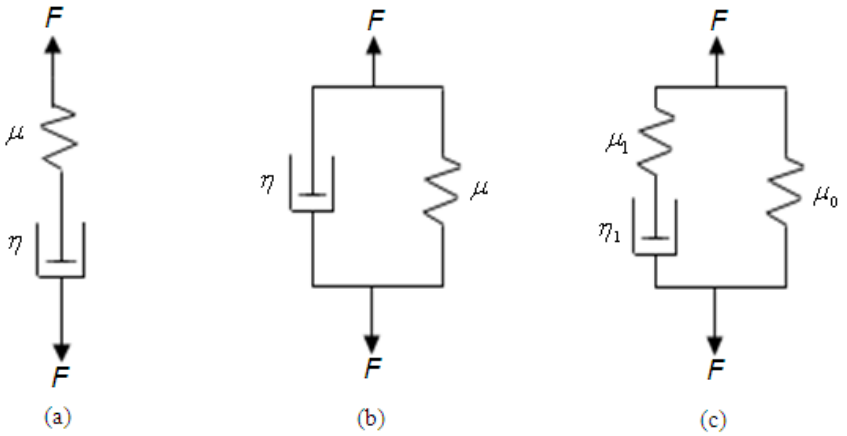

Figure 4.1: Mechanical models of viscoelastic material; (a) Maxwell body, (b) Voigt body, (c) Kelvin body.

The notations, F, η and μ_i represent the force acting on the model, viscosity coefficient of damper and spring constants respectively.

4.1.1.1. Maxwell Model

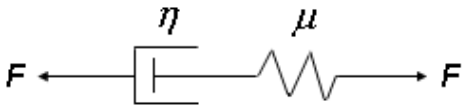

Figure 4.2: The Maxwell model

The Maxwell model in Figure 4.2 is one of the simplest mechanical models consisting linear viscous and elastic elements in series. Maxwell model essentially assumes a uniform distribution of stress. Much research especially in the fluid area implements the Maxwell model to the elastic properties that exist in real fluid. Many have applied Maxwell model onto tissue modelling as well due to the existence of viscoelastic behaviour. The velocity of deflection, $\dot{u}$ is acquired when force, F is applied to from the spring to the damper. It is the sum of the velocities of the damper and spring extension. The equation is expressed as below:

$$\dot{u} = \frac{\dot{F}}{\mu} + \frac{F}{\eta}. \tag{4.1}$$

The relaxation function *k(t)* is the force that must be applied in order to produce an elongation or compression that changes at time $t = 0$ from zero to unity and remains unity thereafter. For a Maxwell model, the relaxation function is given by

$$k(t) = \mu e^{-(\mu/\eta)t} I(t). \tag{4.2}$$

The creep function *c(t)* represents the elongation produced by a sudden application at time $t = 0$ of a constant force of magnitude unity. The Maxwell model has a creep function of

$$C(t) = \left(\frac{1}{\mu} + \frac{1}{\eta}\right) I(t). \tag{4.3}$$

where the unit-step function *I(t)* is defined as follows:

$$I(t) = \begin{cases} 1, t > 0 \\ 0.5, t = 0 \\ 0, t < 0 \end{cases}. \tag{4.4}$$

A sudden load applied results in an immediate deflection by the elastic spring, which is then followed by "creep" of the damper whereas a sudden deformation induces an immediate reaction by the spring, followed by stress relaxation based on the exponential nature. The rate of decay force in this model is characterized by the factor, μ/η and it is known as the relaxation time.

4.1.1.2. Voigt Model

In contrast to the Maxwell model, the Voigt model consists of linear spring and damper in parallel, depicted by Figure 4.3.

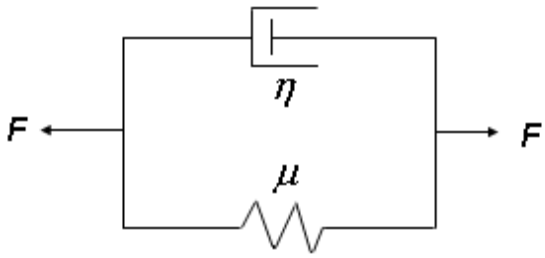

Figure 4.3: The Voigt model

Thus, displacement for both the elements is similar. Voigt model essentially assumes a uniform distribution of strain whereby strain in both elements of the model is the same and the total stress is the sum of the two contributions. The spring and damper will produce forces subjected to a given displacement. The force equation is shown as below:

$$F = \mu u + \eta \dot{u} \,. \tag{4.5}$$

If *F* is suddenly applied, the initial condition of the model will be $u(0) = 0$.

The creep function *c(t)* for Voigt model:

$$C(t) = \frac{1}{\mu}\left(1 - e^{-(\mu/\eta)t}\right) I(t) \,. \tag{4.6}$$

where the unit-step function *I(t)* is defined as follows:

$$I(t) = \begin{cases} 1, t > 0 \\ 0.5, t = 0 \\ 0, t < 0 \end{cases} . \tag{4.7}$$

while the relaxation function *k(t)* for the model is

$$k(t) = \eta \delta(t) + \mu I(t) \,. \tag{4.8}$$

A sudden load applied results in no immediate deflection. This is because there is no instantaneous motion in the damper due to its parallel arrangement with the spring. The deformation will gradually build up and the displacement of the damper relaxes exponentially. Similar to the Maxwell model, the relaxation time is given by μ / η.

4.1.1.3. Kelvin Model

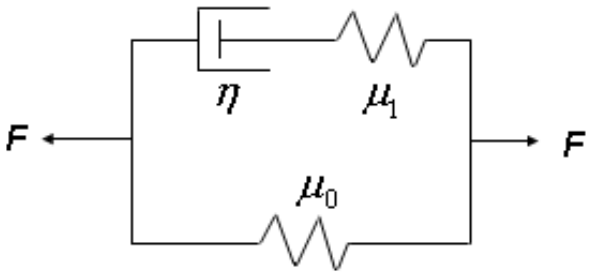

Figure 4.4: The Kelvin model

The Kelvin model also known as the standard linear model shown in Figure 4.4, is widely applied in biomechanics research as it takes into account the viscosity while keeping the computation load manageable. The linear viscoelastic model associates linear elasticity with constant viscosity. The displacements are broken down into that of the dashpot and spring, whereas the total force is the sum of the force from the spring and from the Maxwell element in the Maxwell model. The equation of Kelvin model can be written in the following form:

$$F + \tau_\varepsilon \dot{F} = E_R (u + \tau_\sigma \dot{u}) \ , \tag{4.9}$$

where

$$\tau_\varepsilon = \frac{\eta_1}{\mu_1} \ , \qquad \tau_\sigma = \frac{\eta_1}{\mu_0}(1 + \frac{\mu_0}{\mu_1}), \qquad E_R = \mu_0 \ . \tag{4.10}$$

τ_ε and τ_σ are known as relaxation times for constant strain and constant stress respectively. E_R is commonly referred to as the relaxation modulus.

The creep function, *c(t)* for a standard linear model is:

$$c(t) = \frac{1}{E_R}\left[1 - \left(1 - \frac{\tau_\varepsilon}{\tau_\sigma}\right)e^{-1/\tau_\sigma}\right] I(t) \ . \tag{4.11}$$

where the unit-step function *I(t)* is defined as follows:

$$I(t) = \begin{cases} 1, t > 0 \\ 0.5, t = 0 \\ 0, t < 0 \end{cases} . \tag{4.12}$$

while the relaxation function *k(t)* for a standard linear solid is,:

$$k(t) = E_R \left[1 - \left(1 - \frac{\tau_\varepsilon}{\tau_\sigma} \right) e^{-1/\tau_\sigma} \right] I(t) . \tag{4.13}$$

In Equation (2.13), τ_ε is the time of relaxation of load under the condition of constant deflection. τ_σ is the time of relaxation of deflection under the condition of constant load. As *t* tends to 0, the load-deflection relation is characterized by the constant E_R and hence, it is the relaxed elastic modulus or relaxation modulus.

4.1.2. Stress/Strain Relationship

The static behaviours of a material; likewise, soft tissues, is characterised by the stress/strain relationship. It describes the response on the material under mechanical process and load. Through this relationship, the properties and characteristics of the materials can be computed and established.

Stress corresponds to the amount of force exerted onto a surface area. A specimen with larger surface area can sustain bigger force as compared to one with smaller surface area. However, the critical consideration is the force relating to the surface area of the specimen, but not the size itself. Thus, the important notion is to find the force per unit area, the actual definition of stress (σ), denoted by Equation (4.14) below, by which *F* is the exerted force and *A* is the cross sectional surface area.

$$\sigma = \frac{F}{A} \, (N/m^2) \; or \; (Pa) \quad where \quad (1\,N/m^2 = 1MPa) . \tag{4.14}$$

The length of specimens is corresponding to the strain properties. In general, strain is the ratio of the displacement of any deformation onto a material over the original length. In tissue manipulation, strain (ε) is specifically the amount of deformation, or tensile or compression displacement over the actual length or height of the tissue specimen, given by Equation (4.15); L is the original length or height and L_o, the displacement. It is a dimensionless entity due to the cancellation of units.

$$\varepsilon = \frac{L - L_o}{L}. \tag{4.15}$$

In uniaxial tests, soft tissues are subjected to uniaxial loading; either elongation or compression test along a single axis direction, to study the stress/strain relationship. The stress/strain relationship allows proper selection of strain for determination of appropriate stress in an analysis. Under the unaxial load, the stress and strain of a material is proportional to one another, as shown by Equation (4.16). In this case, the strain is infinitesimal and the selection is less complex. Equation (4.16) abides by the Hooke's law with the constant value, E being denoted as the Young's modulus. This parameter is essential for the computation of FE models.

$$\sigma = E\varepsilon. \tag{4.15}$$

The stress/strain relationship for soft tissue exhibiting linear response is also linear. Nevertheless, for soft tissue under large deformation, non-linear stress/strain characteristics must be taken into account [20]. In a stress/strain relationship, the stress is related to the speed of deformation, which is the strain rate. This is another valid reason to take into the viscous nature of soft tissue consideration; the deformation of the soft tissue does not only rely on their instantaneous values, but also the history of the applied forces [84]. The typical stress/strain relationship curves for elongation and compression are visualized in Figure 4.5.

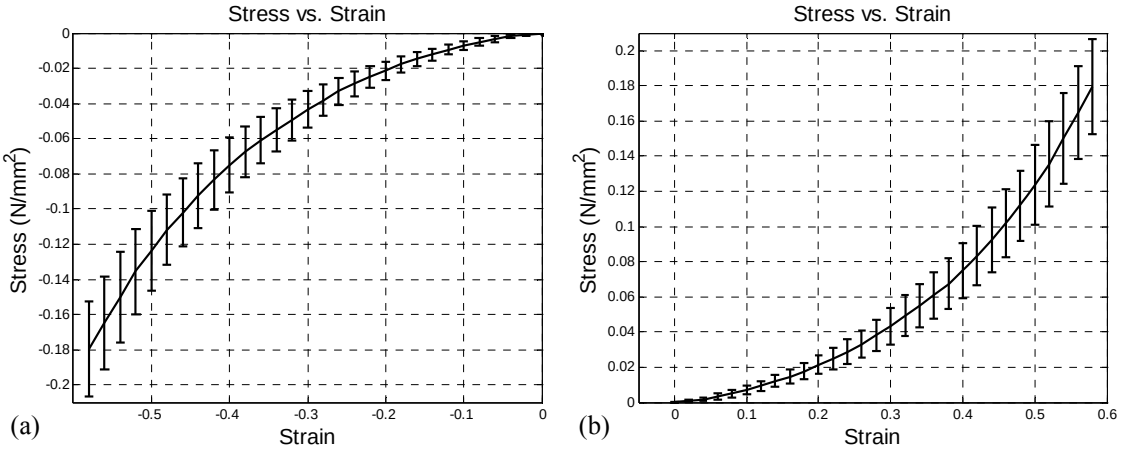

Figure 4.5: Example visualization of stress/strain relationships, (a), compression and (b) elongation.

The stress/strain relationship of a material can be investigated over a series of tissue specimens grouped with consistent mass density. Among different experimental process, the variation in mass density is insignificant as the relationship of stress/strain is generic for the tissue properties determination. The parameters and attained models can be applied for general computations and comparisons.

4.1.3. Assumptions and Hypotheses

Several assumptions were made to assist this study on the modelling of the liver tissue, which will be extended to the analyses of tissue/device modelling in later chapter. Biological tissues, like any other materials, can be models via dynamic models by mechanical components. The common mechanical systems in applications are the spring-mass or tensor-mass systems, whereby the use of spring, mass and damper models is involved. Soft tissue exhibits both elastic and viscous nature, demonstrated by springs and dampers respectively. The fundamental mechanical configurations discussed have been widely used to represent soft tissue models.

Often, modelling of soft tissue becomes complex as the response portrays non-linearity. Some studies have shown that soft tissues can be modelled as linear models

[85], while others, non-linear [56, 67]. Fung [20] developed the Quasi-Linear Viscoelastic model for soft tissue, taking into account the linearity at minimal deformation (approximately 10% strain) and non-linearity at large deformation. The theory of linearity assumption of soft tissue due to minimal deformation is also applied by [63, 84]. In this study, my goal is to achieve minimal deformation prior to the break point of the surgical scalpel blade penetration. Thus, the analyses performed in this study implement the characteristics of a linear model.

The response of the liver tissue is hypothesized to vary at different deformation forces and deformation speeds. Larger force provides shorter time to reach desired deformation displacement. Likewise, faster deformation speed as well. Hence, to achieve minimal deformation at fastest time instance, the deformation force and speed should be sufficiently large. The minimal deformation will be focused at 10% strain applied onto the liver from the surface.

In addition, since the characteristics of a fresh non-coagulated tissue vary from that of a coagulated one, the required deformation speed and force to reach a strain of 10% are different for both cases. The responses of both fresh non-coagulated and coagulated liver tissue will be investigated and discussed in subsequent sessions.

4.2. Non-coagulated Liver Tissue

4.2.1. Experiments

The stress/strain analysis of fresh, non-coagulated liver tissue has been performed by Chui et al. in several of their studies. In one of their work [11], a non-linear model of a fresh porcine liver tissue for surgical simulation purposes is derived from the compression following elongation experiment. Chui et al. [86] analyses the non-linearity of the liver tissue under large deformation, the liver tissues is characterized as quasi-incompressible, non-homogeneous, non-isotropic, non-linear viscoelastic materials.

The experiments are performed on a fresh porcine liver directly from the abattoir. Porcine liver is selected for the analysis as it closely approximates the liver properties of human. The liver specimens are extracted from various portion of the whole porcine liver with the dimensions of approximately 7mm in diameter and 10mm height as pictured in Figure 4.6. The specimens are kept fresh in room temperature and are glued onto the experimental probes by surgical adhesive. The force and displacement were measured during loading test by a precision instrument named Eztest from Shimadzu Co Ltd of Japan.

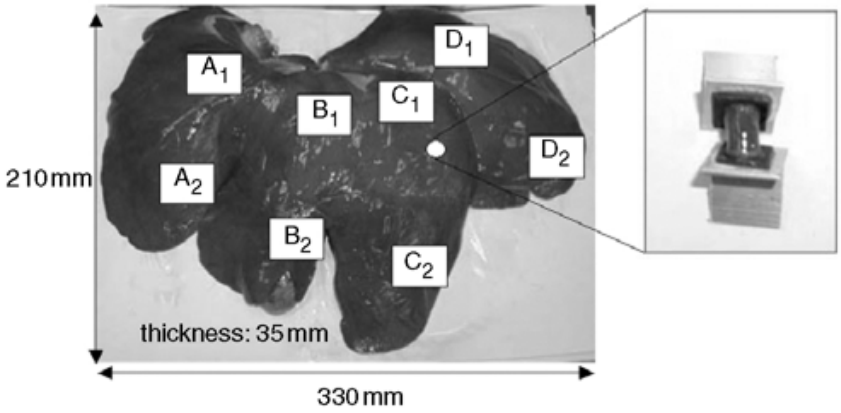

Figure 4.6: Liver specimens extracted from various parts of porcine liver [11].

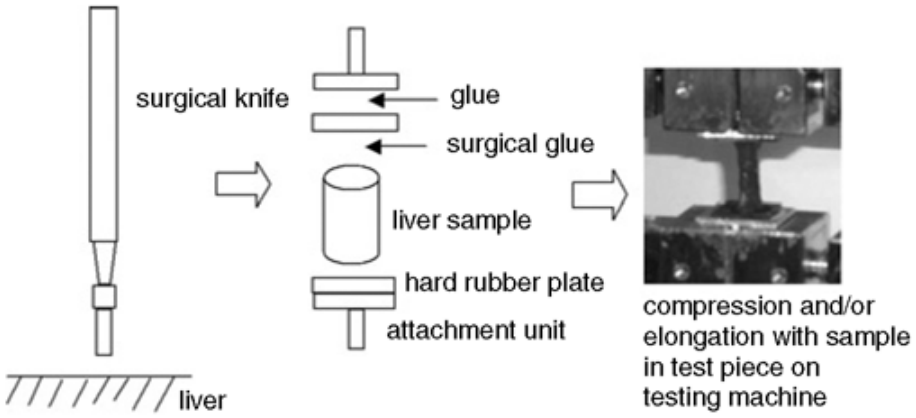

Figure 4.7: Preparation of specimens for experimental set up [11].

Figure 4.7 depicts the process of the specimen preparation and the experimental setup for the elongation and compression experiments. Similar experimental setup and procedures are implemented to derive the mechanical model of the liver tissue. Uniaxial compression tests were performed to attain the force and displacement data against time, as well as the stress/strain relationship. During relaxation test, the liver specimen was stressed at a strain rate of 10 mm per minute to the peak. Then the moving head of the testing machine was suddenly stopped so that the strain remained constant. The data of forces and displacements versus time were recorded.

4.2.2. Stress/Strain Relationship

The experiments performed on fresh, non-coagulated liver tissue enable the determination of the stress/strain relationship. The stress/strain relationship for the non-coagulated liver tissue is attained by plotting the stress versus strain curve as shown in Figure 4.8. The stress/strain relationships of several random samples are grouped to compute and plot the mean as well as standard deviation. It can be seen that for the non-coagulated liver tissue, a stress of approximately 0.175 N/mm^2 is required to reach a strain of around 0.37.

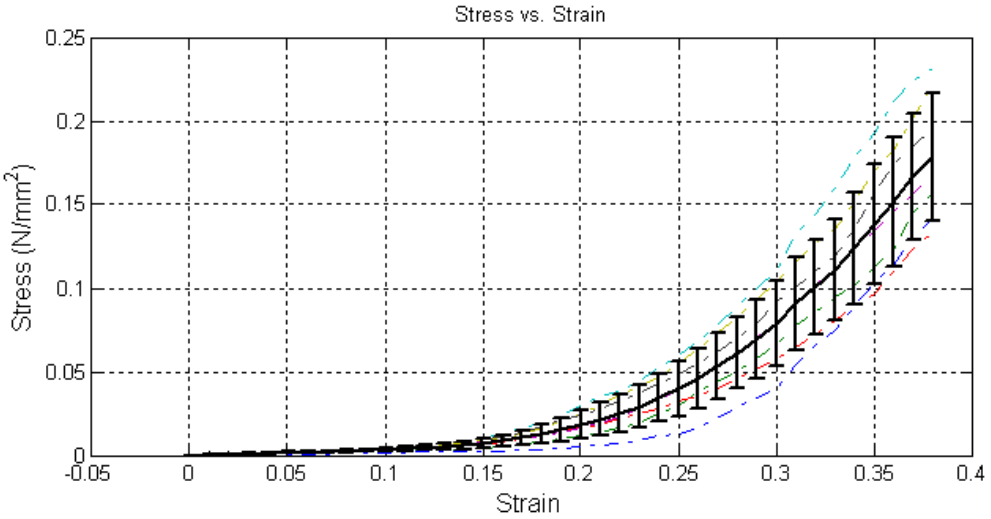

Figure 4.8: Stress/strain relationship of non-coagulated liver tissue.

Through this relationship, the properties of the fresh, non-coagulated tissue can be compared and studied along with that of the coagulated tissue. From these observations, the comparisons made allow the comprehension on the difference between the two mechanical and material properties.

4.2.3. Analysis of Non-coagulated Tissue Mechanical Properties

The relaxation response of the tissue specimens acquired from the experiment is then plotted force against time and the mean of all curves are generated as shown by the black cubic polynomial line in Figure 4.9. The curve is then analysed and curve fitted via the curve fitting process in MatLab to determine the function that closely approximate the response. It is found that the relaxation function of Kelvin model, as seen in Equation (4.9) closely relates to the relaxation of the compressed tissue, as depicted by the smooth blue curve above the original plot in Figure 4.9.

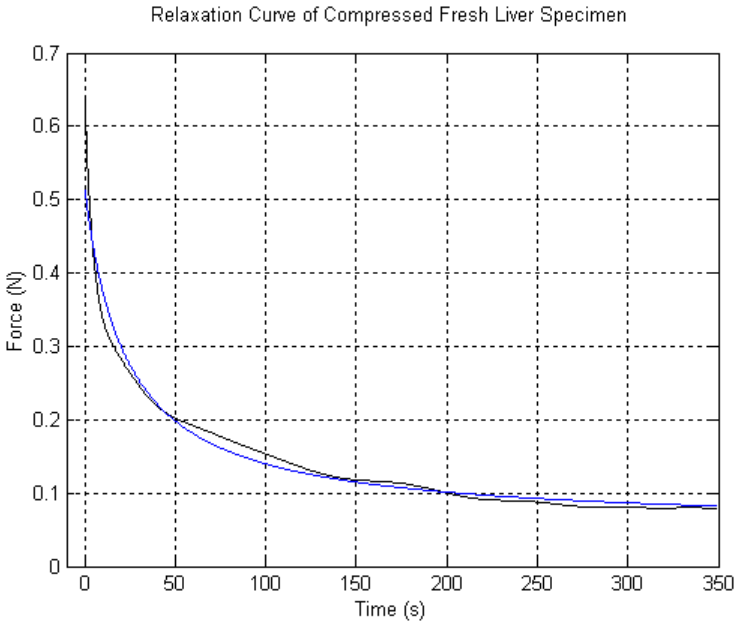

Figure 4.9: Comparison of results from relaxation experiment after compression with theoretical prediction from the Kelvin model [86].

Through curve fitting, the parameters of the equations are generated and tabulated in Table 4.1. These values represent the spring constants and damper coefficient in Kelvin model and are useful in deriving desired tissue dynamic model. These parameters then enable the calculations of the relaxation time for constant strain and stress as well as the relaxation modulus of the standard linear model. The relaxation parameters are computed by using Equations (4.10) and the resultant values are as shown in Table 4.2.

Table 4.1: Material parameters of standard linear model, derived from the relaxation function based on the compression test [86].

μ_0	μ_1	η_1
45.9	293.2	2035.7

Table 4.2: Relaxation parameters of standard linear model, derived from Equations (4.10) based on the values obtained in Table 4.1 [86].

Relaxation Time for constant stress (sec), $\boldsymbol{\tau_\sigma}$	Relaxation Time for constant strain (sec), $\boldsymbol{\tau_\varepsilon}$	Relaxation Modulus, $\boldsymbol{E_R}$
6.9	51.2	45.9

These parameter values are applied in aiding the determination of the mechanical model and equations for the non-coagulated liver tissue.

4.2.4. Proposed Mechanical Model

Physically, as liver is of linear viscoelastic material, Kelvin model will be able to suitably approximate closely its mechanical behaviour. Kelvin model is assumed to be a sufficient model in this study as very minimal deformation is required, resulting in minimal stress relaxation and creep function effect. The curve fitting performed by Chui et al. [86] onto the relaxation functions shows that the physical model of liver tissue can be modelled as standard linear model or Kelvin model. A refined mechanical model of the fresh liver tissue is then constructed according to the earlier findings and parameters.

Figure 4.10 pictures the proposed fundamental mechanical model of the non-coagulated liver tissue. A virtual mass is place at the point in which the external force, F is exerted and another in between spring, μ_1 and damper, η_1 to cater for the change in displacement. The Kelvin model can be visualised as an extended entity which is supposed to be within the liver.

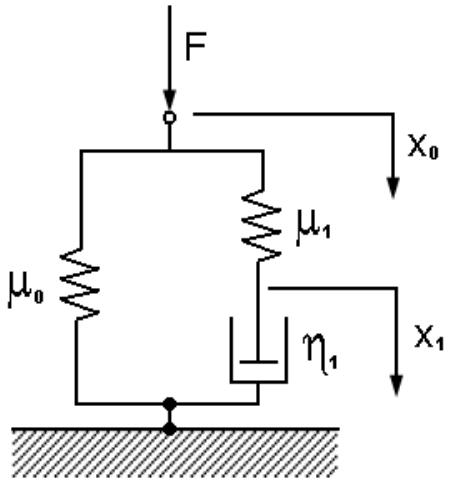

Figure 4.10: Proposed model of non-coagulated liver tissue implementing the Kelvin model.

According to the model above, the mechanical equations or equations of motions is derived as below. In this context, F is the compression force at displacement, x_0 and x_1 is the displacement due to a virtual mass in between μ_1 and η_1, as per mentioned previously.

$$x_0 = \left(\frac{\mu_1}{\mu_0 + \mu_1}\right) x_1 + \frac{F}{\mu_0 + \mu_1}, \tag{4.16}$$

$$\dot{x}_1 = \frac{\mu_1}{\eta_1} x_0 - \frac{\mu_1}{\eta_1} x_1 . \tag{4.17}$$

Upon substituting the values of parameters obtained via previous curve fitting analysis, Equations (4.16) and (4.17) are then simplified as follows:

$$x_0 = (0.865)x_1 + (0.00295)F , \tag{4.18}$$

$$\dot{x}_1 = (0.144)x_0 - (0.144)x_1 . \tag{4.19}$$

These two equations are very useful in analysing interaction onto the non-coagulated liver tissue in the next chapter. The parameters, such as force, F as well as the displacements, x_0 and x_1 will be considered when this model is applied onto interaction models.

4.3. Coagulated Liver Tissue

This section discusses in depth about the work and analysis performed onto the coagulated liver tissue. This is an essential study as a majority part of this work involves coagulated liver tissue. Thus, the material properties in this part significantly aid in later chapters in this thesis.

4.3.1. Experiments

The mechanical properties of a coagulated liver tissue are investigated. Another experimental setup is utilised for the compression tests to be performed with coagulated liver specimens. From fresh porcine harvested, at least 30 samples of coagulated liver specimens were extracted from ablated portions of several fresh porcine livers. The livers were first ablated at various portions of each lobe (A, B, C, and D, as depicted in Figure 4.11), using either the Habib 4X Laparoscopic RF ablation device or the new prototype of integrated RF ablation and cutting device.

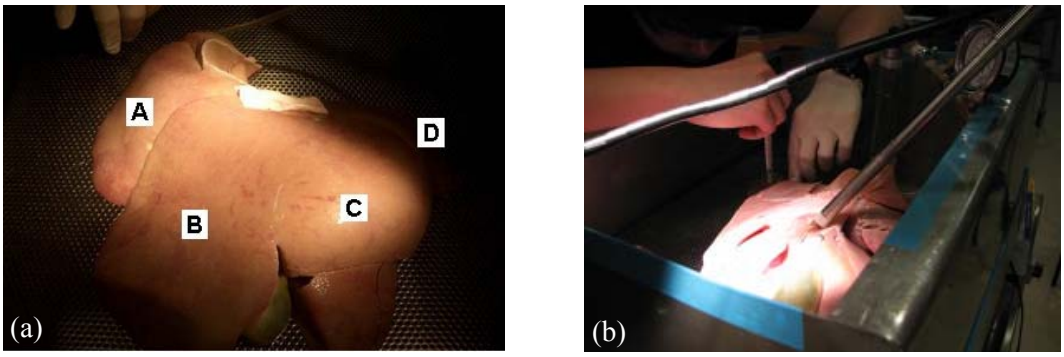

Figure 4.11: (a) Perfused porcine liver for desired ablation at lobe A, B, C and D, and (b) ablation process using the new RF ablation and cutting prototype.

An aluminium tissue cutter with sharp tapered end with inner diameter of 10mm is fabricated to mould the liver specimens into consistent diameter and careful height measurements (10mm) are taken to ensure that the mass are consistent as well (approximately 0.7g per specimen). The specimens are then glued onto thin rubber

pieces with the tissue adhesive, Histoacryl® by B Braun Aesculap. The rubber pieces are attached to the tissue holder with normal glue prior to the attachment of the liver specimen. Figure 4.12 shows the preparation of the tissue specimens for the tests.

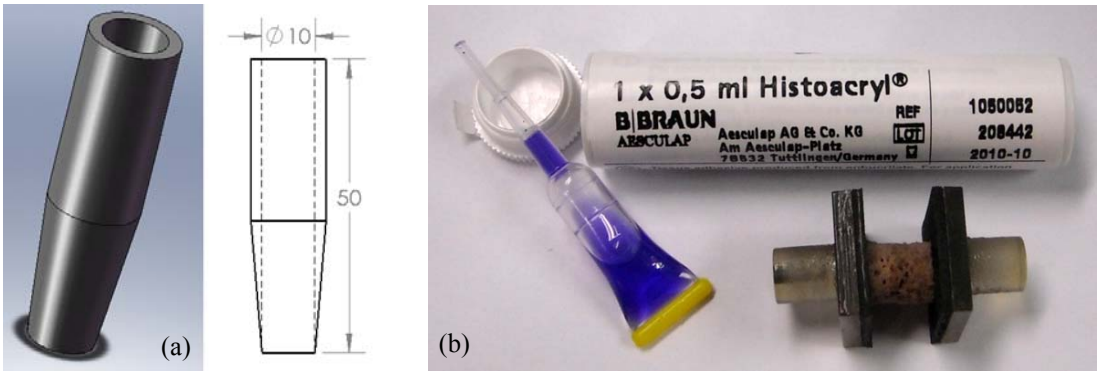

Figure 4.12: (a) Aluminium tissue cutter of 10mm inner diameter, and (b) tissue specimen glued onto tissue holders by Histoacryl®.

The tissue holder with the specimen is then fastened onto the experimental setup with one end held in place by a 9 mm clamper and the other screwed onto a 15N UF1 Isometric force sensor from LCM Systems Ltd. The experimental setup (Figure 4.13) is actuated by a bipolar CTP21 stepper motor which controls the XYZ direction of translational stages. For compression test as shown in Figure 4.14, only the uni-direction Y is required to drive the force sensor upwards and downwards. With a constant deformation speed of 1mm/sec, each specimen is compressed strain of 0.7 and held in position for approximately 20 minutes to acquire the relaxation data.

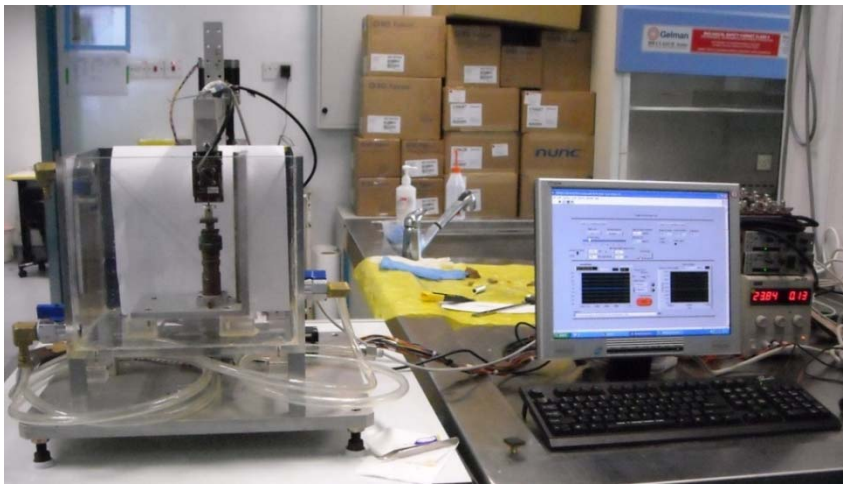

Figure 4.13: Entire experiment setup connected to the computer, data acquisition card, and amplifiers

(a)  (b) 

Figure 4.14: (a) The liver specimen attached to the force sensor, and (b) the liver specimen under compression for approximately 20 minutes.

The system is controlled by the LabView software that is directly interfaced with the data acquisition card (DAQ), connecting to the experimental setup. The settings are as previously explained and are pictured in Figure 4.15 below. The data for force and displacement over time is recorded and plotted for analysis in the subsequent sub-section. The stress/strain relationship for the coagulated liver under compression is also defined through the data acquired.

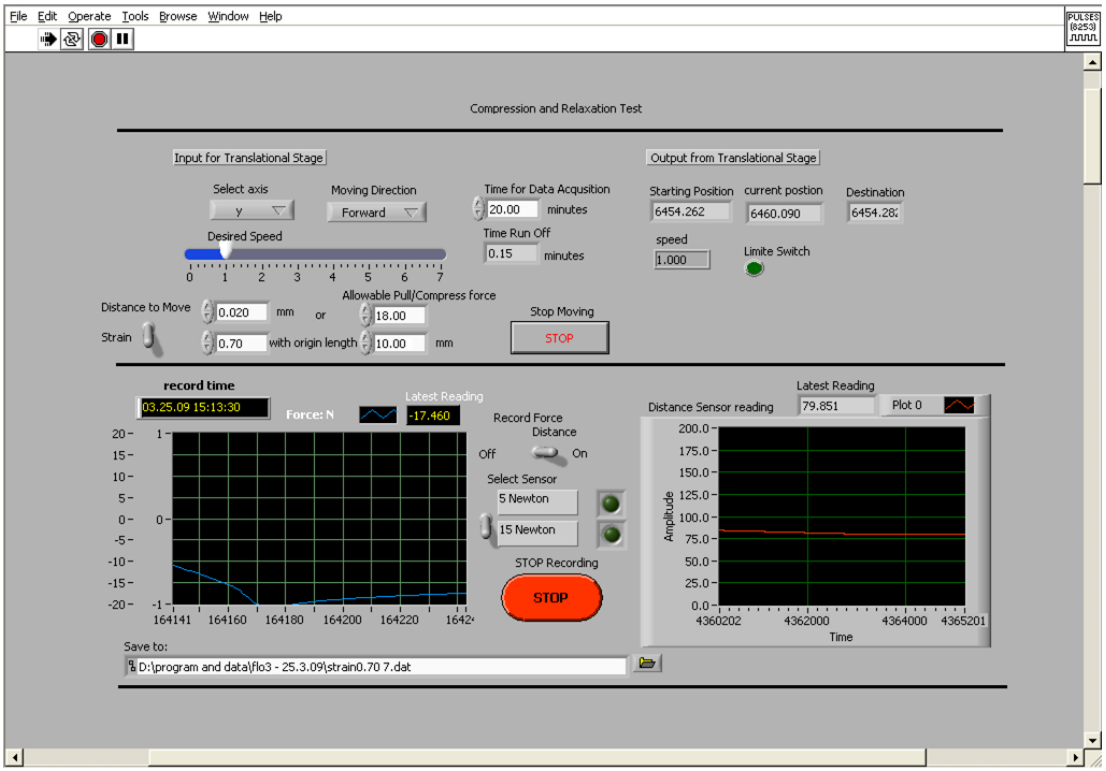

Figure 4.15: The GUI in LabView for calibration and the experimental data acquisition.

4.3.2. Experimental Results

The experimental data were plotted as shown in Figure 4.16. The responses seemed to be fairly consistent. It is observed that the constant strain of 0.7 is reached in short instance of barely 7 milliseconds, by which the compression forces vary with only small deviations along the time duration. The relaxation response of each specimen continues gradually even after the experimental time of 20 minutes.

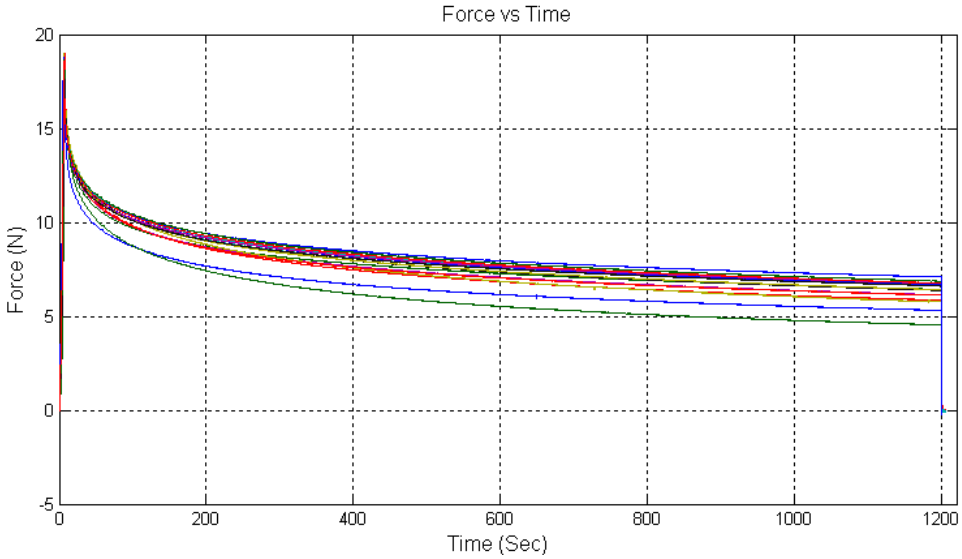

Figure 4.16: Response of coagulated tissue specimens in compression experiments.

These data are then filtered to visualise only the relaxation portion of the responses. The curves are matched by taking the ratio of force at a specific time instance over the highest force value of the similar response, so that all curves start from the initial time at same force ratio of value 1. This is mainly for the purpose of mean and standard deviation calculation of the responses. The resultant mean and standard deviation responses are pictured in Figure 4.17, with the mean and standard deviation plot depicted by black curve and bars respectively. Obviously, it is shown that the responses are considerably close to each other, mostly being within the standard deviation determined.

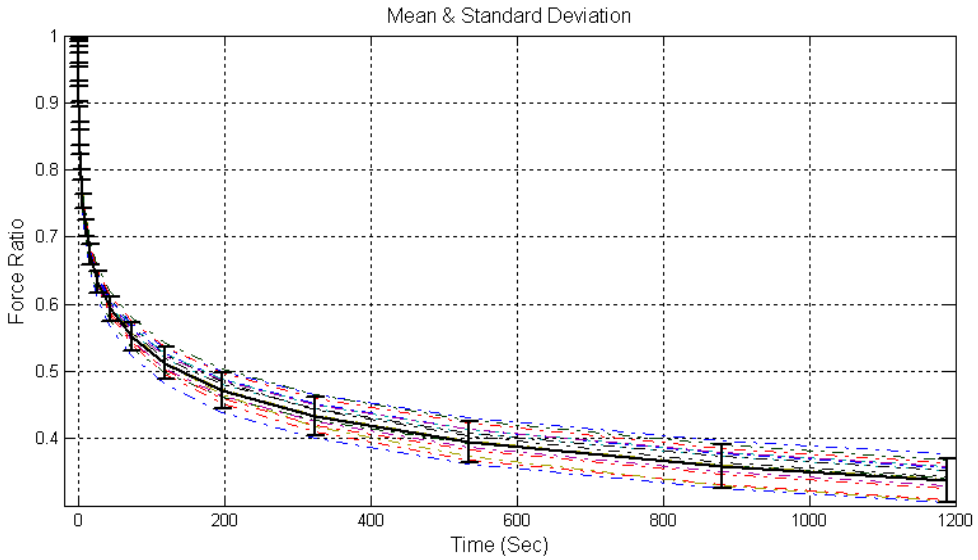

Figure 4.17: Means and standards deviations of the experiment data.

The mean and standard deviation curve is then recalibrated to the actual scale of force (N) by multiplying with the mean of all forces at strain of 0.7. The mean and standard deviation then represent the actual force versus time data as in Figure 4.18.

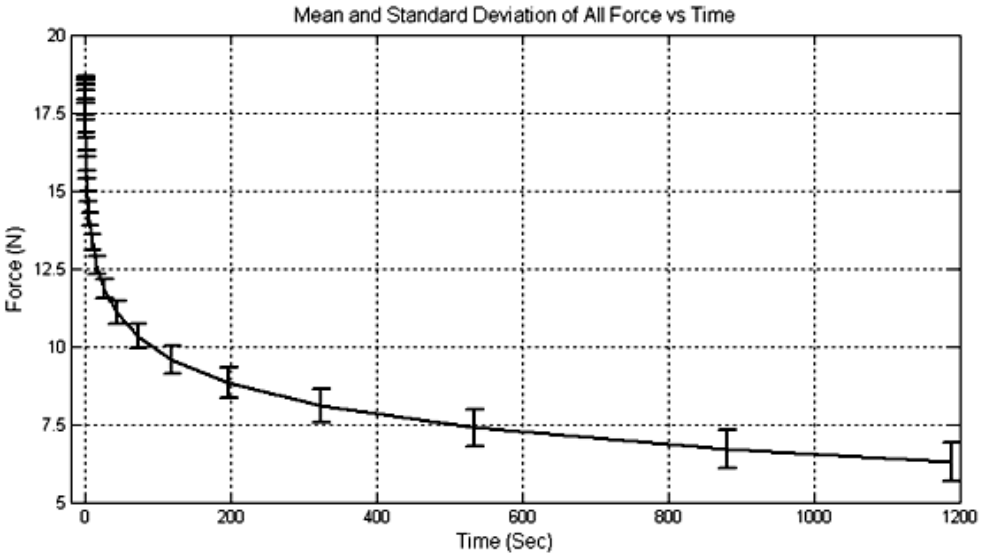

Figure 4.18: True mean and standard deviation of the compression response.

The actual mean relaxation data facilitates in determining the mechanical model closely represents the response. This process is accomplished through curve fitting by applying the *cftool* toolbox in MatLab. The analysis is discussed in the subsequent sub-section.

4.3.3. Stress/Strain Relationship

The experimental data enables the stress/strain relationship of the response to be plotted, as depicted by Figure 4.19. The compression forces are divided by the area of the specimens (*F/A*) to obtain the stress values while strain values are computed by dividing displacements with the original height of the specimens *(Δl/L)*. The stress/strain relationship of each selected responses portray to be considerably close to one another. The mean and standard deviation of the grouped responses are computed and plotted. At strain of approximately 0.58, the average acquired stress is about 0.18 N/mm^2.

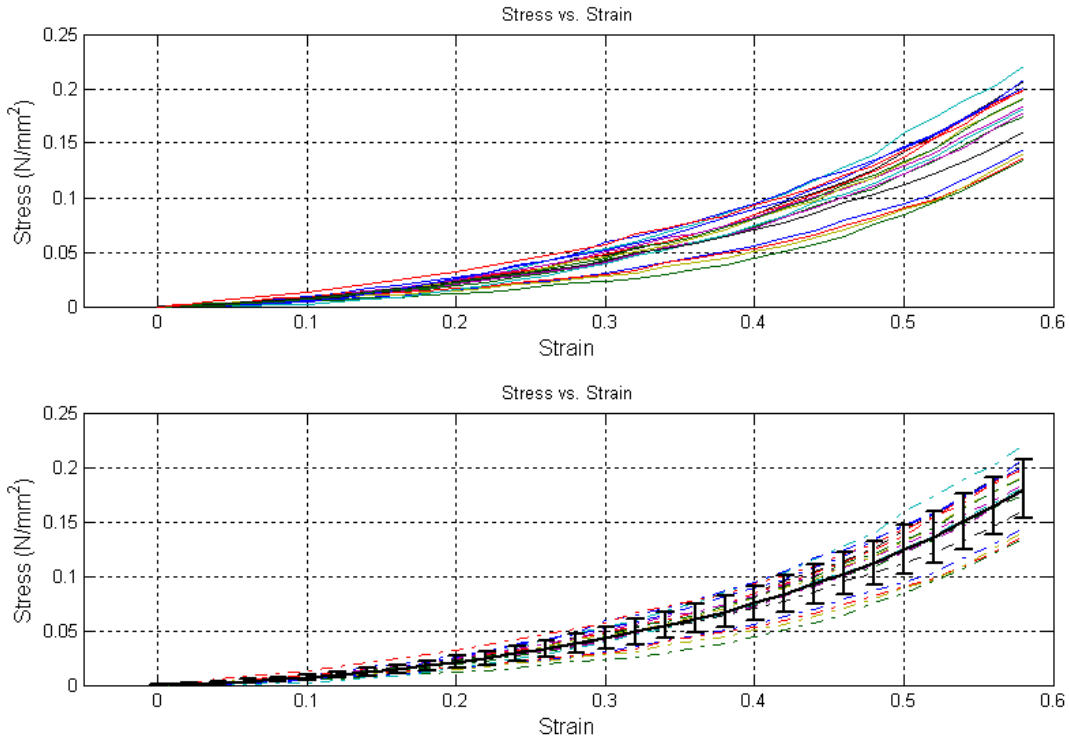

Figure 4.19: Stress versus Strain responses of the coagulated liver tissue specimens.

The stress/strain relationship of the coagulated liver tissue could be compared with that of the non-coagulated tissue.

4.3.4. Analysis of Coagulated Tissue Mechanical Properties

The first step to this analysis is the curve fitting process whereby equations of closely related linear models are fitted and matched on the previously attained relaxation response. Since the non-coagulated liver tissue closely relates to the Kelvin model, the similar equation is tested on the coagulated tissue response to observe the closeness of fit. Equation (4.9) is derived to obtain the ODE solution given in Equation (4.20). The variables are forces (*F(t)*) and time (*t*) instances of the response which is given in the experimental data. The strain was kept constant for approximately 20 minutes for relaxation observation; thus, the compression displacement (*u*) is constant. The parameters, μ_1, μ_0 and η_1 are the spring constants and damper coefficient, which are required to be determined via curve fitting. Equation (4.20) is then fed into *cftool* in MatLab for curve fitting analysis.

$$F(t) = F(0)e^{-t\frac{\mu_1}{\eta_1}} + \mu_0 u\left(1 - e^{-t\frac{\mu_1}{\eta_1}}\right). \tag{4.20}$$

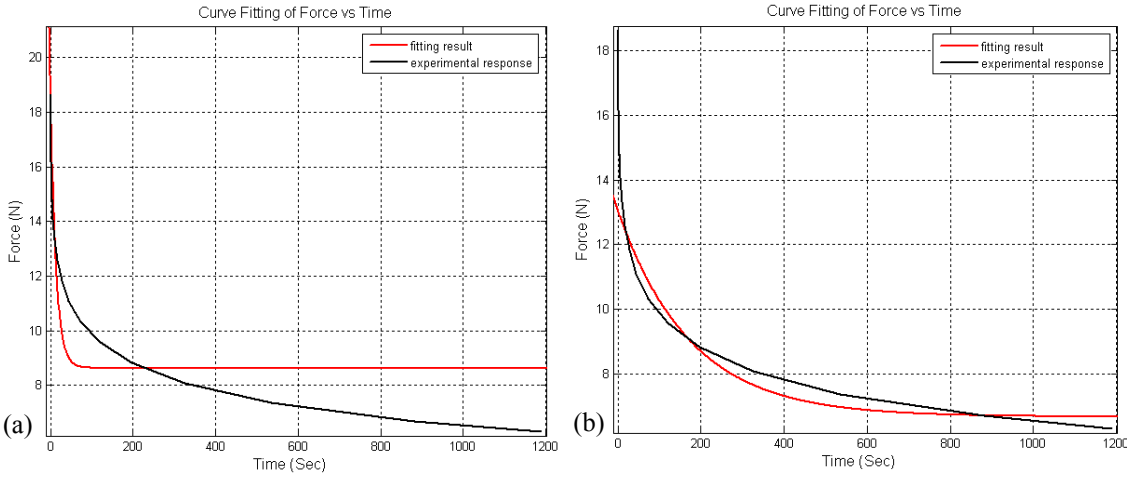

Figure 4.20: Curve fitting: (a) Pure Kelvin equation and (b) compensated Kelvin equation.

Nevertheless, it is observed that the equation does not match well with the experimental curve of the coagulated liver specimen. The pure Kelvin model equation fits well with the earlier relaxation response but forgoing the later response as

depicted in Figure 4.20(a). In contrast, the Kelvin equation resulted to match only the trend in the latter part of the relaxation response but neglecting the front portion of the response even after the best calibration of parameters and compensation of errors subjected to physical experimental inaccuracies, as per seen in Figure 4.20(b). The Kelvin model is then extended by incorporating a Maxwell model in front. Since the two models are in series, the equations are accumulated together, resulting in Equation (4.21):

$$F(t) = \left(\mu_2 u \cdot e^{-t\frac{\mu_2}{\eta_2}}\right) + \left(F(0)e^{-t\frac{\mu_1}{\eta_1}} + \mu_0 u\left(1 - e^{-t\frac{\mu_1}{\eta_1}}\right)\right). \qquad (4.21)$$

The pure Maxwell-Kelvin equation was again, fed into *cftool* to generate the equation curve based on the experimental force-time data. The result was similar to that of pure Kelvin equation discussed earlier. As revealed in Figure 4.21(a), the pure Maxwell-Kelvin equation also focuses only on the earlier response while neglecting the later. However, after careful and much calibration on an error correction factor, Figure 4.21(b) showed that the resulted curve finally seems to match closely to the experimental relaxation response with acceptable discrepancies within the standard deviation established from the experimental data, visualized by Figure 4.21(b).

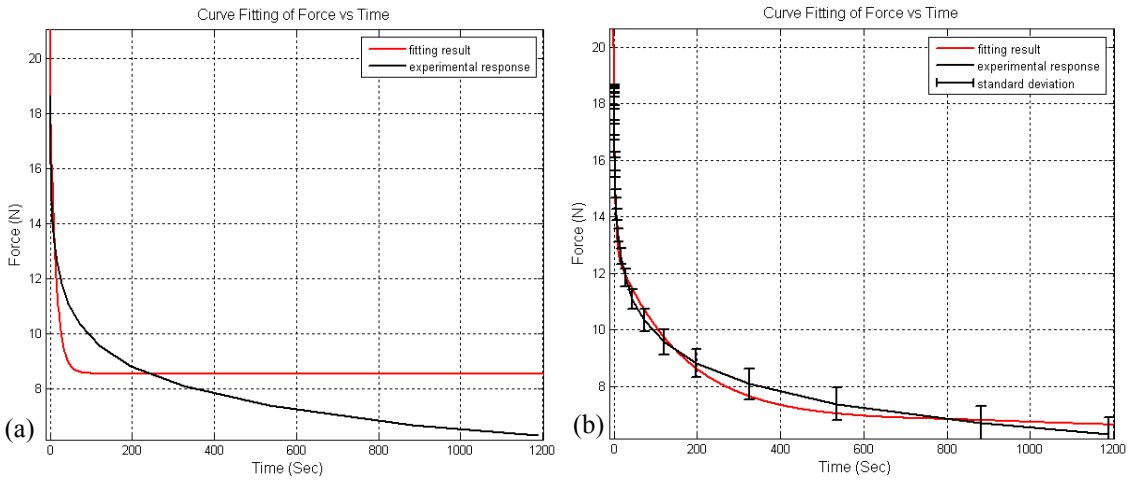

Figure 4.21: Curve fitting: (a) Maxwell-Kelvin equation and (b) compensated Maxwell-Kelvin equation.

As per mentioned, the Maxwell-Kelvin equation that accomplished the close fitting above was compensated with an error correction factor. This factor takes into account the inaccuracy of the physical experimental data and the imprecision of the experimental setup. Mechanical equipments; such as stepper motors and lead screws, are naturally subjected to noise and disturbance that causes vibrational and frictional losses. Hence, the experimental results are undoubtedly shifted by a certain error factor. Thus, to match experimental and theoretical together, the fundamental equation requires a compensation factor:

$$F(t) = (1.657)\left(\mu_2 u \cdot e^{-t\frac{\mu_2}{\eta_2}}\right) + \left(F(0)e^{-t\frac{\mu_1}{\eta_1}} + \mu_0 u\left(1 - e^{-t\frac{\mu_1}{\eta_1}}\right)\right). \quad (4.22)$$

In this analysis, the compensation factor of 0.6570 is multiplied to the fundamental Maxwell-Kelvin equation, resulting in Equation (4.22). The five mechanical parameters are then generated to be as in Table 4.3.

Table 4.3: Material parameters of the Maxwell-Kelvin model, derived from the relaxation function based on the compression test.

μ_0	μ_1	η_1	μ_2	η_2
1.369	2.409	365.7	1.228	2.845

Table 4.4: Relaxation parameters of standard linear model for the portion of Kelvin equation, derived from Equations (4.10) based on the values obtained in Table 4.3.

Relaxation Time for constant stress (sec), $\boldsymbol{\tau_\sigma}$	Relaxation Time for constant strain (sec), $\boldsymbol{\tau_\varepsilon}$	Relaxation Modulus, $\boldsymbol{E_R}$
115.3	151.8	1.369

Table 4.4 contains the computed relaxation parameters that fulfil the Kelvin equation, Equation (4.9). These parameters are used in the modelling of the coagulated liver tissue in the next sub-section.

4.3.5. Proposed Mechanical Model

From the previous analysis, it is found that the Maxwell-Kelvin equation closely approximates the response of the coagulated liver tissue. This enables to mechanical model to be directly derived as shown in Figure 4.22. The parameters attained from the curve fitting analysis are substituted accordingly to obtain the mechanical equations of the model.

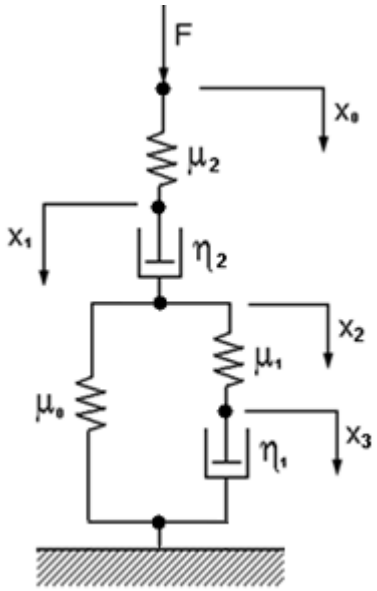

Figure 4.22: Proposed model of coagulated liver tissue implementing the Maxwell-Kelvin model.

The coagulated liver tissue is modelled with a combination of two mechanical constituents, a Maxwell component followed by a Kelvin model. As the coefficients are more than that of a non-coagulated model, there are more equations of motion to be solved. The lower three displacements, i.e. x_1, x_2 and x_3, are subjected to the virtual masses in between springs and dampers in series, and F is again the external force contribution to the compression of the liver tissue. The mechanical equations are derived as follows:

$$x_0 = x_1 + \frac{F}{\mu_2}, \tag{4.23}$$

$$\dot{x}_1 = \frac{\mu_2}{\eta_2} x_0 - \frac{\mu_2}{\eta_2} x_1 + \dot{x}_2 \,, \tag{4.24}$$

$$\dot{x}_2 = \dot{x}_1 + \frac{\mu_1}{\eta_2} x_3 + \frac{(-\mu_1 - \mu_0)}{\eta_2} x_2 \,, \tag{4.25}$$

$$\dot{x}_3 = \frac{\mu_1}{\eta_1} x_2 - \frac{\mu_1}{\eta_1} x_3 \,. \tag{4.26}$$

The attained parameters from the curve fitting analysis are substituted into the above equations to obtain simplified equations, as follows:

$$x_0 = x_1 + (0.8143)F \,, \tag{4.27}$$

$$\dot{x}_1 = (431.634)x_0 - (431.634)x_1 + \dot{x}_2 \,, \tag{4.28}$$

$$\dot{x}_2 = \dot{x}_1 + (846.749)x_3 - (1.3279)x_2 \,, \tag{4.29}$$

$$\dot{x}_3 = (0.00659)x_2 - (0.00659)x_3 \,. \tag{4.30}$$

Similar to that of the non-coagulated liver tissue, these equations are the major constituents of the tissue and probe interaction studies. These are essential for the cutting analysis onto the coagulated liver tissue in the subsequent chapter, in fulfilling the objective of the research and thesis.

4.4. Discussions and Conclusions

In this chapter, the mechanical properties of fresh, non-coagulated and the coagulated liver tissue are analysed. The differences between the two material properties are obviously seen from the analysis performed. The findings presented in this chapter are useful for the modelling the tissue and device interaction.

4.4.1. Stress/Strain Relationship Correlation

The stress/strain relationships of both the non-coagulated and coagulated liver tissue have been presented in the earlier sections. There are clear observations on the differences of both relationships. This entails the variations of both liver conditions in term of material properties as well.

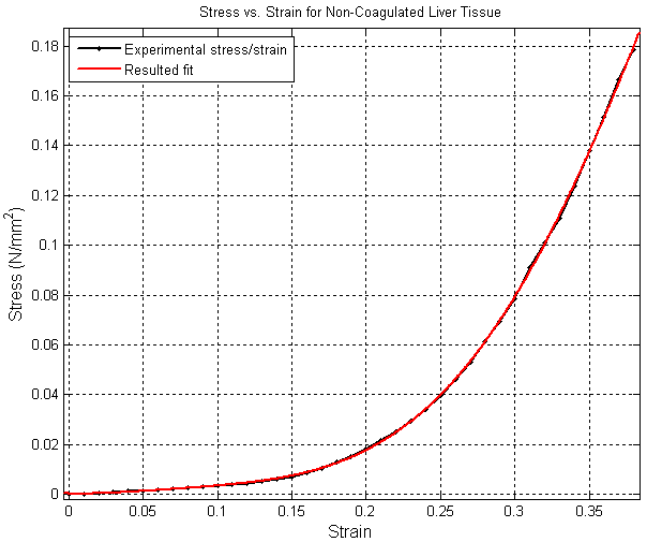

Figure 4.23: Curve fitting onto the stress/strain relationship of the non-coagulated liver tissue.

Figure 4.23 shows the stress/strain relationship of the non-coagulated liver tissue, which is extracted from Figure 4.18. Using the *cftool* function in Matlab, the stress/strain curve is matched with the red curve as pictured to attain the closest general equation. It is observed that the polynomial of order 5 fit the relationship well, resulting in Equation (4.31):

$$y_1 = -63.05x^5 + 56.91x^4 - 12.32x^3 + 1.211x^2 - 0.01701x + 0.00031\,. \quad (4.31)$$

The coagulated liver tissue though, has the stress/strain relationship shown in Figure 4.19. The relationship has almost similar trend as that of the non-coagulated tissue. It is also curve fitted in *cftool* to acquire a general equation corresponding to the stress/strain curve.

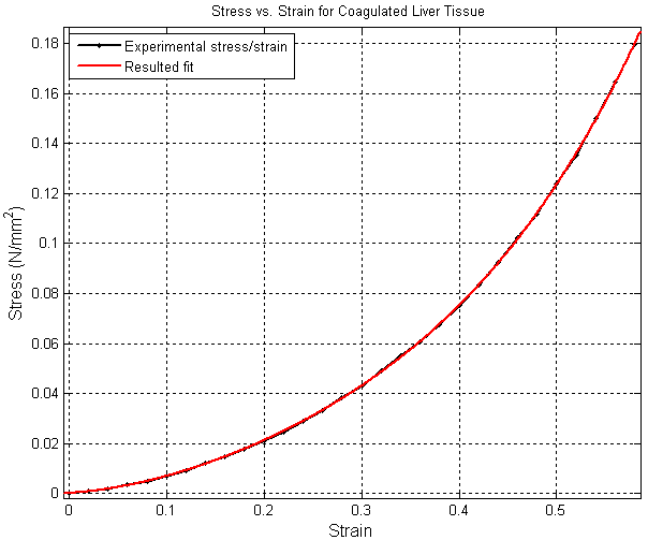

Figure 4.24: Curve fitting onto the stress/strain relationship of the coagulated liver tissue.

The curve was well fitted with a general 4th degree polynomial as depicted in Figure 4.24 above. The generated equation is given in Equation (4.32):

$$y_2 = 1.228x^4 - 0.744x^3 + 0.5136x^2 + 0.02285x + 0.000155\,. \quad (4.32)$$

This equation is applied with the equation generated by non-coagulated liver tissue to develop the correlation function between the two relationships. The relationships can be assumed to be correlated as by a function (α) equating to one another, as given by Equation (4.33). The function (α) is then simplified to be Equation (4.34):

$$y_2 = \alpha \cdot y_1\,, \quad (4.33)$$

$$\alpha = \frac{y_2}{y_1} = \frac{1.228x^4 - 0.744x^3 + 0.5136x^2 + 0.02285x + 0.000155}{-63.05x^5 + 56.91x^4 - 12.32x^3 + 1.211x^2 - 0.01701x + 0.00031}. \quad (4.34)$$

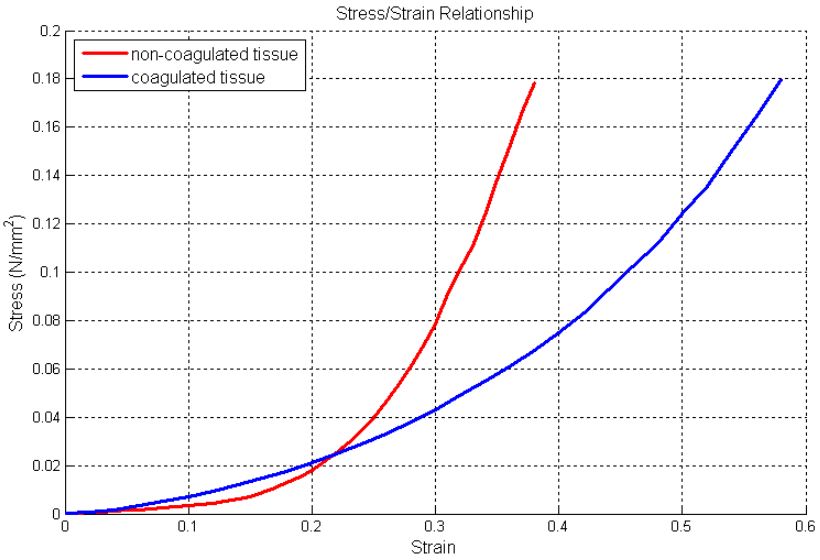

Figure 4.25: Stress/strain relationships of non-coagulated and coagulated liver tissue.

Figure 4.25 visualises the comparison between the coagulated and non-coagulated tissue stress/strain relationships. Both the tissues behave differently at different stress and strain. There exist however, an intersection between the two relationship, indicating a change of response. Prior to the "turning-point", the coagulated tissue reached higher stress with lower strain, in contrast with the non-coagulated tissue. After the "turning-point" though, the non-coagulated liver tissue requires higher stress to achieve the same strain as the coagulated tissue.

In addition, it is obvious that the coagulated tissue required more energy to rupture than the non-coagulated tissue. The steep gradient of the non-coagulated tissue stress/strain curve clearly implies that it has higher stiffness than the coagulated tissue; thus, it is able to cater for more mechanical load.

4.4.2. Mechanical Properties Comparison

As per discussed earlier, the non-coagulated liver tissue model closely relates to the Kelvin model, whereby the response of the relaxation decays exponentially. As seen in Figure 4.9, the curve generated by Kelvin equation approximates the

relaxation trend considerably throughout the response with appropriately computed parameters. It is also observed that the force response over time during the rapid front portion of the relaxation seems to be gradual, i.e. approximately an amount of 0.5N over 250 seconds, with an assumed relaxation rate of 0.002 N/sec.

For the coagulated liver tissue though, Figure 4.20 (a) and (b) clearly showed that Kelvin model alone was not sufficient in approximating the response of the relaxation response. It only traces either the front or the back portion of the relaxation while neglecting the other. When Maxwell model is merged with the Kelvin model, the combined equation resulted in a suitable fit after introducing an error compensation factor. Figure 4.20 visualised the fitting of the generated curve throughout the relaxation response. The front relaxation portion of more rapid exponential decay is portrayed by the simple Maxwell configuration while the latter portion relates to Kelvin constituent that consists of a more complex mechanical configuration with more parameters. Over the time duration of 250 seconds, the coagulated liver specimens experienced a decrease of about 10N upon compression up to the strain of 0.7. Thus, the relaxation rate at this point is assumed to be 0.004 N/sec, which is twice faster than the coagulated tissue.

It is noticed that the relaxation of fresh liver tissue was not as much and as rapid as the coagulated liver tissue. This may be due to the presence of fluid in the fresh non-coagulated tissue, i.e. blood, moist, and protein, which is of incompressible nature. The coagulated liver tissue has already experienced dehydration and protein degeneralisation. Thus, with the exsiccated and porosity nature, the coagulated liver tissue is less dense than the non-coagulated version and possesses the ability to absorb mechanical load exerted. Naturally, the coagulated liver tissue requires more force to rupture as compared to the non-coagulated tissue.

Chapter 5: Modelling of Liver Tissue/ Cutting Device Interaction

The interaction between tissue and device during an intervention is essential to for surgical planning. With the interaction model, feedback parameters from the surgical process can be determined and calibrated. This can aid to a more effective and reliable surgical process.

Prior to analysing the interaction between the liver tissue and device, the model of liver tissue has to be established. The liver tissue models in the previous chapter are essential for the liver tissue and cutting tool interaction modelling. As the study focuses on the analysis of ablated tissue upon cutting, this chapter solely discusses on the interaction between coagulated liver tissue and the cutting tool according to the prototype design. Thus, only the Maxwell-Kelvin model is incorporated for the study of the tissue/tool interaction modelling.

5.1. Hypotheses and Assumptions

Several assumptions have to be made in order to cater for the challenges encountered in this analysis. The assumptions assist in simplifying clinical conditions so that the interaction study can be performed. It is based on the established geometry of the blade and liver tissue that these assumptions are valid. If a different blade is implemented, a new construction of blade/tissue geometry may be required.

The scalpel blade, Aesculap BB511 is incorporated with the integrated RF ablation and cutting device prototype. The blade, prior to the breaking point on the liver surface is in perfect contact with the liver tissue. Thus, the liver geometry in contact with the blade edge is linear. Deformation of the liver tissue beyond the blade

contact tracks exponential curves to the surface of the liver tissue. Besides, the minimal thickness of the blade is assumed negligible for it does not significantly contribute to the experimental results as the tissue was punctured at the instant it is in contact with the blade point. Thus, the geometry of blade/tissue contact with the tissue can be illustrated as seen in Figure 5.1.

The liver tissue consists of an infinite number of the proposed mechanical models, i.e. Kelvin model and Maxwell-Kelvin model for the non-coagulated and coagulated liver tissue respectively. The property of the liver tissue is assumed to be homogenous and uniform. Hence, the same mechanical model can be implemented vertically throughout the liver. The mechanical constituent is arranged in a widespread beneath the liver surface as depicted in Figure 5.2.

It is hypothesized that the force exerted onto the scalpel blade is equals to the sum of the reaction forces generated by the liver, i.e. membrane tension and internal pressure forces, towards achieving equilibrium. The force onto the tissue by the scalpel blade is constant with respect to the deformation speed and distance. The internal pressure force is the force exerted by the portion of the liver which is in contact with the scalpel blade edges whereas the membrane force is due to the exponential trail produced by the deformation after the tissue-blade contact area.

5.2. Proposed Dynamic Model of Interaction

The geometry of the scalpel blade and liver tissue contact prior to reaching break point on the liver surface is simulated in MatLab as shown in Figure 5.1. Several parameters are predefined according to the assumptions made. In the simulation, the deformation set at 5mm is merely for visualisation of the deformation pattern. In the mathematical analysis, the deformation and external force exerted will be related to the experimental data from the penetration test onto the coagulated tissue.

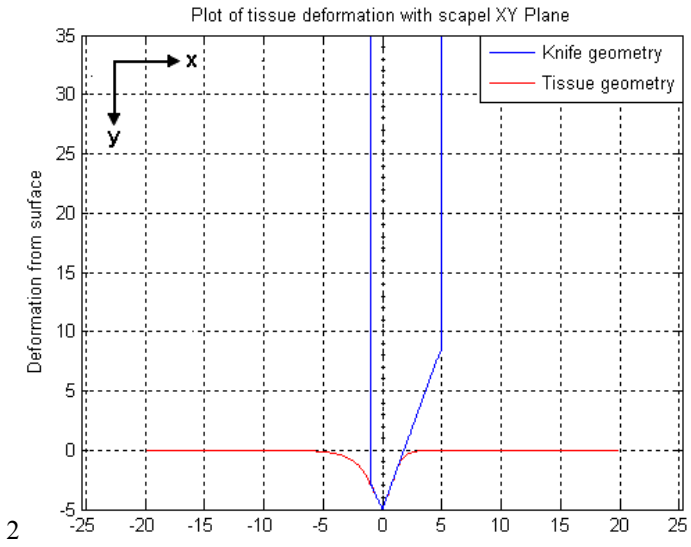

2

Figure 5.1: Graphical representation of the blade/tissue interaction prior to penetration.

The liver tissue and blade interaction is further described in Figure 5.2 with defined parameters. The deformation of the liver surface in contact with the blade edge is modelled with linear equations of gradient, while the deformation beyond the contact with the blade is characterised by exponential functions; the equations are as shown in Equations (5.2-5.5). The blade geometry is based on the actual measurement of the scalpel blade, whereby θ_1 and θ_2 are 70° and 65° respectively, and x_1 and x_2 are 1.2132 and -1 respectively.

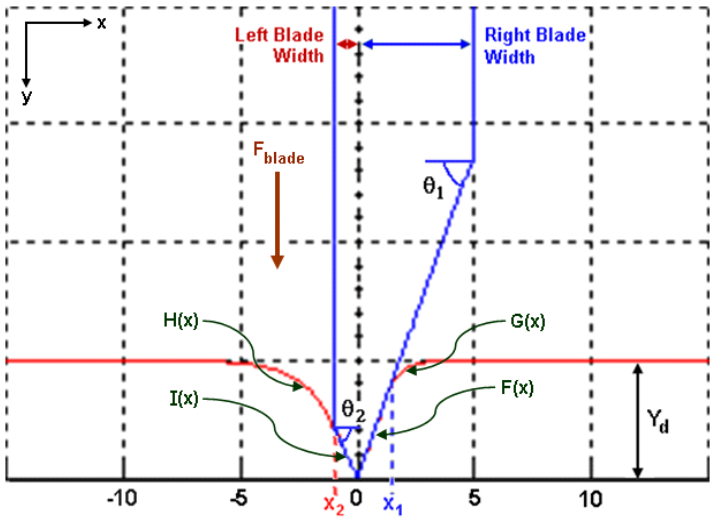

Figure 5.2: Parameter definitions on the tissue/blade interaction geometry.

The force exerted on the scalpel blade, F_{blade} is balanced by the reaction forces within the liver tissue, i.e. the internal pressure and membrane forces. The internal pressure forces are the reaction forces generated by the portion of tissue in contact with the blade edge, $F_{F(x)}$ and $F_{I(x)}$ by which *F(x)* and *I(x)* are the linear slope functions given by Equations (5.2) and (5.5). The membrane forces are that generated by the deformation which is not in contact with the blade, $F_{G(x)}$ and $F_{H(x)}$ whereby *G(x)* and *H(x)* are of exponential functions as in Equations (5.3) and (5.4). Hence, F_{blade} is equivalent to the sum of all internal pressure forces and the membrane forces. Y_d though, is the deformation distance required for the break force to be achieved.

$$F_{blade} = F_{reaction\ of\ tissue} = F_{F(x)} + F_{G(x)} + F_{H(x)} + F_{I(x)}\,, \tag{5.1}$$

$$F(x) = m_1 x + Y_d \quad whereby \quad slope = m_1 = -tan\theta_1\,, \tag{5.2}$$

$$G(x) = Ae^{B(x-x_1)} \quad whereby \quad A = Y_d - (x_1 tan\theta_1) \;\;\&\;\; B = {}^{m_1}/_{A}\,, \tag{5.3}$$

$$H(x) = Ce^{D(x-x_1)} \quad whereby \quad C = Y_d + (x_2 tan\theta_2) \;\;\&\;\; D = {}^{m_2}/_{C}\,, \tag{5.4}$$

$$I(x) = m_2 x + Y_d \quad whereby \quad slope = m_2 = tan\theta_2\,. \tag{5.5}$$

The uniform and homogenous distribution of the mechanical constituent of the coagulated liver tissue, the Maxwell-Kelvin model within the coagulated tissue is illustrated in Figure 5.3. The modelling analysis is executed with respect to the geometry and equations established here.

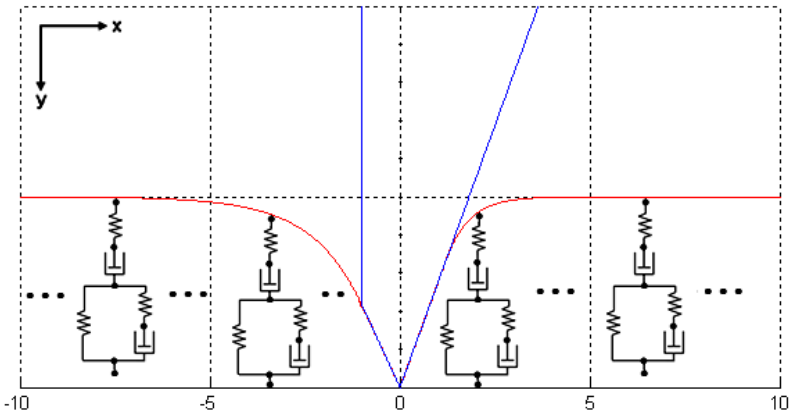

Figure 5.3: Distribution of Maxwell-Kelvin constituent beneath the liver tissue surface.

5.3. Experiment

Prior to the modelling analysis onto the dynamic model of the coagulated liver tissue and scalpel blade interaction, a penetration test is performed. The objective of the experiment is to observe the response of the coagulated liver tissue upon achieving the break force.

5.3.1. Penetration Tests

The experimental setup utilised in the compression test as described previously in Chapter 4 is modified for the indentation test. The force sensor is attached with a scalpel blade holder above a tissue holder resting on a work platform, as pictured in Figure 5.4(a). The blade and tissue holders are made of Delrin for light weight and corrosion prevention.

(a) 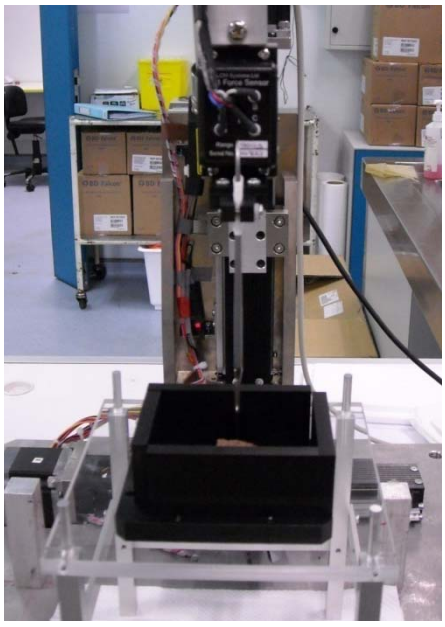 (b) 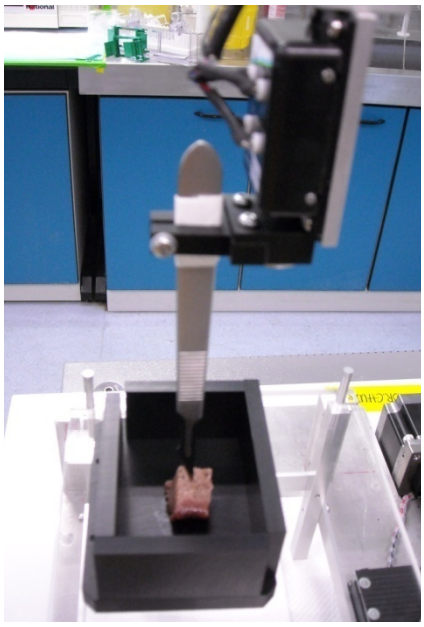

Figure 5.4: (a) Modified experimental setup for the penetration test, and (b) placement of the liver specimen in the tissue holder.

Similar to the compression test procedures, a fresh liver tissue is ablated using the RF ablation device at various lobes. Coagulated liver specimen cubes are

extracted by scalpel knife. The specimen is then placed in the tissue holder right below the scalpel blade attached to the force sensor, shown in Figure 4.5(b). The pointed edge of the blade is calibrated via the similar LabView GUI used in the compression test, to rest right above the surface of the specimen. The stepper motor speed is set at 1mm/sec and is executed to drive the blade 10mm into the specimen. The data of force versus time and distance travelled are acquired by the DAQ and processed for observations thereafter.

5.3.2. Experiment Results and Discussion

The typical experimental results attained from the penetration tests are then used to generate the 'force versus distance' and 'force versus time' graphs, depicted in Figure 5.5 and 5.6 respectively. The first obvious break force is assumed to be the break point onto the surface or membrane of the liver tissue. Beyond that, repetitive deformation and break forces are observed as the blade cuts further into the coagulated tissue. It may also be due to the vibration due to mechanical losses.

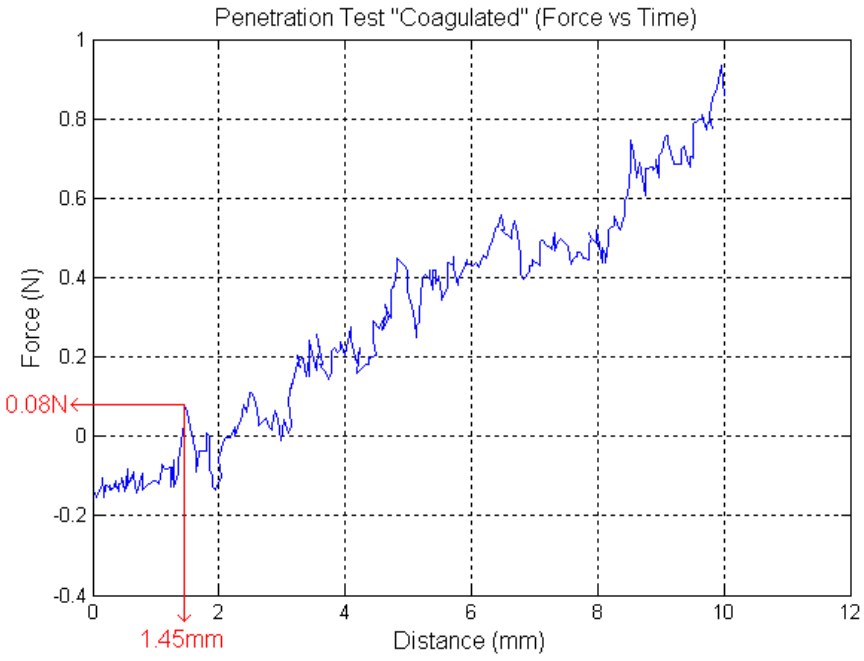

Figure 5.5: Coagulated tissue penetration test data plots, force versus distance.

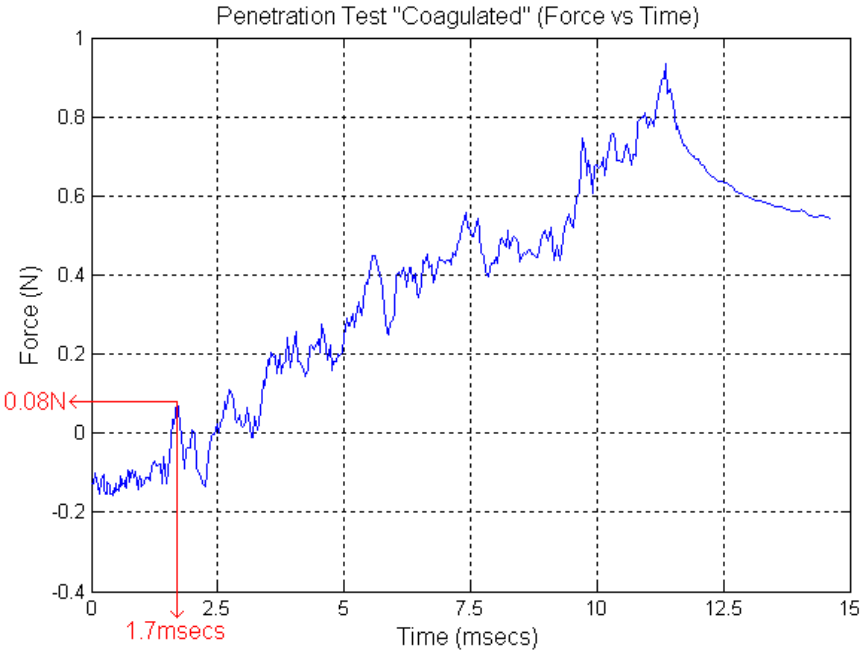

Figure 5.6: Coagulated tissue penetration test data plots, force versus time.

The approximately linear increase in force seen in the above responses is due to the friction between the blade and coagulated tissue as the blade traverse deeper into the tissue. The first break point is achieved by 0.08N of force exerted onto the scalpel blade (F) at a deformation distance of 1.45mm (Y_d) after 1.7 milliseconds (t) of execution. These parameters will be used to validate the interaction model proposed as per the geometry portrayed earlier.

5.4. Modelling Analysis

In this context, the analysis is performed onto the mechanical model of the coagulated tissue at the instance when break point is achieved. The break force, and the respective time and distance of deformation at that particular point are the important unknown variables. These variables differ with respect to several factors, such as deformation speed and experimental setup. This static analysis implements the parameters acquired from the experimental result for validation of the tissue/blade interaction model.

The required force-displacement equation is derived from the general Maxwell-Kelvin constituent equations, i.e. Equations (4.23) to (4.30), and is included into the mathematical structure of the blade/tissue interaction model. Equation (5.6) is formed by combining all the general equations into the function of reaction force (*F(s)*) in terms of instantaneous deformation displacement ($X_0(s)$), along with the substitution of respective material parameters. It is then followed by the simplification given in Equation (5.7), after being transformed into the time domain. The equations are shown as follows:

$$F(s) = \frac{\left[\frac{0.0066}{s+0.0066} - 1.568\right]}{\left[0.862 + \frac{0.1518}{s} + \frac{0.69}{s+0.8467} + \frac{0.0023}{s^2+0.0066s}\right]} \cdot X_0(s)\,, \tag{5.6}$$

$$F = \frac{0.0066e^{-0.0066t} - 1.568 \cdot \delta(t)}{0.862 \cdot \delta(t) + 0.1518 + 0.69e^{-0.8467t} + (0.3485)\left(1 - e^{-\frac{t}{151.52}}\right)} \cdot x_0 \cdot \tag{5.7}$$

Equation (5.7) resulted from the Inverse Laplace transform of Equation (5.6), thus there exist a time parameter, *t* and a delta function, *δ(t)*. Time, *t* in this analysis is taken as the instantaneous time when break point is achieved; hence the value is directly extracted from the penetration test result (*t* = 1.7 milliseconds). The delta function *δ(t)*, according to the Dirac delta function, is a unit impulse and is defined as,

$$\delta(t) = \begin{cases} 0; & t \neq 0 \\ 1; & t = 0 \end{cases} . \tag{5.8}$$

As *δ(t)* does not really have a physical meaning in the mathematical model, it is assumed to be a constant. It is then taken into advantage to be defined as a compensation or corrective factor to the mechanical losses and experimental inaccuracies involved in the process of constructing the Maxwell-Kelvin model. This constant parameter is tuned to accommodate to the experimental data in this analysis to create a suitable function to be validated.

Referring back to Figure 5.2 and 5.3, as the Maxwell-Kelvin constituents are distributed homogenously and infinitely beneath the tissue surface, the reaction forces exerted within the tissue are actually the sum of all forces under the corresponding functions, i.e. *F(x), G(x), H(x)* and *I(x)*. Thus, integration of the forces beneath the surface is required. The instantaneous deformation displacement, x_0 is equivalent to the functions, *F(x), G(x), H(x)* and *I(x)* for each respective force. The forces corresponding to each function are written as follows:

$$F_{F(x)} = \int_0^{x_1} \frac{[0.0066e^{-0.0066t} - 1.568 \cdot \delta(t)] \cdot F(x)}{0.862 \cdot \delta(t) + 0.1518 + 0.69e^{-0.8467t} + (0.3485)\left(1 - e^{-\frac{t}{151.52}}\right)}, \quad (5.9)$$

$$F_{G(x)} = \int_{x_1}^{\infty} \frac{[0.0066e^{-0.0066t} - 1.568 \cdot \delta(t)] \cdot G(x)}{0.862 \cdot \delta(t) + 0.1518 + 0.69e^{-0.8467t} + (0.3485)\left(1 - e^{-\frac{t}{151.52}}\right)}, \quad (5.10)$$

$$F_{H(x)} = \int_{x_2}^{0} \frac{[0.0066e^{-0.0066t} - 1.568 \cdot \delta(t)] \cdot H(x)}{0.862 \cdot \delta(t) + 0.1518 + 0.69e^{-0.8467t} + (0.3485)\left(1 - e^{-\frac{t}{151.52}}\right)}, \quad (5.11)$$

$$F_{I(x)} = \int_{-\infty}^{x_2} \frac{[0.0066e^{-0.0066t} - 1.568 \cdot \delta(t)] \cdot I(x)}{0.862 \cdot \delta(t) + 0.1518 + 0.69e^{-0.8467t} + (0.3485)\left(1 - e^{-\frac{t}{151.52}}\right)}. \quad (5.12)$$

Equations (5.9) to (5.12) are simplified to the Equations (5.13) to (5.16). The Equations (5.2) to (5.5) is substituted into the above equations along with the parameter, i.e. θ_1, θ_2, x_1, x_2, t, and Y_d. Equation (5.13) is then resulted upon solving for Equation (5.1), as shown below,

$$F_{blade} = F_{reaction\ of\ tissue} = \left(\frac{0.010698 - 2.541 \cdot \delta(t)}{1.397 \cdot \delta(t) - 1.368}\right). \quad (5.13)$$

The corrective factor, *δ(t)* resembles a tuning parameter to match the theoretical computation to the experimental result. For better implementation of the corrective factor, the Dirac Delta function is modified. The value of the compensation factor is only considered for the non-zero positive values of time, *t* as the process is invalid for negative values of *t*. Thus, *δ(t)* is defined as,

$$\delta(t) = \begin{cases} corrective\ factor; & t > 0 \\ 1; & t = 0 \\ 0; & t < 0 \end{cases} . \quad (5.14)$$

Upon careful calibration, it is found that the correction factor of 0.03 at time, *t* larger than zero enables the mathematical computation to closely approximate the experimental force value, 0.08N. The mathematical expressions of the modelling analysis are finalised to be as below,

$$F_{blade} = F_{reaction\ of\ tissue} = 0.08\,, \quad (5.15)$$

$$\delta(t) = \begin{cases} 0.03; & t > 0 \\ 1; & t = 0 \\ 0; & t < 0 \end{cases} . \quad (5.16)$$

5.5. Discussions

The modelling analysis performed validated the dynamic model proposed for the interaction between the coagulated liver tissue and scalpel blade. The penetration experiment data provides close estimation of the parameters and constants for the mathematical computation of force exerted onto the tissue by the blade.

The mathematical process involved the Inverse Laplace transform, generating a delta function, *δ(t)* which portrays impulse function input. However, in the practical experimental environment, the input is driven by a continuous signal that allows the force data to be continuously monitored. Hence, physically, it is not relevant to defined *δ(t)* as part of the input. Therefore, the existence of *δ(t)* due to the mathematical transformation is assumed as a corrective factor to compensate for the necessary losses that may incur onto the experimental data.

With the defined *δ(t)* and other assumptions, the mathematical expression derived from the dynamic interaction model is validated. The required force to create break point onto the tissue can be determined based on given experimental conditions.

Chapter 6: Conclusions

6.1. Discussion

Significant work and findings are acquired in the area of tissue modelling. A prototype of the integrated RF ablation and cutting device in aiding RF assisted resection surgery has been developed and discussed. The development of the prototype was the initial process of the research prior to the study on tissue modelling and analysis.

The focus of this thesis is on coagulated liver tissue as it is essential for the subsequent process of improvement onto the device prototype. The mechanical model of the coagulated liver is established based on the procedures and proposed model for fresh liver tissue. The dynamic modelling of the coagulated liver tissue/scalpel blade interaction is also demonstrated by implementing the proposed tissue model, which is based on the Maxwell-Kelvin model.

The validation of the interaction model is accomplished by matching the theoretical model to the experimental data. It is noted that the error correction factors in both the tissue model as well as the tissue/blade interaction model is necessary as compensation for the several possible physical factors, i.e. inaccuracy in motion and data acquisition, and mechanical losses from the experimental setup. With the calibration of these error corrective factors, the models are able to approximate closely to the actual tissue through investigation by experimental procedures.

The findings gained from this study will significantly contribute to the improvements of the prototype. Many future works, as per discussed in later sub-section, also seem promising towards the advancement in the bio-mechatronics field.

6.2. Contributions

One of the most significant values of a research and development project is the contribution towards the field of study. In this thesis, the innovation and analyses that contribute to important findings and development have been revealed and discussed.

The development of a new prototype integrating RF ablation and scalpel blade for tissue dissecting portrays advancement in the liver intervention field. With the incorporation of two conventionally separated processes in the hepatic resection procedure, haemorrhage issues are eliminated; thus, blood transfusion is not required. Moreover, time consumption and complexity of the surgery can be reduced; hence, beneficial to the patients in the safety and convenience wise.

The theoretical aspect of the prototype development is researched on toward progressing into a well defined-engineered stage. The mechanical model of a fresh non-coagulated tissue, a Kelvin model is introduced according to a previous work done. The interest in this research relates to the cutting response, the mechanical model of the coagulated liver tissue is established as to develop an interaction model for the tissue penetration response. A Maxwell-Kelvin model is defined to represent the coagulated tissue. It is essential for the construction of the interaction model.

Following the proposition of the coagulated liver tissue, the tissue/scalpel blade interaction model is constructed. Validation of the proposed interaction model is achieved upon implementation of the data acquired from physical penetration tests onto coagulated tissue. This interaction model and analyses procedures discussed in this thesis leads to the determination of parameters such as required penetration force with respect to minimal time and deformation. This procedure is useful for surgical simulation and planning as well as feedback design, i.e. haptic force feedback.

6.3. Recommendations and Future Works

There are many potential future works that can be taken into consideration with respect to the results accomplished in this study. Several recommendations of future enhancements are described as improvements to the work done in this research.

The mechanical and dynamic models proposed in this research are constructed via procedures involving curve fitting and mathematical analysis. More in-depth calibration of parameters in curve fitting using a better program or software may result in better construction of mechanical models. Thus, mathematical analyses onto the tissue/blade interaction model can also be improved along with the improvement on tissue mechanical model.

The validated models are mainly linear viscoelastic in nature as minimal deformation is strongly considered. However, to cater for larger deformation, non-linear viscoelasticity has to be considered. Thus, a more refined and complex mechanical model has to be investigated; for example, the quasi-linear viscoelastic model which caters for both minimal and large deformation onto soft tissues. The resulted version could then be used as a general model for both the linear and non-linear conditions.

The experimental setup utilised in this research work is developed with minimal cost materials and available commercial items. Even though the experimental results are reasonable, but errors and mechanical losses are still prone to occur. Thus, a better experimental setup can be constructed to acquire more precise and accurate data. A finer and smoother stepper motor can be considered along with a force transducer of finer precision. These will help enhance the experimental data for the curve fitting analyses as well as mechanical parameters and model determination.

Simulations works to visualise the response of the tissue and tissue/blade interaction models can also be considered. The parameters and models developed can be fed into simulation FE software, i.e. ANSYS or Abaqus to construct interactive, real time or static simulations. Simulations can also be executed in Matlab given the available parameters and computational structures. Input and output parameters can be varied to study the response onto the tissue and changes encountered according to the geometry construction of the tissue and the interaction. This will be an encouraging step towards surgical simulation and feedback analysis.

The prototype design of the integrated RF ablation and cutting device awaits enhancement. The design should be maintained small for laparoscopic surgery so that open surgery is not required. The design can be advanced by incorporating haptic force feedback sensing to monitor the forces required for cutting. It is desired to have appropriate force exerted as maximal force may affect surrounding tissue regions. Blood flow sensing is also a good consideration as to monitor the blood flow to a complete stop before dissecting into the liver tissue.

With an improved design of the prototype, in vivo experiments on pigs should be performed towards validating the implementation of the device prototype. This process will help determine which area of the design to be modified and further enhanced. It is also an important step towards introducing the device into the real surgical environment.

Last but not least, a robotic manipulator can be developed to be incorporated with the integrated RF ablation and cutting device. Repetitive ablation and cutting process can be executed more accurately by a robotic manipulator. This advancement will bring the new innovation towards realising an autonomous surgical world.

Bibliography

1. R.T. Poon, *Recent advances in techniques of liver resection.* Surg Technol Int, 2004. **13**: p. 71-7.
2. D. M. Parkin, B.F., J. Ferlay, P. Paola, *Global Cancer Statistics, 2002.* A Cancer Journal for Clinicians, March/April 2005. **55**(2).
3. *World Health Organization (WHO): The World Health Report*. 2002; Available from: http://www.who.int/whr/2002/en.
4. *China reports half of world's new liver cancer cases*. China Daily [Newspaper Report] July 28,2008; Available from: http://www.chinadaily.com.cn/china/2008-07/28/content_6882806.htm.
5. *National Cancer Centre Singapore Launches Inaugural Liver Cancer Awareness Month*. [Media Release] 19 August 2008; Available from: http://www.nccs.com.sg/news/2008/articles/080819.htm.
6. *World Health Organization: Cancer*. Fact Sheet N297 February 2009; Available from: http://www.who.int/mediacentre/factsheets/fs297/en/print.html.
7. *World Population Prospects: The 2006 Revision*, P.D. Department of Economic and Social Affairs, Editor. 2007, United Nations Publication: New York.
8. D. Haemmerich, *Hepatic radiofrequency ablation - An overview from an engineering perspective.* 26th Annual International Conference of the IEEE EMBS, September, 2004 p. 5433-5436.
9. Deshan Yang, M.C.C., David M. Mahvi, John G. Webster, *Measurement and Analysis of Tissue Temperature During Microwave Liver Ablation.* IEEE Transactions on Biomedical Engineering, January 2007. **54**(1): p. 150-155.
10. D. Radovanovic, et al., *Treatment of colorectal liver metastases with a combination of liver resection and radiofrequency ablation.* Med Pregl, 2005. **58**(1-2): p. 57-62.
11. C.K. Chui, et al., *Combined compression and elongation experiments and non-linear modelling of liver tissue for surgical simulation.* Medical & Biological Engineering & Computing, 2004. **42**: p. 787-798.
12. A. Ayav, L.R. Jiao, and N.A. Habib, *Bloodless liver resection using radiofrequency energy.* Dig Surg, 27 July 2007. **24**(4): p. 314-317.
13. G.D. Dodd, et al., *Minimally invasive treatment of malignant hepatic tumors: at the threshold of a major breakthrough.* Radiographies, 2000. **20**(1): p. 9-27.
14. S.G. Delis, et al., *Radiofrequency-assisted liver resection.* Surgical Oncology, 2007.
15. M.E.Ulucakli, *Simulation of Radiofrequency Ablation and Thermal Damage to Tissue.* Bioengineering Conference: Proceedings of the IEEE 32nd Annual Northeast, 2006: p. 93-94.
16. Y. Deshan , C.C.M., M.M. David, G. John, *Measurement and Analysis of Tissue Temperature during Microwave Liver Ablation.* IEEE Trans. on Biomedical Engineering, 2007. **54**: p. 150-155.
17. T. Ramachandran, *Water vaporization from heated tissue: An in vitro study by differential scanning calorimetry.* Lasers Surg. Med., 1996. **19**: p. 413-415.
18. S.F.F. Gibson, *Using Linked Volumes to Model Object Collisions,Deformation, Cutting, Carving, and Joining.* IEEE Transaction on Visualization and Computer Graphics, 1999. **5**(4): p. 333-348.
19. D. Terzopoulos, et al. *Elastically Deformable Models*. in *In Proceedings of SIGGRAPH*. 1987. Anaheim, USA.
20. Y.C. Fung, *Mechanical Properties of Living Tissues*. 2nd ed. Biomechanics: . 1993, New York: Springer-Verlag

21. J.H. Pringle, *Notes on the Arrest of Hepatic Hemorrhage due to Trauma. .* Ann Surg 1908(48): p. 541-549.
22. M.A. Hilal and J.P.A. Lodge, *Pushing back the frontiers of resectability in liver cancer surgery.* Journal of Cancer Surgery, 2008. **34**: p. 272-280.
23. W. Zhou, et al., *Selective hepatic vascular exclusion and Pringle maneuver: a comparative study in liver resection.* Eur J Surg Oncol, 2008. **34**(1): p. 49-54.
24. M. Cromheecke, et al., *Hepatic resection: haemostatic control by means of compression sutures: a new method.* Neth J Surg, 1991. **43**(4): p. 95-8.
25. S. Kondo, et al., *Arterioportal Shunting as an Alternative to Microvascular Reconstruction after Hepatic Artery Resection. .* Br J Surg 2004. **91**(2): p. 248-251.
26. D.O. Irabor, *Left Hepatectomy with Finger-Fracture Technique for Primary Liver Cell Carcinoma in a Tropical Low Socio-Economic Population.* Pakistan Journal of Medical Sciences, April-June 2008. **24**(3): p. 452-454.
27. B.N. Koo, et al., *Hepatic resection by the Cavitron Ultrasonic Surgical Aspirator increases the incidence and severity of venous air embolism.* Anesth Analg, 2005. **101**(4): p. 966-970.
28. Y. Hata, et al., *Liver Resection in Children, Using a Water-Jet.* Journal of Pediatric Surgery, May 2004. **29**(5): p. 648-650.
29. H. Bismuth, et al., *Liver Resection Versus Transplantation for Hepatocellular Carcinoma in Cirrhotic Patients.* Annals of Surgery, 1993. **218**(2): p. 145-151.
30. S.A. Curley, F. Izzo, and P. Delrio, *Radiofrequency ablation of unresectable primary and metastatic hepatic malignancies: results in 123 patients. .* Annals of Surgery, 1999. **230**(1): p. 1-8.
31. T.F. Wood, et al., *Radiofrequency Ablation of 231 Unresectable Hepatic Tumors: Indications, Limitations, and Complications. .* Annal of Surgical Oncology, 2000. **7**(8): p. 593-600.
32. L.M. Sutherland, et al., *Radiofrequency ablation of liver tumors: a systematic review.* Arch Surg, 2006. **141**(2): p. 181-90.
33. M.B. Nicholl and A.J. Bilchik, *Thermal ablation of hepatic malignancy: Useful but still not optimal.* European Journal of Surgical Oncology, 2007: p. 1-6.
34. R.A. Lencioni, et al., *Small Hepatocellular Carcinoma in Cirrhosis: Randomized comparison of Radio-frequency Thermal Ablation versus Percutaneous Ethanol Injection.* Radiology, 2003. **228**(1): p. 235-40.
35. N. Honda, et al., *Percutaneous hot saline injection therapy for hepatic tumors: an alternative to percutaneous ethanol injection therapy.* Radiology, 1994. **190**(1): p. 53-7.
36. G.M. Onik, et al., *Cryosurgery of liver cancer.* Seminars in Surgical Oncology, 1993. **9**(4): p. 309-317.
37. R.M. Charnley, J. Doran, and D.L. Morris, *Cryotherapy for liver metastases: A new approach.* British Journal of Surgery, 1989. **76**(10): p. 1040-1041.
38. X.D Zhou, et al., *Clinical evaluation of cryosurgery in the treatment of primary liver cancer Report of 60 Cases.* Cancer, 1988. **61**(9): p. 1889-1892.
39. T. Sarantou, A. Bilchik, and K.P. Ramming, *Complications of hepatic cryosurgery.* Seminars in Surgical Oncology, 1998. **14**(2): p. 156-162.
40. V. Arienti, et al., *Complications of laser ablation for hepatocellular carcinoma: a multicenter study.* Radiology, 2008. **246**(3): p. 947-55.
41. C.J. Simon, D.E. Dupuy, and W.W. Mayo-Smith, *Microwave ablation: principles and applications.* Radiographics, 2005. **25 Suppl 1**: p. S69-83.

42. N. Bhardwaj, et al., *A comparative histological evaluation of the ablations produced by microwave, cryotherapy and radiofrequency in the liver.* Pathology, 2009. **41**(2): p. 168-72.
43. G.D. Dodd, *Percutaneous RF Ablation of Colorectal Hepatic Metastases*. 2003, American Cancer Society.
44. Y. Peng, *Studies of the Bipolar InLine Radiofrequency Ablation Device in Liver and Kidney Transection*, in *Department of Surgery*. 2007, University of New South Wales: Kogarah, Australia. p. 244.
45. A. Ayav, et al., *Liver Resection With a New Multiprobe Bipolar Radiofrequency Device.* Arch Surg, 2008. **143**(4): p. 396-401.
46. M.E. Ulucakli, *Simulation of Radiofrequency Ablation and Thermal Damage to Tissue.* Bioengineering Conference: Proceedings of the IEEE 32nd Annual Northeast, 2006: p. 93-94.
47. P. Bachellier, et al., *Laparoscopic Liver Resection Assisted with Radiofrequency.* The American Journal of Surgery, 2007. **193**: p. 427-430.
48. L.R. Jiao, et al., *Radiofrequency assisted liver resection--a novel technique.* Hepatogastroenterology, 2005. **52**(66): p. 1685-1687.
49. L. Jiao, et al., *Radio Frequency Assisted Liver Resection: The Habib's Technique*, in *Liver and Pancreatic Diseases Management*. 2006, Springer US. p. 31-37.
50. D. Hompes, et al., *Laparoscopic liver resection using radiofrequency coagulation.* The Journal of Surgical Endoscopy, 2007. **21**: p. 175-180.
51. T.E. Clancy and R.S.Swanson, *Laparoscopic Radiofrequency-Assisted Liver Resection (LRR): A Report of Two Cases.* Digestive Diseases and Sciences, December 2005. **50**(12): p. 2259-2262.
52. A. Navarro, et al., *Laparoscopic Blood-Saving Liver Resection using a New Radiofrequency-Assisted Device: Preliminary Report of an In Vivo Study with Pig Liver.* The Journal of Surgical Endoscopy, 2008. **22**: p. 1384-1391.
53. M. Mitsuo, et al., *Radiofrequency (RF)-Assisted Hepatectomy May Induce Severe Postoperative Liver Damage.* World Journal of Surgery, 2007. **31**: p. 2208-2212.
54. E. Berber and A. Siperstein, *Radiofrequency (RF)-assisted Hepatectomy may Induce Severe Liver Damage.* World Journal of Surgery, 2008. **32**: p. 1897-1898.
55. M. Milicevic and P. Bulajic, *Radiofrequency-Assisted Liver Resection Does Not Induce severe Liver Damage.* World Journal of Surgery, 2008. **32**: p. 1901-1902.
56. E. Basafa, F. Farahmand, and G. Vossoughi, *A Non-Linear Mass-Spring Model for More Realistic and Efficient Simulation of Soft Tissues Surgery*, in *Studies in Health Technology and Informatics*, J.D. Westwood, et al., Editors. 2008, IOS Press. p. 23-25.
57. M. Nesme, F. Faurel, and Y. Payan, *Hierarchical Multi-Resolution Finite Element Model for Soft Body Simulation.* Lecture Notes in Computer Science, 2006 **4072** p. 40-47.
58. S. Cotin, H. Delingette, and N. Ayache, *Efficient linear elastic models of soft tissues for real-time surgery simulation.* Stud Health Technol Inform, 1999. **62**: p. 100-101.
59. H. Lamecker, T. Lange, and M. Seebass, *A Statistical Shape Model for the Liver.* Lecture Notes In Computer Science**,** MICCAI, 2002. **2489**: p. 421-427.
60. H. Lamecker, T. Lange, and M. Seebass, *Segmentation of the Liver Using a 3d Statistical Shape Model.* Konrad-Zuse-Zentrum fur Informationstechnik Berlin, 2004: p. 4-8.
61. L. Massoptier and S. Casciaro. *Fully Automatic Liver Segmentation through Graph-Cut Technique*. in *Proceedings of the 29th Annual International Conference of the IEEE EMBS Cité Internationale,* . August 23-26, 2007. Lyon, France.

62. S. Casciaro, et al. *A Method for Fast and Automatic Segmentation of Soft Organs from CT and MR Images* in *Proceedings of 20th Int. Congress Computer Assisted Radiology and Surgery*. June 2006. Osaka, Japan
63. H. Delingette and N. Ayache, *Soft Tissue Modeling for Surgery Simulation*, in *Handbook of Numerical Analysis*, P.G. Ciarlet, Editor. 2004, Elsevier B.V.: Sophia-Antipolis, France.
64. J. Montagnat and H. Delingette, *Globally Constrained Deformable Models for 3d Object Reconstruction.* Signal Processing, 1998. **71**(2): p. 173-186.
65. W. Lorensen and H.E. Cline, *Marching Cubes: A High Resolution 3D Surface Construction Algorithm.* ACM Computer Graphics (SIGGRAPH'87) 1987. **21**: p. 163-169.
66. F. Buchtel and E. Kaiser. *The Rheology of the Cross Striated Muscle Fibre with Particular Reference to Isotonic Conditions*. in *Biol. Medd*. 1951. Det Kongelige Danske Videnskabernes Selskab, Copenhagen, Dan.
67. A. Viidik, *Biomechanics and functional adaptation of tendons and joint ligaments.* , in *Studies on the anatomy and function of bone and joints.* , F.G. Evans, Editor. 1966, Springer: New York. p. 17-38.
68. D. Terzopoulos and K. Fleiseher, *Modeling Inelastic Deformation:Viscoelasticity, Plasticity, Fracture*, in *SIGGRAPH '88*. August 1988, ACM: Atlanta.
69. J.M. Schwartz, et al., *Modeling liver tissue properties using a non-linear visco-elastic model for surgery simulation.* Medical Image Analysis 2005. **9**: p. 103-112.
70. S.C. Ko, S. Lee, and C.H. Hsueh, *Viscoelastic Stress Relaxation in Film/Substrate Systems-Kelvin Model.* Jour on Applied Physics 2003. **9**(5): p. 2453-2457.
71. J. Flanagan and L. Landgraf, *Self-Oscillating Source for Vocal-tract Synthesizers.* IEEE Trans. On Audio and Eletroacoustics, 1968. **16**: p. 57-64
72. K. Ishizaka and J. Flanagan, *Synthesis of Voiced Sounds from Two-Masses Model of the Vocal Cords.* Bell Syst. Tech. Journal, 1972. **51**: p. 1233-1268.
73. M. Hauth, et al., *Soft Tissue Simulation Based on Measured Data,* , in *Medical Image Computing and Computer-Assisted Intervention*. 2003, Springer Berlin / Heidelberg. p. 262-270.
74. R. Sinkus, *MR-Elastography* Ecole Supérieure de Physique et de Chimie Industrielles de la Ville de Paris.
75. L. Huwart, et al., *Liver fibrosis: Non-Invasive Assessment with MR Elastography.* NMR Biomed., 2006. **19**: p. 173-179.
76. S.P. Dimaio and S.E. Salcudean, *Simulated Interactive Needle Insertion*, in *International Symposium on Haptic Interfaces for Virtual Environment and Teleoperator System*. 2002: USA. p. 344-351.
77. K .V. Hansen, et al., *Modelling of interaction between a spatula and a human brain.* Medical Image Analysis, 2004 **8**: p. 23-33.
78. T. Chanthasopeephan, J.P. Desai, and A.C. Lau, *Measuring forces in liver cutting: new equipment and experimental results.* Ann Biomed Eng, 2003. **31**(11): p. 1372-1382.
79. T. Chanthasopeephan, J.P. Desai, and A.C. Lau, *Study of soft tissue cutting forces and cutting speeds.* Stud Health Technol Inform, 2004. **98**: p. 56-62.
80. T. Chanthasopeephan, J.P. Desai, and A.C. Lau, *Modeling soft-tissue deformation prior to cutting for surgical simulation: finite element analysis and study of cutting parameters.* IEEE Trans Biomed Eng, 2007. **54**(3): p. 349-359.
81. T. Azar and V. Hayward. *Estimation of the Fracture Toughness of Soft Tissue From Needle Insertion*. in *In Proc. of Biomedical Simulation, 4th International Symposium*. 2008: Springer Verlag.

82. B. Maurin, et al. *In Vivo Study of Forces during Needle Insertions*. in *Perspective in Image-guided Surgery: Proceedings of the Scientific Workshop on Medical Robotics, Navigation, and Visualization (MRNV'04)*. 2004.
83. M.E. Rentschler, et al., *Modeling, Analysis, and Experimental Study of In Vivo Wheeled Robotic Mobility.* IEEE Transactions on Robotics, April 2006. **22**(2).
84. H. Delingette. *Towards Realistic Soft Tissue Modeling in Medical Simulation*. in *IEEE Proceedings: Special Issue on Surgery Simulation*. April 1998.
85. F. Buchtal and E. Kaiser. *The Rheology of the Cross Striated Muscle Fibre with Particular Reference to Isotonic Conditions*. in *Biol. Medd*. 1951. Det Kongelige Danske Videnskabernes Selskab, Copenhagen, Dan.
86. C.K. Chui, *Mechanical Properties, Constitutive Equations, Integrative Computational Model of Liver and their Applications in Compuater Aided Surgery*. 2004, PhD, The University of Tokyo,: Japan.

List of Publications

1. C.Y.F. Leong, L.J. Yang, K.Y.S. Chang, A.N. Poo, I. Sakuma, C.K. Chui, *A Precise Robotic Ablation and Division Mechanism for Liver Resection*, in *Proceedings of 4th International Workshop on Medical Imaging and Augmented Reality*, Tokyo, Japan, August, 2008.

2. C.Y.F. Leong, C.K. Chui, K.Y.S. Chang, I. Sakuma, A.N. Poo, *Modeling and Simulation of Tissue/Device Interaction using Standard Viscoelastic Model*, in *Proceedings of IEEE International Conference on Systems, Man, and Cybernetics*, Singapore, October, 2008.

3. B. P. Nguyen, T. Yang, C.Y.F. Leong, K.Y.S. Chang, S.H. Ong, C. K. Chui, *Patient Specific Biomechanical Modeling of Hepatic Vasculature for Augmented Reality Surgery*, in *Proceedings of 4th International Workshop on Medical Imaging and Augmented Reality*, Tokyo, Japan, August, 2008.

Appendices

EXPERIMENT PROCEDURES & SETUPS:

Compression Test:

1) Coagulated liver specimens from different portions of the fresh and perfused porcine liver are extracted.
2) The specimens are cut into dimensions of 10mm diameter, 10 mm height and mass of 0.7g with a cylindrical aluminium cutter.
3) The cylindrical specimens are then glued onto thin rubber pieces, which are already attached to tissue holder by super glue, with Aesculap Hystoacryl® surgical bond.
4) The bottom tissue holder with liver specimen is held in place by a clamper while the top holder piece is screwed onto the LCM Systems 15N force transducer with the aid of calibration in the LabView GUI.
5) The LabView GUI is then configured to specific operation process for the compression test, i.e. speed of 1mm/sec at strain of 0.7.
6) Upon compression, the stepper motor stopped when the strain of 0.7 is reached and the specimens are held in place for 20 minutes to acquire relaxation data.
7) The experimental data is then utilised to analyse the force versus time relaxation response as well as the stress versus strain relationship.

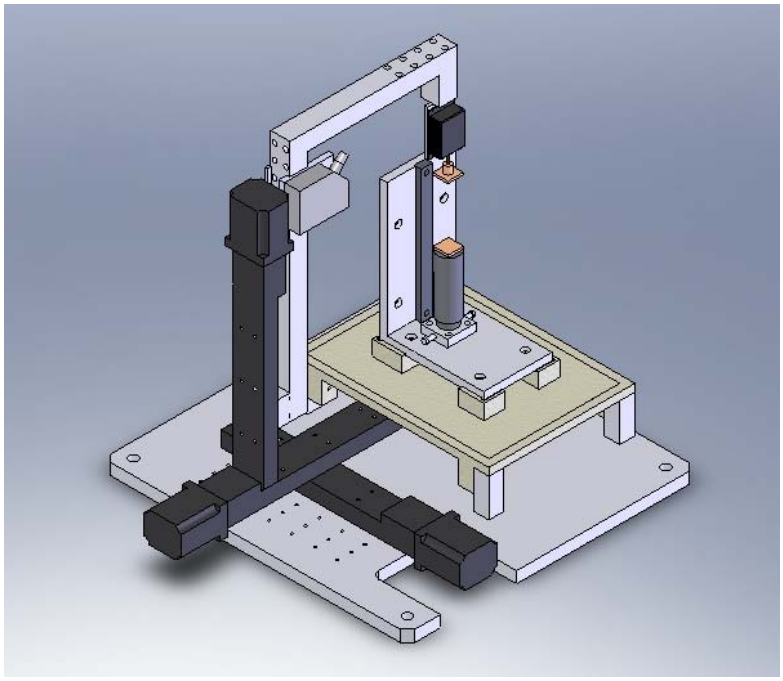

Figure: Experiment setup for the Compressions Test

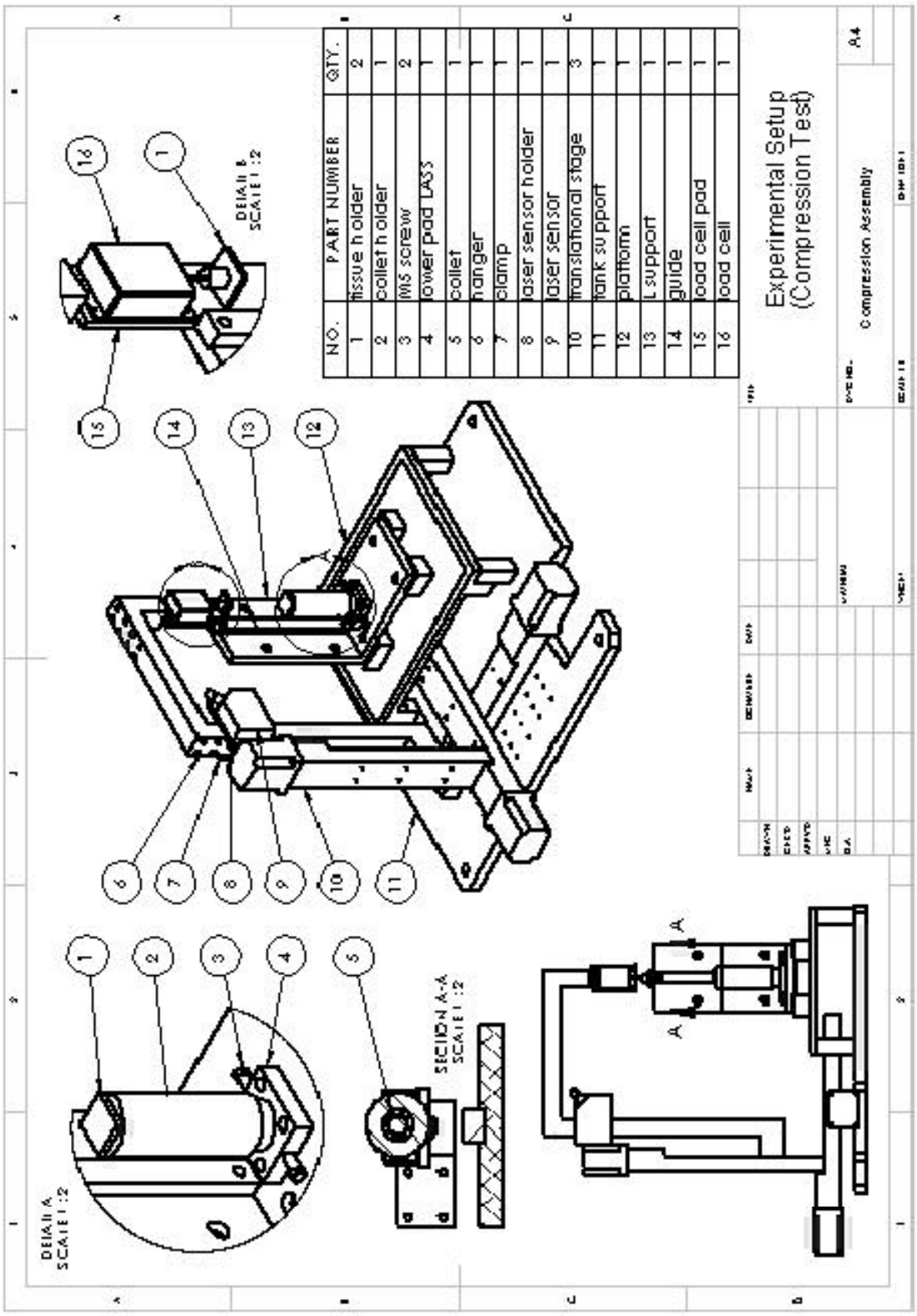

Figure: Assembly drawing of the compression test experiment setup

Indentation Test:

1) Porcine liver specimens (non-coagulated and coagulated) with dimensions of 60x80x20mm are prepared.
2) Middle portions of the specimens are ablated with Habib 4X Laparoscopic RFA device.
3) Specimens are then placed in a tissue holder placed within the experimental set up.
4) The indentor with a rounded tip measuring 2mm in diameter is attached to the LCM Systems 15N force sensor.
5) With the calibration in the LabView GUI, the stepper motor connecting to the force sensor is set to contact the indentor with the liver specimen surface.
6) The indentation process is then executed based on a range of calibrated motor speeds and deformation distance.
7) The data are then acquired and processed with MatLab to enable observations onto the force versus distance and force versus time responses.

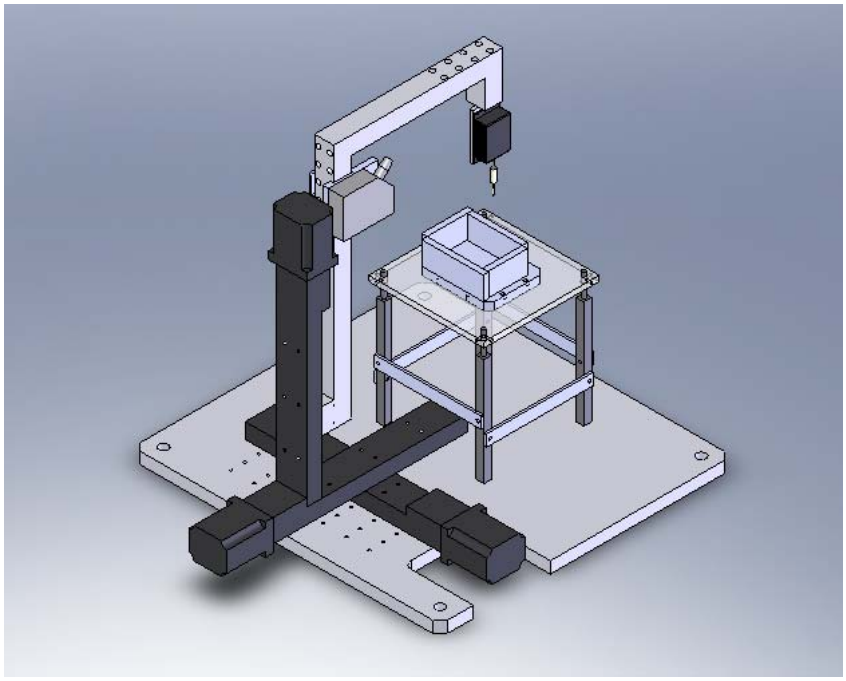

Figure: Experiment setup for the Indentation Test

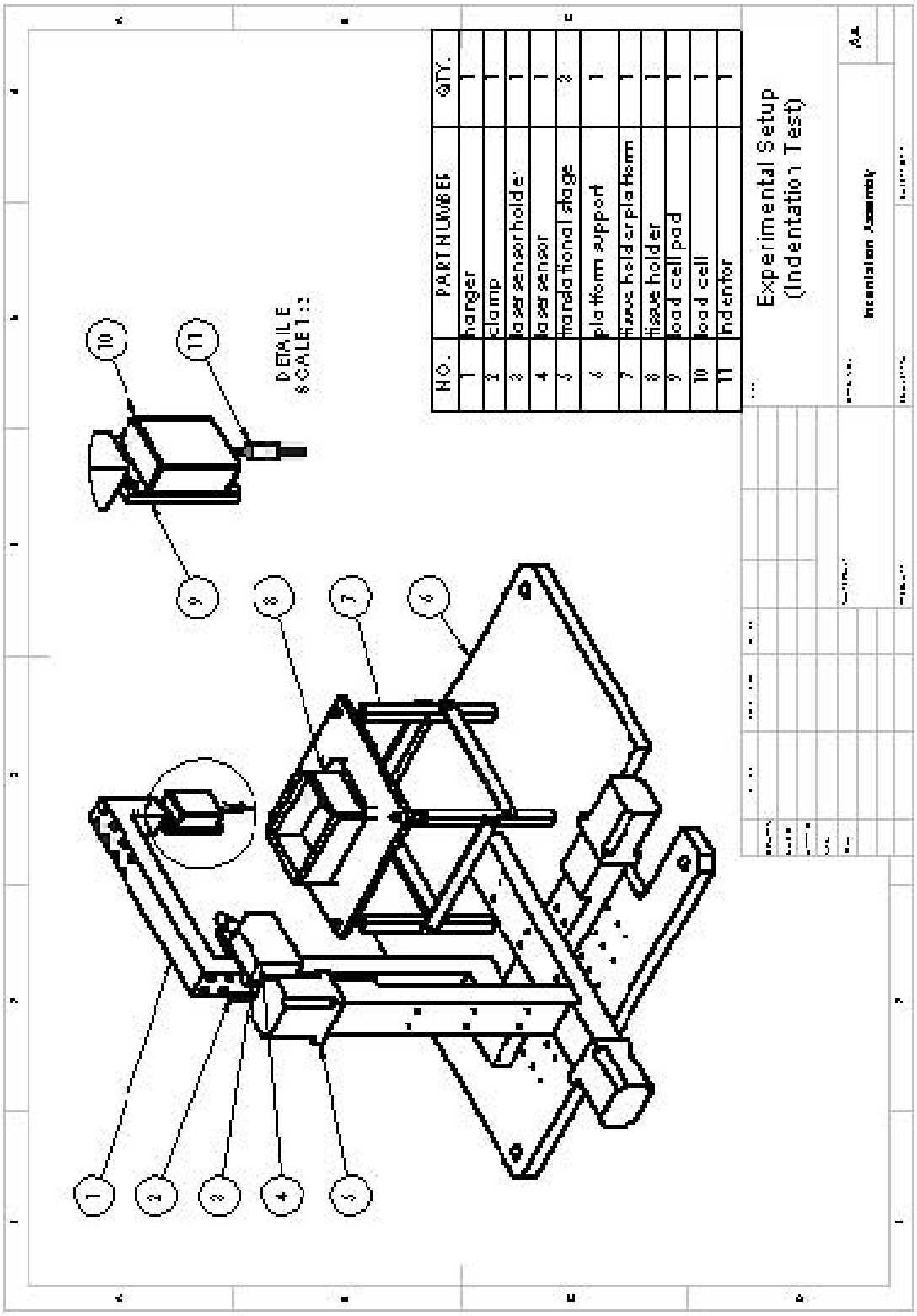

Figure: Assembly drawing of the indentation test experiment setup

Penetration Test:

1) Porcine liver specimens (non-coagulated and coagulated) with dimensions of 60x80x20mm are prepared.
2) Middle portions of the specimens are ablated with Habib 4X Laparoscopic RFA device.
3) Specimens are then placed in a tissue holder placed within the experimental set up.
4) A surgical knife with scalpel blade model (BB540 or BB511) is attached to the LCM Systems 15N force sensor.
5) With the calibration in the LabView GUI, the stepper motor connecting to the force sensor is set to contact the indentor with the liver specimen surface.
6) The indentation process is then executed based on a range of calibrated motor speeds and deformation distance.
7) The data are then acquired and processed with MatLab to enable observations onto the force versus distance and force versus time responses.

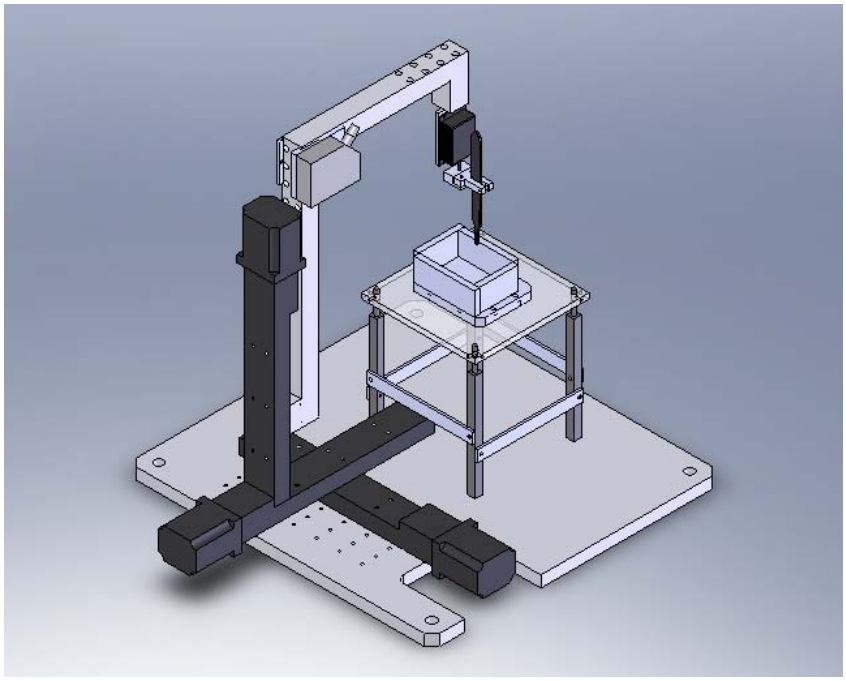

Figure: Experiment setup for the Penetration Test

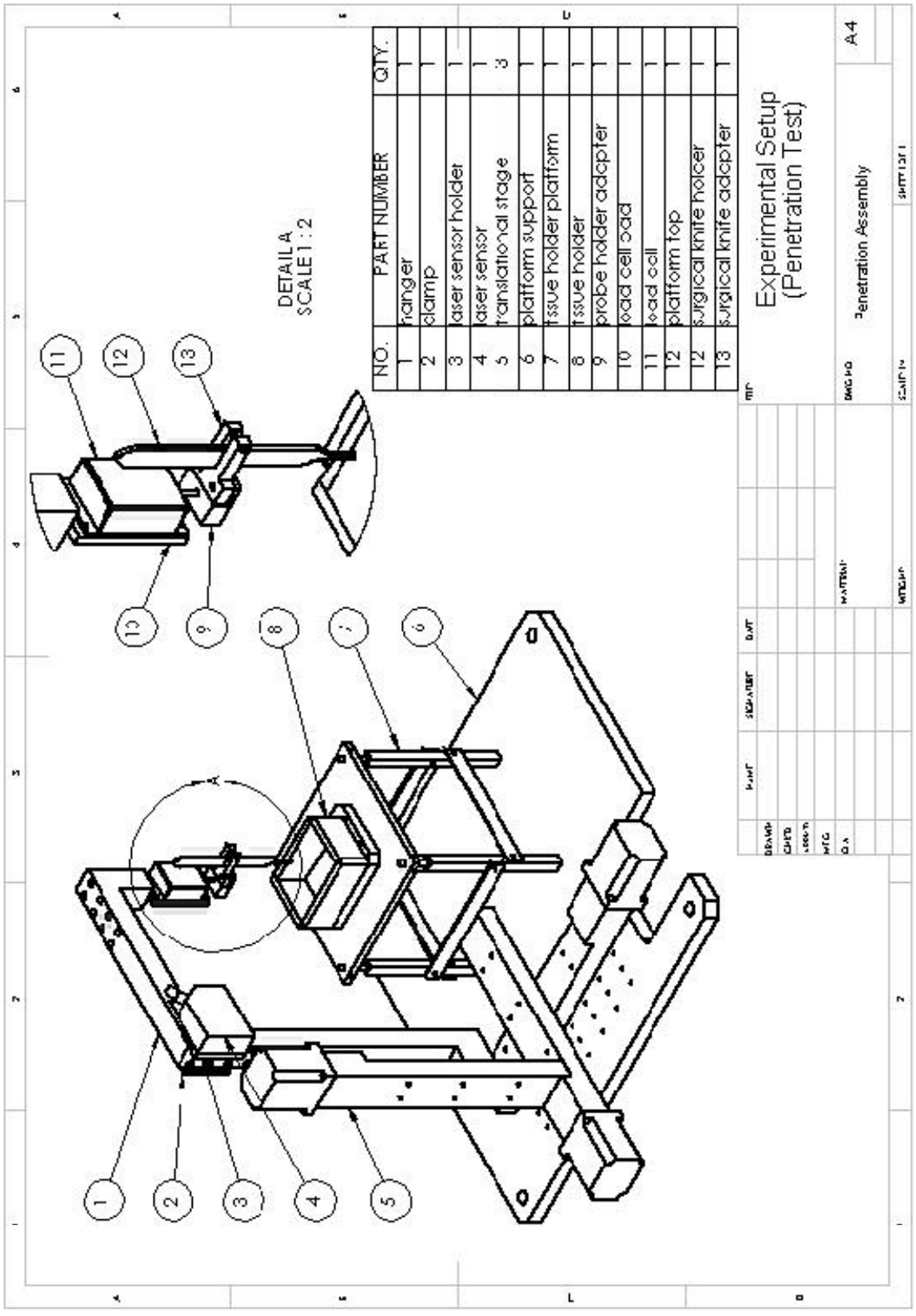

Figure: Assembly drawing of the penetration test experiment setup